Thesis for the degree of Doctor of Philosophy

There's Plenty of Room in Higher Dimensions

Nonlinear Dynamics of Nanoelectromechanical Systems

Axel Martin Eriksson

CHALMERS

Department of Physics

Chalmers University of Technology

Göteborg, Sweden 2017

There's Plenty of Room in Higher Dimensions

Nonlinear Dynamics of Nanoelectromechanical Systems

Axel Martin Eriksson

ISBN 978-91-7597-613-6

Doktorsavhandlingar vid Chalmers tekniska högskola

Ny serie nr 4294

ISSN 0346-718X

Department of Physics

Chalmers University of Technology

SE-412 96 Göteborg

Sweden

Telephone + 46 (0)31-772 1000

Typeset in LaTeX.

Figures created using MATLAB, MATHEMATICA and POWERPOINT.

Printed by Chalmers Reproservice

Göteborg, Sweden 2017

There's Plenty of Room in Higher Dimensions
Nonlinear Dynamics of Nanoelectromechanical Systems
Axel Martin Eriksson
Department of Physics
Chalmers University of Technology

Abstract

Nanoelectromechanical systems (NEMS) couple the dynamics of electrons to vibrating nanostructures such as suspended beams or membranes. These resonators can be used in for instance nanoelectronics and sensor applications. NEMS are also of fundamental interest since electrons exhibit strong quantum effects when confined in nanoobjects. Furthermore, NEMS such as graphene resonators are strongly nonlinear, which opens the door for complex dynamical response.

The operation of nanoresonators often rely on actuation of mechanical vibrations driven by an electric ac-field. The first part of this thesis theoretically investigates high-frequency nonresonant actuation relying on electromechanical back action (Papers I-II). The nonresonant phenomenon can be utilized to study nonlinear dissipation and to selectively actuate different vibrational modes, also asymmetric ones, even though the driving field is homogeneous (Paper III). Another nonresonant actuation mechanism converts heat into mechanical energy and relies on electron-electron interaction in a movable quantum dot (Paper IV).

Furthermore, parametric actuation of a nanoresonator can be used to generate a supercurrent through a superconducting weak link even though the superconducting phase difference across the link is zero (Paper V). The excitation leads to a spontaneous symmetry breaking, which allows for a new possibility to switch between the two current directions.

Actuation of mechanical vibrations is also used to study nonlinear dynamics and mode coupling in nanoresonators. The strength of nonlinearities and vibrational frequencies can be tuned by electrostatic means (Paper VI). This tunability and the low dissipation in nanoresonators make it possible to selectively address individual or combinations of modes. Coupled modes allow for much richer nonlinear dynamics, such as internal resonances (Paper VII), due to the increased dimensionality of the relevant phase space. Furthermore, exotic dynamical regions may be hidden and not observed in standard experiments. However, bifurcation theory can help to construct maps which reveal the hidden regions. A lot more is therefore to be expected from coupled mode dynamics, since *there's plenty of room in higher dimensions.*

KEYWORDS: NEMS, nonlinear dynamics, nonresonant actuation, quantum dots, superconductivity, internal resonance.

List of appended papers

This thesis consists of an introductory text and the scientific papers:

I. *Nonresonant high frequency excitation of mechanical vibrations in a graphene based nanoresonator*
A. M. Eriksson, M. V. Voinova and L. Y. Gorelik
New Journal of Physics **17**, 033016 (2015)

II. *Nonresonant high-frequency excitation of mechanical vibrations in a movable quantum dot*
A. M. Eriksson
New Journal of Physics **17**, 113057 (2015)

III. *Selective nonresonant excitation of vibrational modes in suspended graphene via vibron–plasmon interaction*
A. M. Eriksson and L. Y. Gorelik
2D Materials **2**, 045008 (2015)

IV. *Nanoelectromechanical Heat Engine Based on Electron-Electron Interaction*
A. Vikström, **A. M. Eriksson**, S. I. Kulinich, and L. Y. Gorelik
Physical Review Letters **117**, 247701 (2016)

V. *Zero-Phase-Difference Josephson Current Based on Spontaneous Symmetry Breaking via Parametric Excitation of a Movable Superconducting Dot*
A. M. Eriksson and A. Vikström,
Physical Review Letters **118**, 197701 (2017)

VI. *Frequency tuning, nonlinearities and mode coupling in circular mechanical graphene resonators*
A. M. Eriksson, D. Midtvedt, A. Croy and A. Isacsson
Nanotechnology **24**, 395702 (2013)

VII. *Energy-dependent path of dissipation in nanomechanical resonators*
J. Güttinger, A. Noury, P. Weber, **A. M. Eriksson**, C. Lagoin, J. Moser, C. Eichler, A. Wallraff, A. Isacsson and A. Bachtold
Nature Nanotechnology **12**, 631-636 (2017)

My contributions to the appended papers

I. I was the primary contributor to the calculations and the main author of the paper.

II. I was the sole author.

III. I was the primary contributor to the calculations and the main author of the paper.

IV. I contributed to the calculations and co-authored the paper. I suggested to interpret the results with the bottleneck effect. I drew the figure of the energy diagram including the electron-electron interaction.

V. I was the primary contributor to the calculations and the main author of the paper. I pushed the suggestion to view the paper in relation to explicit symmetry breaking in φ_0-junctions. This perspective is interesting since we utilized spontaneous symmetry breaking which enable switching of the supercurrent direction.

VI. I was the primary contributor to the calculations and the main author of the paper. I performed the COMSOL Multiphysics simulations, the numerical calculations of the coupling constants and the frequency tuning.

VII. I suggested to use the bifurcation continuation software MATCONT to simulate the bifurcation diagram. My simulations led me to suggest that the initiation of torus dynamics via the Neimark-Sacker bifurcation was related to the experimental findings. I performed the fitting of the model to the amplitude response and bifurcation diagrams. Furthermore, I was the main author of the supplementary material related to the theoretical modeling. I also made suggestions to the main manuscript.

Contents

Chapter 1

Introduction

"There's plenty of room at the bottom."

Richard Feynman

Nanoelectromechanical systems (NEMS) combine electron dynamics with mechanics, at the nanoscale. These systems often take the form of mechanical resonators made from suspended membranes or beams (Fig. 1.1). The reasons to study NEMS are many. To begin with, they are of fundamental interest since they constitute an excellent platform to explore the transition between classical and quantum physics. One way to address this question is to cool down the system and study the dynamics as the system comes closer and closer to its quantum ground state [1]. This typically requires a temperature below 1 mK. Ultimately, it allows for manipulation of single mechanical quanta [2]. Furthermore, the quantized nature of charge becomes important at the nanoscale. To enclose several electrons into a nanosized confinement often requires large amounts of energy due to Coulomb repulsion and the electrons can therefore block each other. As a result, single electron phenomena such as Coulomb blockade are often observed and utilized in NEMS devices [3].

From an application point of view, NEMS are interesting since they can be used in nanoelectronics e.g. as electric filters [4], transmitters [5] and receivers [6]. For these applications, *nano*structures might be important since smaller components typically have larger sensitivity and

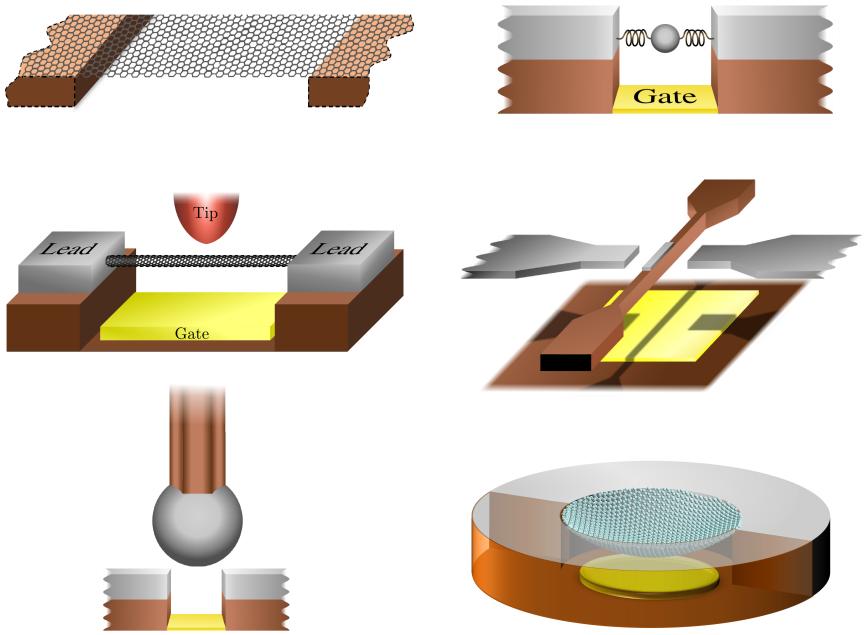

Figure 1.1: Different types of suspended nanoelectromechanical structures. In each example, one part of the structure is suspended and can vibrate mechanically. The vibrating part is typically a beam or a membrane and can exchange electrons with nearby conducting parts of the structure. Non-conducting material (brown) act as support for the vibrating part and isolate it from a gate electrode. The gate voltage can manipulate the charge on the suspended part in order to operate the function of the device.

consume less energy [7], which saves battery time. Smaller and more energy efficient components are also crucial to avoid overheating of increasingly thinner and more component dense devices. Nanoresonators are also promising for sensor applications. NEMS can be utilized to measure charge [8] and tiny forces [9]. Furthermore, a mass spectroscopy NEM-sensor with a sensitivity corresponding to one proton mass has been reported [10]. The function of the sensor is based on the following idea: when for example an air molecule lands on a vibrating NEMS, the particle adds some mass to the resonator which shifts its vibrational frequency. By detecting this shift and possibly also electronic changes, the electromechanical resonators can ultimately be used as artificial noses to detect for instance hazardous gases. The smallness of nanosystems

naturally gives them high sensitivity. Furthermore, smaller and lighter structures also lead to higher vibrational frequencies, which may enable faster technologies.

Material properties quantitatively affect the response of NEM resonators. Suspended graphene and carbon nanotubes have been extensively used in experimental studies. Such carbon structures have several favorable and extraordinary properties[1]. Most importantly, they have widely tunable frequencies [11] and high quality factors[2]. A promising parallel research activity for two-dimensional materials such as graphene is to stack layers into heterostructures [12]. Such heterostructures have been used as mechanical resonators [13]. These artificial materials exhibit new properties which can be tailored by the stacking composition. The success of these new materials will likely not be determined by how they can improve existing technologies, but by which completely new technologies the materials enable.

This compilation thesis treats the theoretical modeling of the nonlinear dynamics in suspended nanosystems as those in Fig. 1.1. In contrast to cooling down the systems, as mentioned above, I will focus on actuation of mechanical vibrations and the response of strongly driven resonators. To drive the mechanical motion in the systems of the appended papers, we have utilized both resonant and nonresonant actuation mechanisms. These mechanisms rely on the relatively strong interaction between mechanical vibrations and charges in NEMS [14, 15]. When a mechanical resonator is strongly driven, nonlinear effects will drastically influence its response. The nonlinearities in NEMS are often of geometric or electrostatic origin. These nonlinearities not only affect the single-mode response but also couple different vibrational modes and ultimately make the dynamics chaotic. From an application point of view, nonlinearities have generally been aggravating; linear systems are easier to characterize and control. However, the advancing experimental control of NEMS and increasing computational power have made nonlinear nanomechanics a highly interesting topic. Nonlinear phenomena are no longer unwanted complications which we try to limit. The question for nonlinear NEMS is rather how we can make the nonlinearities stronger, tailor [16] and utilize them in applications [17]. One

[1]The electrical and mechanical properties of carbon materials will be further discussed in the next chapter.

[2]The quality factor is a measure of how much energy is lost during one oscillation compared to the energy stored in the oscillation.

category of strongly nonlinear devices are graphene resonators due to their exceptional thickness. Graphene resonators are therefore highly interesting for studies of nonlinear dynamics.

The tunable frequencies and nonlinearities of NEMS in combination with their high quality factors enable access to exotic dynamical regions[3]. However, to find and understand these regions by standard experimental techniques can be very time consuming. Furthermore, nonlinear dynamical features can be *hidden* due to the complexity of coupled nonlinear systems. To experimentally find the hidden exotic dynamics might therefore require special treatment. An important question is how we can resolve such issues and advance the mastery of NEMS in order to explore their full nonlinear dynamics[4].

1.1 Aim of Thesis

The aim of this thesis is to introduce the reader[5] to the field of nanoelectromechanical resonators. It also attempts to give a brief intuitive explanation of the physics in the different papers: what the main mechanisms are and how they work. Understanding of these mechanisms will make the reader better prepared to read the appended papers. The interested reader is referred to these papers and their supplemental materials for more technical details, techniques and derivations. When needed, complementary calculations and details will be presented in appendices[6]. However, the main body of this thesis will focus on how the appended papers fit together, how they relate to the research field of NEMS, the most important physical mechanisms and the main results of the papers.

1.2 Outline

In the next chapter, I will describe some important electrical and mechanical properties of suspended carbon structures and how the dynam-

[3]Such as codimension-two bifurcations which require simultaneous adjustment of two parameters.

[4]An impatient reader may (cautiously) jump to conclusions (chapter 6), where I discuss how the mastery of nonlinear NEMS might be accelerated.

[5]The reader is assumed to have some basic training in physics. However, to (hopefully) make this introductory text more accessible, the amount of equations and technical details have consciously been kept low.

[6]The appendices have been published in a slightly different form in my Licentiate thesis [18].

ics of nanostructures can be described by both classical and quantum models. I will also discuss different resonant techniques of how mechanical vibrations can be actuated and what basic response is typically observed in nanoresonators.

In chapter 3, I extend the discussion of actuation mechanisms to include nonresonant ones. These mechanisms rely on the delayed electromechanical back action in the system.

In chapter 4, I present an example of how actuated mechanical vibrations can be exploited. Namely, I describe how parametric actuation of mechanical vibrations can be utilized to generate a supercurrent between two superconducting leads, even though the phase difference between the leads are zero.

In chapter 5, I continue on the topic of actuated mechanical vibrations by discussing nonlinear mode interaction. To begin with, I describe the frequency tuning and strength of nonlinear mode coupling for circular garaphene resonators. This tunability is then utilized to tune two vibrational modes of a multi-layer graphene resonator into a strong coupling regime, called internal resonance. The internal resonance does not only strongly affect the driven response of the resonator, but also drastically alter the dissipation of the modes.

Chapter 2

Nanoelectromechanics

"All models are wrong;
some models are useful."

George Box

Nanoelectromechanical systems (NEMS) [19] combine mechanics and electron dynamics at the nanoscale. In this thesis, I am mainly interested in understanding electromechanical actuation mechanisms and nonlinear mode interactions in nanosystems. The systems to have in mind are suspended structures such as the schematic ones in Fig 1.1 and the physical one in Fig. 2.1. The suspended parts can vibrate and are electrically connected to electrodes so that electrons can be exchanged between the components. Gate electrodes can both statically and dynamically adjust the charge of the vibrating parts.

To model these systems, several questions regarding the involved dynamics have to be addressed. How much can the dynamics be simplified without losing the power to explain the interesting dynamical features? What is the origin of the electromechanical coupling? Do some parts have to be treated quantum mechanically? Are nonlinear effects important and, if so, what is the origin of the nonlinearity? Appropriate mathematical models then have to be constructed which comply with the requirements.

To simplify the theoretical description, phenomenological equations are often used. When proposing a phenomenological model, it is important to examine if the model parameters can be realized by existing ex-

perimental methods. If not, new materials or measurement techniques may be required to detect the predicted phenomena. In many situations, the carbon materials graphene and carbon nanotubes (CNTs) have proven themselves to be good candidates for nanomechanical resonators[1].

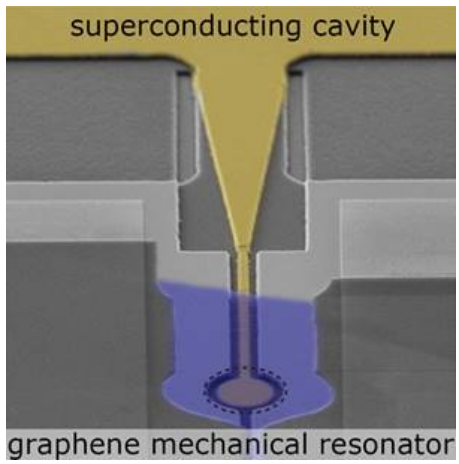

Figure 2.1: Scanning electron microscopy (false-color) image of a circular graphene resonator. The mechanical resonator is coupled to a superconducting cavity for sensitive displacement measurements [24]. Graphene resonators are often called nanomechanical drums since their mechanical behavior is similar. The figure was provided by Professor Adrian Bachtold.

Below, I will discuss some of the electrical and mechanical properties of these carbon materials and introduce some models which we have in our toolbox to describe the dynamics of NEMS. The different models constitute building blocks which can be fitted together in a plethora of ways in order to describe different kinds of dynamics in NEMS.

2.1 Electronic Properties and Models of Nanostructures

Graphene [25, 26] is a two-dimensional material constituted of a single layer of carbon atoms. The electrical properties of graphene can to a good approximation be deduced from p-orbitals perpendicular to the graphene membrane. Tight-binding calculations for the dispersion of the p-orbitals predict linear so called *Dirac cones* at each corner of

[1]Other materials such as aluminum [20], gallium arsenide [21], black phosphorus [22] and silicon nitride [23] are also being used but will not be discussed further in this thesis.

the hexagonal Brillouin zone. As a consequence, the Fermi velocity in graphene is constant $v_F \approx 10^6$ m/s and the carrier type can easily be controlled by electrostatic or chemical doping. The charge carriers in graphene exhibit high charge carrier mobility which may exceed 10^6 $cm^2V^{-1}s^{-1}$ [27]. There is no bandgap in graphene since the valence and conduction bands touch at the Dirac points. However, several ways to open a bandgap in graphene structures have been proposed since many applications rely on semiconducting transport [28].

Properties of materials at the nanoscale can often be counterintuitive. As an example, graphene is an extraordinary good absorber of light, yet it is almost completely transparent ~ 98 % [29]. This is because graphene is only a single atom thick. Piling up several layers of such a strong absorber quickly reduces the transparency of multi-layer graphene.

The electrical properties of graphene can be drastically modified by wrapping it into carbon nanotubes (CNTs) [30]. CNTs are typically a micrometer long but only a few nanometers in diameter. The almost atomistically short circumference of a CNT imposes strong quantization of the electronic wave functions in this direction. CNTs are therefore often referred to as one-dimensional objects. In contrast to graphene, CNTs can be either metallic or semiconducting with a bandgap of up to $\sim$ 1 eV, depending on the chiral angle and the diameter of the tube [31].

The electronic properties of both graphene and CNTs make them useful for transport of charge. Below, I will briefly summarize the models for charge transport used in the appended papers.

2.1.1 Equivalent Circuit Model

The equivalent circuit model is very useful to describe electronic transport, mainly because of its simplicity. In the circuit model[2], the dynamics of the electronic subsystem is mapped to an electric circuit which captures the qualitative features of the original system. This is done by lumping the physical elements of the original system into their corresponding electronic elements such as resistances and capacitors.

The procedure reduces the complexity of the interacting charge densities and replaces the system with a simple effective circuit. For instance, in Fig. 2.2 the insulating oxide layers between the graphene

[2]Also called *lumped element model* or *capacitance model*.

membrane and the electrode leads can be modeled as resistors while the membrane and backgate constitute an effective capacitor. The appropriate values of the lumped elements can in principle be calculated by considering the geometry and by solving Maxwell's equations with appropriate boundary conditions [32]. However, in practice the values are extracted by fitting the theoretical model to experiments or by crude order-of-magnitude estimations. One strategy is to view the graphene membrane and the backgate as the two plates of a parallel plate capacitor which gives the capacitance $C = \epsilon_0 A/d$ where ϵ_0 is the permittivity of vacuum, A is the area of the plates and d is the distance between them.[3] This strategy neglects the curvature of the membrane if it is pulled towards the gate by an applied electric field.

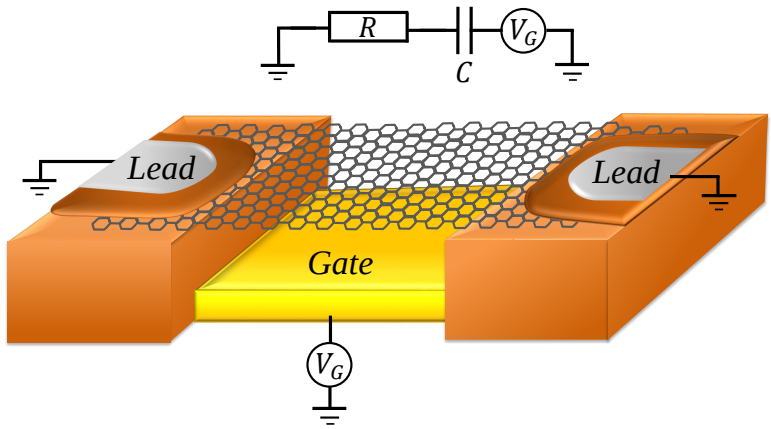

Figure 2.2: In the circuit model, the physical system (bottom) is replaced by an effective electric circuit (top). In this case, the oxide layers between the conducting leads and the graphene membrane have been modeled as a resistor. The electrostatic interaction between the graphene sheet and the gate has been modeled as a capacitance. The electric dynamics of the system has thereby been reduced to a driven RC-circuit.

In the circuit model, the graphene sheet is assumed to be a good conductor and the total resistance is therefore dominated by the oxide layers. Hence, when charges enter the graphene membrane via the oxide layers, they are assumed to immediately redistribute to cancel potential differences within the membrane. Since we are not interested in biasing

[3] In our considerations the graphene membrane is assumed to be large, chemically doped and suspended at a relatively large distance from the gate electrode so that the electronic band structure can be disregarded.

the two leads with different voltages, we may reduce the two contacts to a single effective resistance R.

When the corresponding electric circuit has been formulated, the dynamical equations are obtained by standard circuit analysis [33]. For our simple system, the current through the oxide layers is directly obtained by Ohm's law

$$\dot{q} = \frac{1}{R}\Big(V_{\rm G}(t) - \frac{q}{C}\Big), \tag{2.1}$$

where q is the charge on the membrane, $V_{\rm G}(t) = V_0\cos(\Omega t)$ is the alternating gate voltage and q/C is the potential drop over the capacitor. The equation tells us that if the gate voltage is changed, the charge of the membrane will reach its new equilibrium on a time scale given by the RC-time $\tau_{\rm RC} = RC$.

2.1.2 Semiclassical Model of Charge Transport

In paper III, we will focus on externally driven charge oscillations within the graphene membrane. We can therefore no longer view the membrane as a lumped component as we did in the circuit model. To describe the driven oscillations of the distributed charge density, we will instead adopt a simple semiclassical model of a suspended chemically doped graphene sheet (Fig 2.3**a**).

As a start, let us assume that we apply a weak electric field $E_{\rm ext}(x,t)$ along the x-direction. The electrons will be accelerated[4] by the external field and result in a finite current density $j(x,t)$. If the external field is inhomogeneous, it will generate a slight separation of charges in different regions, i.e., an inhomogeneous charge density $\varrho(x,t)$ (Fig. 2.3**b**). The separation will give rise to an internal electric field $E_{\rm int}(x,t)$, as the charges in the positively and negatively charged regions attract each other with Coulomb forces. The internal field can be calculated by summing up the fields from charged infinite wires placed next to each other,

$$E_{\rm int}(x,t) = \frac{1}{2\pi\epsilon_0}\mathcal{P}\int_{-\infty}^{\infty}\frac{\varrho(x',t)}{x-x'}{\rm d}x' \tag{2.2}$$

where ϵ_0 is the vacuum permittivity and $\mathcal{P}$ denotes the principal value of the integral. The internal field will counteract the separation of charges and contribute to the total electric field $E(x,t) = E_{\rm ext}(x,t) + E_{\rm int}(x,t)$.

[4]For simplicity we assume the dynamics to be homogeneous in the y-direction.

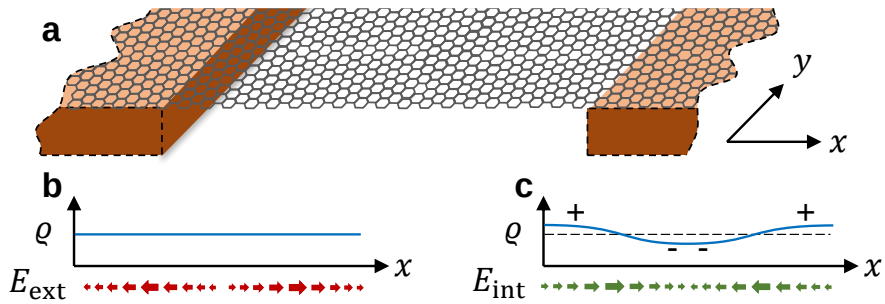

Figure 2.3: **a** Cross-section of a doped suspended graphene sheet. **b** An external electric field E_{ext} is applied to the homogeneous charge distribution. **c** The induced inhomogeneous current will polarize the membrane. The separation of charge then creates an internal electric field E_{int} which counteracts the external field.

The damped charge dynamics driven by the electric field can be modeled by the semiclassical equation[5] [34]

$$\frac{\partial}{\partial t} j(x,t) + \nu_{\text{R}} j(x,t) = \frac{e^2 E_{\text{F}}}{\hbar^2 \pi} E(x,t), \tag{2.3}$$

where ν_{R} is the relaxation frequency mainly due to disorder [35] and E_{F} is the Fermi energy in the graphene sheet. Furthermore, the charge density has to obey the continuity equation

$$\frac{\partial}{\partial t} \varrho(x,t) = -\frac{\partial}{\partial x} j(x,t) \tag{2.4}$$

which assures conservation of charge.

2.1.3 Quantum Tunneling Models

Charge transport in nanostructures incorporating so called *quantum dots*[6] (QDs) may exhibit strong quantum effects and can then not be described by classical models. The charge dynamics of a QD can be reduced to include only a few quantum levels by shrinking its size, since

[5] The semiclassical equation can be obtained by a relaxation-time approach starting from the Boltzmann equation and deriving hydrodynamic equations [34, 35]. Inter-band excitations have been neglected since these are suppressed at low temperature $k_{\text{B}}T \ll E_{\text{F}}$ and external field frequencies which are not too high $\hbar\Omega < 2E_{\text{F}}$.

[6] Typically made of small metal or semiconductor grains.

this increases the separation of the energy levels due to space quantization. Furthermore, charging effects become very important when electrons are confined into a small volume. For small structures, electrostatic interaction significantly contributes to and rearrange the separation between energy levels. The charging energy associated with confining the charge q on a structure with capacitance C is $E_{\mathrm{C}} = q^2/(2C)$ and therefore depends on the geometry of the QD. The structure will operate as a few level quantum dot if the thermal energy $k_{\mathrm{B}}T$ and the energy accessible from other sources[7] are comparable to or smaller than the separation of electronic energy levels. Furthermore, quantum dots are often coupled to other systems such as conducting leads, so that electrons can be exchanged by quantum tunneling. In what follows, I will describe three models for different kinds of quantum dots.

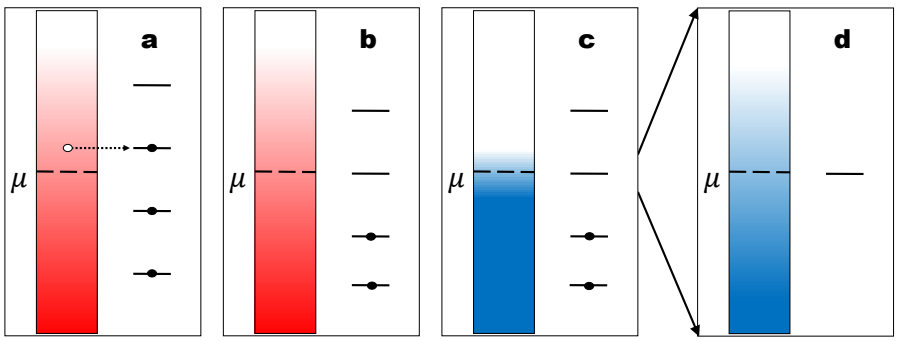

Figure 2.4: **a** The non-interacting single-electron energy levels (black bars) of a quantum dot are in tunneling contact with a continuum of electronic states in a nearby reservoir. The population of electrons in the reservoir is smeared due to finite temperature as indicated by the color gradient. The tunneling coupling allows electrons to tunnel (dashed arrow) from filled levels to empty levels. **b** The energy levels can be adjusted by applying an electric field. An interesting situation occurs if we tune one of the levels close to the chemical potential μ of the reservoir. **c** If we decrease our energy sources such as temperature, we will only access and be able to change the level closest to the chemical potential. We can thereby "zoom in" on the relevant energy scale of the dynamics and disregard the other energy levels.

[7]Such as voltage biasing energies eV or photon energies $\hbar\omega$.

Single-Level Quantum Dots

An important kind of quantum dot is the single-level quantum dot (SL-QD) where only one electronic level contributes to the electron dynamics on the dot (Fig. 2.4). Single-level quantum dots can be achieved by applying a static voltage to the QD in order to cancel the charging energy associated with adding one electron to the dot. In that case, the neutral state of the QD and its state with one excess electron can be very close to degenerate. In such a situation, manipulation between the empty and filled single-electron level can be achieved without involving other electronic states. This is because the other states require access to much larger energies.

The time-evolution of a quantum system is governed by the Liouville-von Neumann equation

$$i\hbar\partial_t\hat{\rho} = [\hat{H},\hat{\rho}], \tag{2.5}$$

where $\hat{\rho}$ is the density operator of the quantum system and $\hat{H}$ is its Hamiltonian operator which corresponds to the energy of the system. The Hamiltonian, which dictates the dynamics, can be built up by the following reasoning.

Let us start with the uncoupled single-electron level of the QD and denote its energy ϵ_{Dot} counted from the chemical potential in reservoir. If the level is occupied by an electron, we have to add ϵ_{Dot} to the total energy. In the language of second quantization [36] we can write the corresponding term in the Hamiltonian as

$$\hat{H}_{\text{SL-QD}} = \epsilon_{\mathrm{Dot}}\hat{d}^\dagger\hat{d} \tag{2.6}$$

with creation and annihilation operators $\hat{d}^\dagger$ and $\hat{d}$, respectively. For simplicity, we disregard spin degeneracy which can be lifted by for instance a magnetic field.

The QD is often coupled to a conducting lead which serves as a bulk[8] reservoir for electrons. The leads are often so large that the discreteness of their electronic levels can be neglected. The uncoupled reservoir is described by the term

$$\hat{H}_{\mathrm{Lead}} = \sum_k \epsilon_k \hat{l}_k^\dagger \hat{l}_k \tag{2.7}$$

[8] We will neglect surface effects such as localized states due to the edge and defects.

where $\hat{l}_k$ is the annihilation operator of an electron[9] with energy ϵ_k in the leads.

Electrons can tunnel to and from the QD and thereby change its state. We can mathematically describe this by coupling the dot state to the reservoir states via quantum tunneling with the term

$$\hat{H}_{\text{Tunneling}} = -\sum_k \mathcal{T}\left(\hat{l}_k^\dagger \hat{d} + \hat{l}_k \hat{d}^\dagger\right), \tag{2.8}$$

where $\mathcal{T}$ is the tunneling strength. It represents the energy associated with delocalization of the electron between the coupled states. The tunneling strength $\mathcal{T}$ depends on the spatial overlap of the involved wave functions in the uncoupled electron levels. As a consequence, $\mathcal{T}$ typically decreases exponentially with distance x between the dot and the reservoir, $\mathcal{T} \propto \exp(-x/\lambda)$. Here, λ is the characteristic tunneling length[10] which is usually on the order of 1 Å [37]. The operator $\hat{l}_k \hat{d}^\dagger$ will annihilate an electron in the reservoir state $|k\rangle$ and create an electron in the dot state $|d\rangle$. In total, the number of electrons is conserved.

The Hamiltonian of the coupled electronic system constituted by the single-level quantum dot, the lead and the tunneling coupling is then given by summing up the contributions $\hat{H} = \hat{H}_{\text{SL-QD}} + \hat{H}_{\text{Lead}} + \hat{H}_{\text{Tunneling}}$.

Multi-Level Quantum Dots

In multi-level quantum dots (ML-QDs), there is at least one more electronic level which contributes to the charge dynamics. We will later be interested in a two-level QD. To write down its Hamiltonian we start by adding two non-interacting single-level quantum dots according to Eq. (2.6). However, an important modification is usually needed if the dot is occupied by two electrons simultaneously. Namely, the doubly-occupied state is associated with the additional energy U due to electron-electron interaction. The Hamiltonian for the two-level quantum dot can be written in the form

$$\hat{H}_{\text{ML-QD}} = E_1^\uparrow \hat{n}_\uparrow + E_1^\downarrow \hat{n}_\downarrow + U \hat{n}_\uparrow \hat{n}_\downarrow \tag{2.9}$$

[9] Or quasiparticle, i.e., a "dressed electron" where electron-electron interaction within the lead has been taken into account.

[10] Simple scattering models show that the tunneling length depends on the work function U_{w} of the material and the energy E of the electron as $\lambda = \hbar/\sqrt{8 m_{\text{e}} |E - U_{\text{w}}|}$ with electron mass m_{e}. However, the energy dependence can often be neglected since U_{w} is typically on the order of electron volts [37], which for us is a huge energy scale.

where we have labeled the two-levels with spin-arrows. The index "1" refers to a *non*-interacting level. The number operator $\hat{n}_\sigma$ gives a contribution to the total energy if there is an electron of spin σ on the dot. The two-level QD can be in four states; the charge-neutral state $|0\rangle$, the single-populated states $|\uparrow\rangle$ and $|\downarrow\rangle$ with opposite spins, and the double-populated state $|2\rangle$.

Interacting electrons are somewhat more complicated to describe than non-interacting particles. In the non-interacting electron picture, we see all electronic levels as independent and we can add and remove electrons without changing the positioning of the levels. All we need is to fulfill the Pauli exclusion principle, which states that two electrons cannot occupy the same state (Fig. 2.5). However, if the electrons interact, the independent-level language does not apply. Instead, we have to consider the dynamics of the complete quantum states (Fig. 2.5**c**).

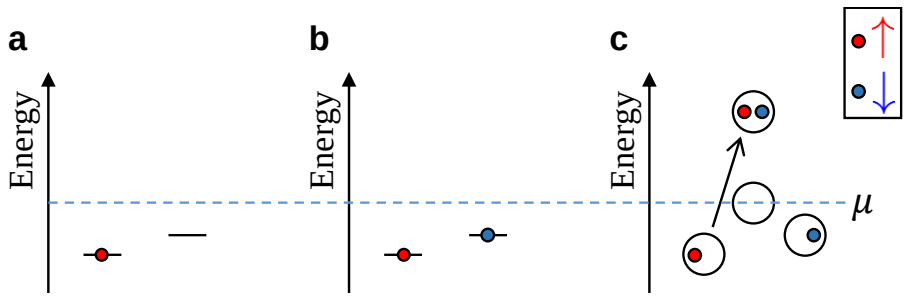

Figure 2.5: **a** In the non-interacting electron picture we can represent the (non-degenerate) electron levels as bars. The dynamics can be imagined as electrons jumping in and out of an electronic reservoir without changing the positions of the levels. However, for interacting particles the energy of an electron depends on the population of other electronic states and the levels will no longer be static. Instead of considering independent *levels*, we should describe the complete *states* of the QD indicated by the circles in **c**. Note that the circles describing the neutral and double-populated state are *not* electron levels. As an example, let us assume that we have a non-interacting system in the state $|\uparrow\rangle$ shown in **a**. If we add a spin-$\downarrow$ electron to the dot, we arrive in the double-populated state shown in **b**. However, if the electrons interact, the process of adding a spin-$\downarrow$ electron brings us from the lower circle, representing $|\uparrow\rangle$, to the upper double-populated circle. In order to get there, we need to pay the additional interaction energy U, which in this case brings us above the chemical potential μ of the reservoir.

Single-Cooper-Pair Quantum Dots

If a quantum dot is cooled to low temperatures it might become superconducting depending on its material properties. In such a case, electrons in the leads and dot condensate and form Cooper pairs. The system will in some respects behave similar to a normal-conducting junction, but the role of electron tunneling is replaced by tunneling of Cooper pairs.

A simple case of a single-Cooper-pair quantum dot coupled to a superconducting lead can be obtained by the following qualitative description[11]. Let us assume the dot to be properly tuned so that only its neutral state $|0\rangle$ and state with one excess Cooper pair $|1\rangle$ are involved in the dynamics. The energy of the charged state $-2eV_0$ can be adjusted by the gate voltage and corresponds to the Hamiltonian term

$$\hat{H}_{\mathrm{CPB}} = -2eV_0|1\rangle\langle 1|. \tag{2.10}$$

One way to represent the condensed state of the superconducting reservoir is by the coherent superposition

$$|\phi\rangle \propto \sum_N e^{iN\phi}|N\rangle_{\mathrm{R}}, \tag{2.11}$$

where N is a measure of how many Cooper pairs there are in the superconducting reservoir and ϕ is the *superconducting phase* of the reservoir. In the same representation we can write the tunneling[12] coupling for Cooper pairs as

$$\hat{H}_{\mathrm{Tunneling}} = -\frac{\hbar\omega_{\mathrm{J}}}{2}\sum_{N'}|N'\rangle_{\mathrm{R}}\langle N'+1|_{\mathrm{R}} \otimes |1\rangle\langle 0| + \text{Hermitian conjugate}. \tag{2.12}$$

The term which is written out represents tunneling of a Cooper pair from the reservoir to the dot. This process is associated with the Josephson tunneling energy $\hbar\omega_{\mathrm{J}}$.

Next, we will see how the superconducting system can be reduced to a two-state Hamiltonian system. If we apply the tunneling Hamiltonian on the condensate state (Eq. (2.11)), we obtain terms of the

[11] For a more thorough description, the reader is referred to Ref. [3].

[12] In principle, excitation and tunneling of quasiparticles also take place. However, these processes are heavily suppressed when avaiable energy scources such as thermal fluctuations are much smaller than the superconducting gap 2Δ where Δ is the superconducting order parameter [3].

form $\sum_{N'} |N'\rangle\langle N'+1||\phi\rangle = e^{i\phi}|\phi\rangle$. Hence, the condensate state is an eigenstate to the tunneling operator and we can replace the tunneling operator by the complex number $e^{i\phi}$. Therefore, we do not have to write out the lead subsystem and can reduce the Hilbert space to a two-state system [38]. We can simply view these tunneling processes as "picking up" the superconducting phase ϕ.

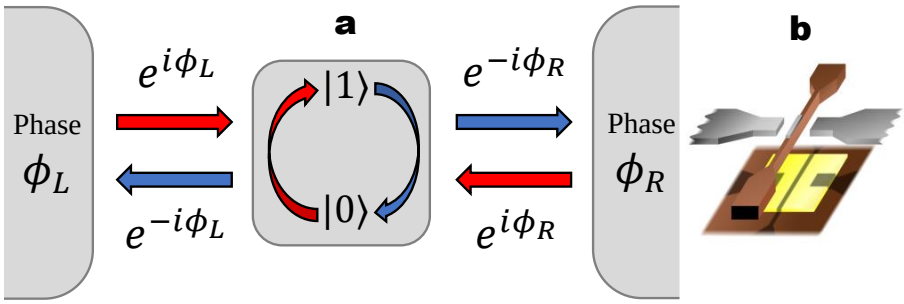

Figure 2.6: **a** A single-Cooper-pair box between two superconductors. Tunneling of Cooper pairs to the dot (red arrows) brings the CPB from its neutral to its charged state by picking up the phase of the involved superconducting reservoir. **b** Suggestion for an experimental realization of the system.

Let us put our single-Cooper-pair quantum dot, also called *single-Cooper-pair box* (CPB), in a junction between two superconductors where Cooper pairs can tunnel between the leads via the box (Fig. 2.6). Since only the phase difference between superconductors have physical meaning, it is convenient to introduce the phase difference $\Delta\phi$ and take $\phi_L = -\phi_R = \Delta\phi/2$. The resulting Hamiltonian[13] takes the form

$$\hat{H} = -2eV_0|1\rangle\langle 1| - \hbar\omega_J \cos(\Delta\phi/2)|1\rangle\langle 0| + \text{Hermitian conjugate.} \quad (2.13)$$

Hence, the dot and lead dynamics have been reduced to that of a two-state Hamiltonian system. This is not possible in a normal-conducting tunnel junction. The important difference is that in the superconducting case, the electrons in a lead form a condensate which is a single well-defined state, while the electrons in the normal-conducting case are in an incoherent mixture of states. A coherent superposition between the reservoir states and the dot states is therefore only possible in the superconducting case. An important experimental advance was to coherently manipulate the states of a single-Cooper-pair box [39, 40].

[13]For simplicity we assume the tunneling strength to the left and right superconductors to be the same.

2.2 Nanomechanics of Suspended Structures

In this section, I will first comment on the mechanical properties of carbon materials and then more generally discuss the mechanics of suspended nanostructures.

The mechanical properties of graphene and carbon nanotubes (CNTs) originate from the strong sp^2-hybridised σ-bonds between the carbon atoms [30]. These σ-bonds make the materials some of the stiffest[14] materials known with a Young's modulus of up to 1 TPa for CNTs [41].

Suspended carbon nanostructures have high vibrational frequencies[15] due to their high stiffness and low mass. The vibrational frequency of suspended graphene is typically on the order of 100 MHz. The frequency of a suspended CNT is usually higher, due to its more rigid structure. However, the frequencies heavily depend on the geometry, type of clamping and tension T. An important case is the vibrational frequency of the fundamental mode of a circular graphene drum, which can be estimated by the frequency of a stressed membrane

$$\omega_{\mathrm{m}} \approx 2.4\sqrt{\frac{T}{\rho_0 R^2}} \tag{2.14}$$

where $R \sim 1$ μm is the radius and $\rho_0 = 0.75$ mg/m^2 [42] is the two-dimensional mass density of graphene.

In experimental realizations, the parameters of a vibrational mode can be difficult to calculate accurately since the geometries[16] can be complicated and the built-in stress from fabrication might be non-uniform (Fig. 2.7). Furthermore, the structures may contain grain boundaries and defects, which affect the elastic properties of the suspended structure. To circumvent these complications, in theoretical

[14]Several times stiffer than steel. The stiffness of CNTs typically decreases with increasing tube diameter which has been addressed to rippling effects [41].

[15]The high vibrational frequencies of NEMS are interesting for high frequency electromechanical applications. High frequencies are also favorable when trying to reach the ground state, since the thermodynamic energy $k_{\mathrm{B}}T$ has to be much smaller than the vibrational quantum $\hbar\omega_{\mathrm{m}}$.

[16]The geometry of graphene resonators are typically circular drums clamped around the circumference or ribbons clamped at the suspension points. Graphene ribbons often suffer from ill-defined modes along the free edges [43] which complicates the dynamics and degrades the quality factor [44]. This problem is circumvented in circular fully-clamped structures. Carbon nanotubes can be clamped at either one or two ends. One benefit of the double clamped structure is that the two ends can be voltage biased, allowing for charge transport through the suspended part.

modeling, phenomenological equations for the vibrational modes are often used where the parameters are fitted to experimental data.

Despite the extraordinary stiffness of the carbon materials, especially graphene should be thought of as an elastic membrane rather than as a stiff metal plate. This is because graphene is ultimately thin, which results in an exceptionally low bending rigidity. Furthermore, graphene can be stretched $\sim$ 10 % of its length before breaking [45], which is remarkable since it is a one atom thick *crystalline* material, in contrast to an elastic membrane of folded polymers. The possibility to stretch the resonators without breaking them makes it possible to realize tunable nanomechanical resonators. By applying an external load, for example by an electric field, the tension in the resonating structure can be increased, which then increases the vibrational frequencies. The same phenomenon is used when the strings of a guitar are tuned.

Both graphene and carbon nanotubes have been modeled by continuum elasticity theory with great success [46]. The general idea of the theory is to write down expressions for the energy costs associated with deformations and then derive dynamic partial differential equations for the motion of the structure[17]. The first step to solve the resulting equations is to find the static solution where the stresses in the structure cancel external forces. Furthermore, linear theory is sufficient if the dynamics is restricted to small amplitude of oscillations and the equations are therefore linearized around the static deflection. The problem is then reduced to finding the discrete frequencies and spatial mode shapes of the suspended structure.

For higher vibrational amplitudes, nonlinear effects become important. It is worth mentioning that the nonlinearities in graphene resonators are usually of geometric and electrostatic origin and not due to nonlinear elastic forces between the carbon atoms. However, it is possible to reach the nonlinear elastic regime [45]. Nonlinearities will not only influence the dynamics of single modes but also couple different vibrational modes. The nonlinear dynamics of NEMS will be discussed further in chapter 5. However, for many purposes, knowledge of the full nonlinear dynamics of vibrational modes is not necessary. It is often enough to model the mechanical subsystem as a single harmonic oscillator.

[17] The energy contributions are often separated into a stretching and a bending component. The bending component is important for suspended CNTs but can often be neglected for graphene resonators.

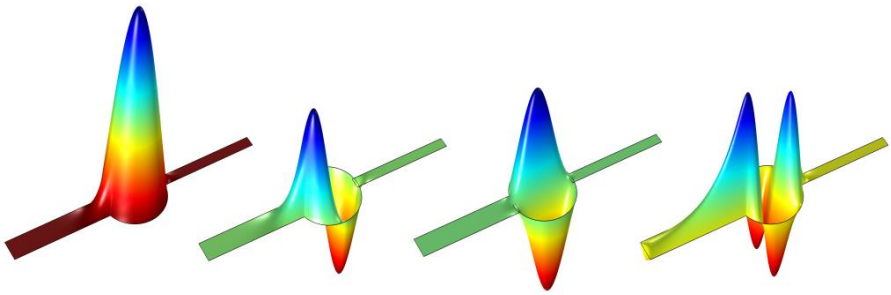

Figure 2.7: The four lowest spatial modes for a gated membrane with the geometry of the experimental drum in Fig. 2.1. The mode shapes were obtained by Comsol Multiphysics simulations. The structure has a trench so that the backgate can be contacted via a conducting wire. Another reason for the trench is that it allows air to escape when the pressure is lowered. The spatial profiles of the vibrational modes resemble the Bessel modes obtained for uniformly stressed circular membranes. However, the trench breaks the circular symmetry and lifts the degeneracy of the second and third mode. The degeneracy is also lifted if the built-in stress is non-uniform. Such asymmetries can complicate the identification of vibrational modes in experiments [47] but may also give additional information about the structure. If a circular graphene membrane is non-uniformly pre-stressed, the asymmetry can be tuned by electrostatic gating [22]. Special designs for resonators can be achieved by utilizing the tunable anisotropy [48].

It is not obvious that continuum elasticity theory, originally developed to describe macroscopic structures, is applicable to nanomaterials where influences from the atomistic structure is easier to imagine. By comparison, the electronic properties of nanostructures were drastically changed from their three-dimensional bulk values. After all, graphene is only one atom thick. However, it has been shown that continuum elastic equations for a thin plate, the Föppl-von Kármán equations[18], can be recovered by starting from an atomistic model for graphene [49]. The main assumption is the long-wavelength approximation. Namely, at a long enough length scale, the hexagonal lattice is approximately isotropic [50] and the atomistic structure can be disregarded. Remarkably, the elasticity theory agrees well with both molecular dynamics calculations [49] and experimental results [51] for graphene resonators as small as a few tens of nanometers. Similar results were found by numerical simulations of CNTs [52].

[18]The Föppl-von Kármán equations will be further discussed in chapter 5.

So, if macroscopic models can be used to also describe nanomechanical systems, why are NEMS interesting from a scientific point of view? To begin with, the mechanics in nanostructures can be coupled to electronic degrees of freedom which can be dominated by quantum effects in contrast to classical systems. Furthermore, nonlinear effects are strong in graphene resonators and one aim is to study nonlinear mechanics in the quantum limit. Another advantage of nanomechanical resonators is their exceptionally high quality factors Q which can exceed 10^6 in for instance CNT [53]. Quality factors surpassing one million were recently demonstrated (Paper VII) also for multi-layer graphene resonators. The high quality factors in NEMS give extremely sharp resonances, which makes it possible to selectively address modes or combinations of modes. Furthermore, the large separation of time scales (due to the high Q) makes room for exotic nonlinear physics where well separated time scales are required. An example of such dynamics is the internal resonance studied in Paper VII, which will be further discussed in chapter 5.

The dissipation mechanisms which limit Q in NEMS are still not fully understood. Different possible mechanisms such as thermoelastic damping [54] and clamping losses [55, 56] have been proposed. It is likely that several mechanisms are active simultaneously. If the different dissipation mechanisms can be viewed as independent "linear" dissipation channels, they can be added according to Matthiessen's rule. The total dissipation rate then becomes $\gamma_{\text{tot}} = \sum_i \gamma_i$ where the sum includes all mechanisms. However, Matthiessien's rule is often violated[19] when a resonator is driven far from equilibrium, where nonlinear dissipation mechanisms kick in [58, 59]. How linear and nonlinear dissipation can be modeled mathematically is briefly described in appendix A. Although dissipation ultimately originates from interaction with the environment, the internal structure of the system can drastically change the route of dissipation as shown in Paper VII.

[19] Matthiessien's rule is also violated for electrons in graphene [57]. The dissipation of a nonequilibrium electron distribution in graphene is first thermalized by electron-electron scattering into a hot Fermi sea on the time scale $\sim$ 100 fs. However, to dissipate the energy from the electronic system, electron-phonon scattering is needed which typically takes place on the time scale $\sim$ 1 ps. Hence, to reach equilibrium, both processes are needed and the time to get there is therefore in this case set by the slower time scale.

2.3 Origins of Nanoelectromechanical Coupling

The fundament of nanoelectromechanics is the coupling between the mechanical and electronic subsystems. The electromechanical coupling can be both strong and tunable [14] and can have different physical origins.

First of all, there is a capacitive coupling between the suspended structure and the gate electrode[20], since the capacitance depends on the distance between the components. Hence, if the structure deflects or vibrates it will affect the charge dynamics. At the same time, a charged structure will experience an electrostatic force[21] towards the gate given by

$$F = -\frac{\partial}{\partial x}\frac{q^2}{2C(x)}, \tag{2.15}$$

where the derivative should be calculated for constant charge [32]. As a consequence, the system exhibits electromechanical *back action*, since the mechanical deflection will influence the charge on the structure which in turn exerts a force acting back on the mechanical deflection.

Another electromechanical coupling is found in the position dependent tunneling coefficient $\mathcal{T} \propto \exp(-x/\lambda)$ [37], as presented in the previous section. This interaction is important when the tunneling rate between two bodies can be changed by mechanical deflection. As in the case of capacitive coupling, the suspended structure will experience an attractive force towards the conducting structure. This is because the energy of the system can be lowered by decreasing the distance between the objects. The tunneling coupling not only results in a mechanical force but also affects the electronic subsystem by changing the tunneling rate when the body is deflected. In contrast to the capacitive force, the force due to delocalization of charge via tunneling is a purely quantum mechanical phenomenon with no classical analogue. Coupling between mechanical and electrical degrees of freedom can be achieved in several other ways, but will not be discussed further in this thesis.

[20] A similar coupling can be achieved without a gate if the charge and mechanical deflection is coupled by an external electric field. We will investigate this case further in section 3.1.3

[21] The force can be viewed as a result of Coulomb attraction due to induced mirror charges in the conducting gate.

2.4 Basic Response in Nanoelectromechanical Resonators

In what follows, I will briefly describe what kind of basic response we can expect in electromechanical resonators such as the graphene drum in Fig. 2.8. As a starting point, let us set up a simple model where we combine the equivalent circuit model Eq. (2.1) with the fundamental building block — the damped anharmonic oscillator — to describe the mechanical deflection. Furthermore, let us describe the electromechanical coupling with the capacitance model Eq. (2.15).

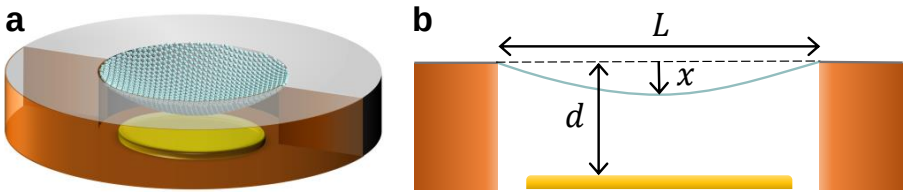

Figure 2.8: **a** Circular graphene resonator. **b** Geometrical variables of the graphene resonator. The distance to the gate d is typically 100 nm whereas the diameter L of the resonator is typically a few μm.

In many cases, the electron dynamics follows the mechanical vibrations adiabatically. This is because the dynamics of the electronic degree of freedom typically takes place on a much faster time scale than the time scale of mechanical oscillations. As a consequence, the electronic subsystem has time to relax to its equilibrium state, given by the mechanical configuration. The electronic subsystem will therefore follow the mechanical deflection adiabatically whilst the mechanical resonator slowly moves. We can therefore set $\dot{q} = 0$ in Eq. (2.1) as long as we do not apply any fast electric fields, i.e., on the time scale τ_{RC}.

To investigate the force terms which are relevant for small drive amplitudes, we linearize the adiabatic equations around the flat membrane configuration[22] and assume that the drive voltage V_d is much smaller than the static voltage V_st, which is typically the case in experiments. Our model then simplifies to

$$\begin{aligned}\ddot{x} + \gamma\dot{x} + \omega_\mathrm{m}^2 x + \eta x^3 &= \frac{1}{2m}\frac{\partial C}{\partial x}\Big(V_\mathrm{st} + V_\mathrm{d}(t)\Big)^2 \\ &\approx \frac{C_0 V_\mathrm{st}}{2m}\Big(V_\mathrm{st} + V_\mathrm{st}\frac{x}{d} + 2V_\mathrm{d}\cos(\Omega t) + 2V_\mathrm{d}\cos(\Omega t)\frac{x}{d}\Big),\end{aligned} \tag{2.16}$$

[22]The equations should be linearized around its equilibrium position, which is shifted by the electrostatic force, but that is of minor importance for the qualitative analysis we want to carry out here.

with mechanical damping γ, effective mass of the mechanical resonator m and strength η of the so called *Duffing nonlinearity* [60]. The electrostatic force (second line of Eq. (2.16)) contains four terms which will give qualitatively different response in the resonator.

The time-independent force will pull the equilibrium position of the membrane closer to the gate. The second force term, which is proportional to $V_{\mathrm{st}}^2 x$, can be absorbed into the left hand side and renormalize the vibrational frequency. By doing so, we see that the electrostatic coupling will decrease the vibrational frequency. The reason is that, as the resonator moves closer to the gate, the resonator becomes more charged and will therefore be more strongly attracted to the gate. On the other hand, as the resonator moves away from the gate, the capacitance decreases and the force towards the gate is weakened. This will effectively reduce the stiffness of the mechanical restoring force, which decreases the vibrational frequency. This phenomenon is therefore often referred to as *softening*.

However, the mechanical frequency will also stiffen due to increased tension when the membrane is stretched towards the gate by the static field. This effect is not taken into account in Eq. (2.16). In general, the frequency tuning can be a complicated combination of softening and stiffening effects, which is strongly dependent on the pre-stress induced during fabrication (Fig. 2.9). The electrostatic softening typically dominates for strongly pre-stressed graphene membranes and small gate distances $d \ll L$.

Besides the frequency tuning, another basic response observed in NEMS is the snap-to-contact phenomenon. It occurs when the membrane is pulled so strongly towards the gate that the electrostatic force overcomes the mechanical restoring force and the suspended equilibrium becomes unstable. The membrane therefore snaps into the gate, which often destroys the device. At the snap-to-contact point, the vibrational frequency tends to zero which is illustrated in Fig. 2.10. Hence, a rapidly decreasing vibrational frequency warns us when we are close to the snap-to-contact point.

The electrostatic driving terms $\propto V_{\mathrm{d}} \cos(\Omega t)$ in Eq. (2.16) can actuate mechanical vibrations. The so called *direct driving* [62], generated by the periodic force independent of x, actuates the membrane by pumping energy into the system at constant rate. When the oscillation is pumped to increasingly higher amplitudes, the intrinsic dissipation of energy also increases. Hence, the linear mechanical damping satu-

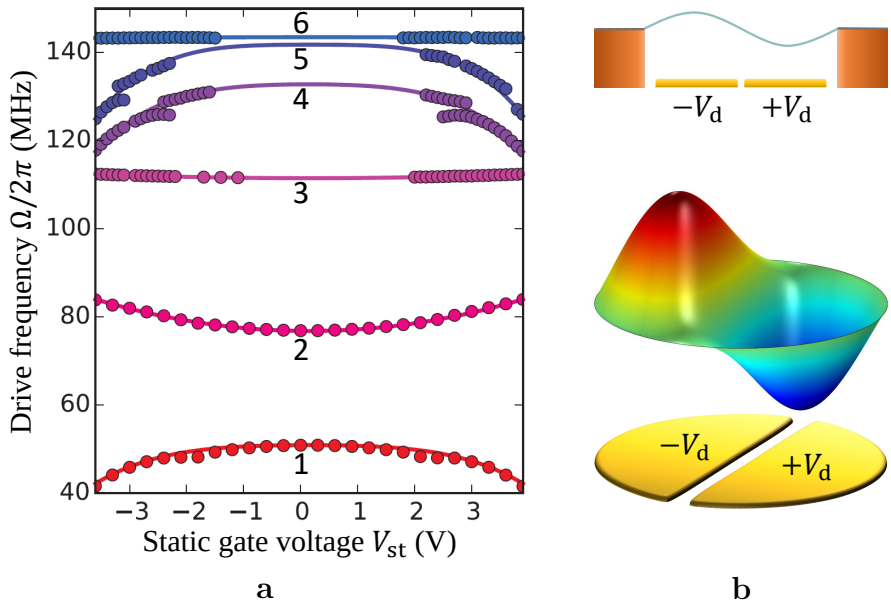

a **b**

Figure 2.9: **a** Experimentally measured vibrational frequencies, as a function of static gate voltage V_{st}, of the circular graphene drum studied in Paper VII. The fundamental (first) mode is dominated by electrostatic softening, while the second mode is stiffened. Strong drive voltage is often required to detect high vibrational modes. The reason is that the coupling between the gate and the membrane depends on the spatial overlap between the geometry of the gate and the profile of the vibrational mode. Generally, higher modes have more complex profiles, which typically leads to a reduced coupling with the gate and therefore a higher effective mass. If the gate is perfectly symmetric and the mode is anti-symmetric there is no coupling at all. Hence, devices often exhibit modes which cannot be read out by the gate and they are therefore called "dark modes". To circumvent this, multi-gate structures [61], seen in **b**, can be used to access more complex modes. A dark mode is likely the reason for the anti-crossing observed on the tuning of modes four and five in **a**.

rates the amplitude of oscillations when the dissipation rate equals the constant pumping rate. The amplitude response to the direct drive is a Lorentzian function of the detuning $\Delta\omega = \Omega - \omega_{\mathrm{m}}$ between the driving frequency and the natural mechanical frequency.

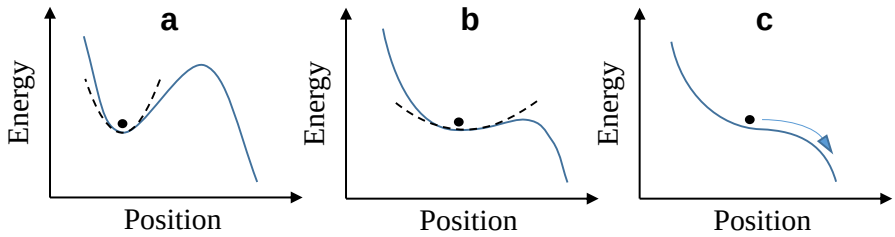

Figure 2.10: Explanation of the snap-to-contact phenomenon. The static position of the membrane is determined by the potential (solid line) resulting from the competition between mechanical and electrostatic forces. **a** The vibrational frequency of the fundamental mode is given by the effective parabolic potential (dashed line) close to the local potential minimum. **b** The frequency is tuned (here softened) by an increased static gate voltage. **c** At a critical voltage, the suspension becomes unstable and the membrane snaps into the backgate. Simultaneously, the frequency goes to zero since the local minimum becomes a saddle point and then disappears. In Fig. 2.9, the steepening frequency tuning of the fundamental mode for $|V_{\mathrm{st}}| > 3$ V is an indication that the system approaches the snap-to-contact point.

Another way to actuate mechanical vibrations is by parametric resonance [62] due to the term proportional to $V_{\mathrm{d}} \cos(\Omega t)x$. The parametric driving is strongest for the condition $\Omega = 2\omega_{\mathrm{m}}$. The energy pumped into the system by the parametric drive increases with amplitude, in contrast to the direct driving. This can be understood by the fact that the parametric force term is proportional to x, i.e., the amplitude of the oscillations. As a consequence, when the parametric drive strength is strong enough to overcome the intrinsic dissipation, the amplitude starts to increase exponentially. To saturate the vibrations above the instability point, nonlinear effects must be included in the model.

Two phenomenological ways to saturate a system driven above its instability point is illustrated in Fig. 2.11. Firstly, a nonlinear damping mechanism can enhance the dissipation at larger amplitudes and overcome the pumping, which will saturate the vibrations. Another possibility is that nonlinear effects decrease the efficiency of the pumping mechanism at larger amplitudes so that it can be balanced by the linear damping, as we will see in chapter 4. The nonlinear response

of more strongly driven resonators will be discussed in more detail in chapter 5.

Despite the simplicity of the model discussed here, it captures two very important ways of actuation commonly used to excite vibrations in NEMS [43, 14, 63, 64]: the direct and the parametric driving. Both are resonant phenomena, since the level of actuation heavily depends on the frequency detuning between the driving field and the vibrational mode. In the next chapter, I will extend the discussion to nonresonant actuation mechanisms.

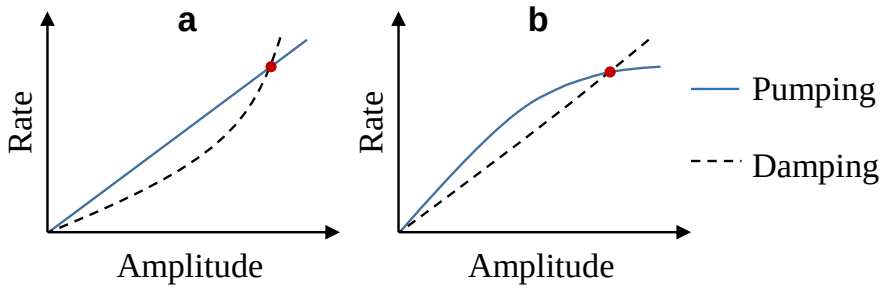

Figure 2.11: Nonlinear stabilization of excited mechanical vibrations. The amplitude of oscillations, in a system driven above its instability point, may be saturated by (**a**) nonlinear damping which takes over at large amplitudes and (**b**) a pumping mechanism whose efficiency decreases with increasing amplitude. A stationary oscillation is reached (dots) when the pumping is compensated by the damping.

Chapter 3

Nonresonant Actuation of Mechanical Vibrations

Intuitive understanding is nothing more than the confidence generated by experience.

"We have purposely trained him wrong, as a joke."
Master Tang

Mechanical actuation of suspended nanostructures often relies on external periodic forces of electrical or optical origin. In many cases, the applied force is in direct or parametric resonance with the vibrational mode frequency [43, 14, 63, 64], as discussed in the previous chapter. However, in this chapter I will focus on *nonresonant* actuation of mechanical vibrations. The actuation of a resonator will be referred to as *nonresonant* if the actuation mechanism is insensitive to the relation between the applied drive frequency and the vibrational frequency.

An example of a nonresonant actuation mechanism is the shuttle instability [65, 66, 67], which is the nanoelectromechanical analogue of the Gordon-Franklin bell [68]. When a movable conducting particle on a cantilever is situated between two voltage biased electrodes, the stationary position of the particle becomes unstable and it starts to shuttle charge between the electrodes. Mechanical so called *self-oscillations* of the particle is thereby actuated at its natural frequency, even though the much lower frequency (often equal to zero) of the drive voltage is far out of resonance.

In optomechanical devices, nonresonant actuation can be achieved by utilization of time-delayed radiation pressure[1] [69] or photothermal forces[2] [70]. The detuning of the drive frequency with respect to the optical cavity influences the effective damping of the mechanical oscillator. This phenomenon was demonstrated for graphene resonators where the graphene sheet was both cooled and mechanically actuated by a laser [71].

A similar nonresonant phenomenon (Fig. 3.1) is achieved if the role of the optical cavity is replaced with an electric LC-circuit [72, 73]. The resonator can then be driven by applying a frequency close to the relatively high LC-frequency. The mechanical oscillator will be nonresonantly driven if the system is in the so called *unresolved sideband regime*, where the line width Γ_{w} of the LC-circuit exceeds the vibrational frequency.

3.1 High-Frequency Actuation by Delayed Back Action

The nonresonant high-frequency actuation mechanisms [69, 72, 73] mentioned above are controlled by the detuning of the drive frequency with respect to a high-frequency resonance in the optical cavity or resonant electric circuit. In Papers I-II, the considered systems were not coupled to such an external resonance. On the contrary, the mechanical vibration was coupled to a purely dissipative electronic subsystem. Nevertheless, nonresonant mechanical actuation could still be achieved by utilizing the electromechanical back action in the system.

[1] Radiation pressure is the momentum transferred when a body is exposed to electromagnetic radiation. This can be used in Fabry–Pérot cavities where one of the reflecting mirrors can move. The force on the mirror is modulated by its position, which can be used to actuate or cool the mechanical vibrations of the movable mirror. In a Fabry–Pérot cavity where the movable mirror is constituted by a graphene sheet, the force caused by radiation pressure is typically very small. This is because of the high transparency of graphene, which gives the Fabry–Pérot cavity a very low finesse, i.e., too much of the radiation leaks out of the cavity. However, photothermal forces can be utilized instead.

[2] Photothermal forces are caused by the heat-induced tension when a material absorbs light. Similar to radiation pressure, photothermal forces can be used to actuate the movable mirror.

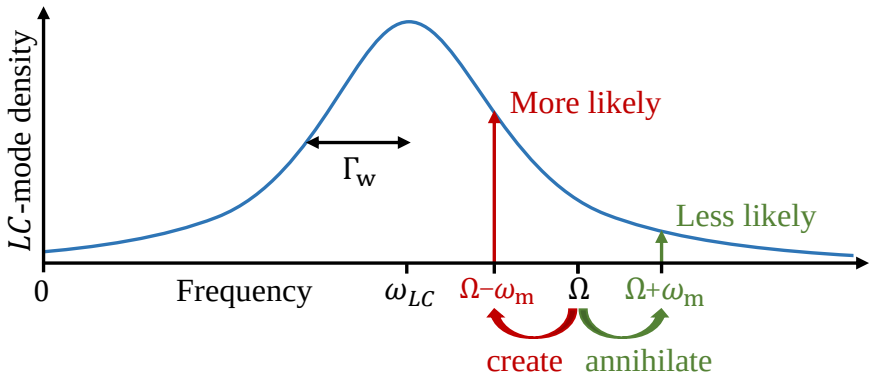

Figure 3.1: Nonresonant actuation by coupling a mechanical resonator to an external LC-circuit. The mechanical vibrations are pumped if the drive frequency Ω is larger than the natural frequency ω_{LC} of the resonant circuit. This can be understood by viewing the interaction as exchange of quanta between harmonic oscillators. First of all, we describe the driving field and mechanical vibration as two ideal harmonic oscillators with energy quanta $\hbar\Omega$ and $\hbar\omega_{\mathrm{m}}$, respectively. On the other hand, the LC-oscillator is coupled to the environment and the LC-resonance is therefore broadened with width Γ_{w}. We can take this into account by viewing the LC-oscillator as a continuum of harmonic oscillators with a Lorentzian mode density (solid line). The LC-oscillator(s) can therefore not only be excited by energy quantum $\hbar\omega_{LC}$, but by any quantum $\hbar\omega$. However, the transition amplitude, for exchange of quanta between the subsystems, depends on the mode density and will therefore decrease with increasing $|\omega - \omega_{LC}|$. Consider the case in which the coupling mechanism requires a mechanical quantum to either be created or annihilated when we drive the LC-oscillator with a quantum $\hbar\Omega$. Hence, when we drive at frequency Ω and create a mechanical quantum, we will have the energy $\hbar(\Omega - \omega_{\mathrm{m}})$ to feed the LC-oscillator with. The situation is analogous if we instead would have annihilated a mechanical quantum. To conserve energy, we have to find an oscillator in the LC-mode density with the corresponding energy $\hbar(\Omega - \omega_{\mathrm{m}})$. For blue-detuned drive ($\Omega > \omega_{\mathrm{LC}}$), the transition in which a mechanical quantum is created is more likely than the transition in which a mechanical quantum is annihilated. This is because the mode density is higher for frequencies closer to ω_{LC}. As a consequence, in net we will pump energy into the mechanical vibration. In the unresolved sideband regime, $\Gamma_{\mathrm{w}} \gg \omega_{\mathrm{m}}$, the pumping of mechanical quanta will be insensitive to the relation between Ω and ω_{m}. The phenomenon is therefore nonresonant in the context of this thesis.

3.1.1 Delayed Back Action in the Circuit Model

In Paper I, we studied nonresonant actuation of a suspended graphene sheet (Fig. 3.2). The actuation mechanism relies on the time-delayed response in the electronic subsystem, as derived in the paper. The aim of the following paragraphs is to complement the mathematical derivation in Paper I with a (hopefully) more intuitive explanation of why actuation can be achieved. To this end, I will here describe a qualitative, simplified version of the circuit model used in the paper.

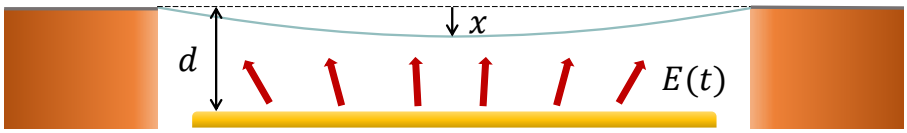

Figure 3.2: Suspended mechanical resonator controlled by the electric field from the gate.

In the model, the charge on the membrane is driven by the alternating gate voltage,

$$\dot{q} = -\frac{q}{RC} + \frac{V_{\rm d}\cos(\Omega t)}{R}\left(1 + \frac{x}{d}\right). \tag{3.1}$$

Here, we have taken into account that the influence of the gate voltage increases slightly if the membrane is mechanically bent towards the gate. The charge can adjust to external variations on the time scale RC which is typically much faster than the mechanical vibrations. When the membrane is charged, the electric field from the gate will exert a force on the mechanical resonator according to

$$\ddot{x} + \gamma\dot{x} + \omega_{\rm m}^2 x = \frac{V_{\rm d}\cos(\Omega t)}{m_{\rm eff} d} q. \tag{3.2}$$

There is an electromechanical back action in the system, since the mechanical deflection alters the charge which in turn acts back onto the mechanical deflection. Furthermore, the interaction is modulated by the drive field.

To see if actuation is possible, we need to investigate the force which acts back on the mechanical resonator. Actuation is achieved if the back action force pumps energy into the vibration and overcomes the mechanical damping. This is the case for a dynamic force component $F_{\rm d}$ proportional to $\dot{x}$, since it will perform the work $\int_0^T {\rm d}t\ \dot{x} F_{\rm d} \neq 0$ during

one period T of the oscillation. We therefore want to understand if such a force component exists. If it does, will it perform work on the vibration or extract work from it, i.e., induce additional damping? As we will see, both pumping and damping can be achieved if we account for the time-delayed response in the electronic subsystem. We can therefore not assume that the electronic subsystem follows the mechanical vibration adiabatically, as we did in section 2.4.

The instantaneous charge, at a given time t, depends on the history of the drive field and the mechanical deflection according to

$$q(t) = \int_{-\infty}^{t} \mathrm{d}t' e^{-(t-t')/RC} \frac{V_\mathrm{d} \cos(\Omega t')}{R} \left(1 + \frac{x(t')}{d}\right). \tag{3.3}$$

The electronic subsystem has a finite "memory" on the time scale RC, due to relaxation of charge. As a consequence, the charge at some time t depends exponentially less on the previous variations of the drive field and the past of the drive field is "forgotten". The accumulated charge $q(t)$ can therefore be viewed as an exponential-weighted average of the history of the drive, i.e., what the charge does remember.

Before trying to understand the actuation mechanism, we will see how the back action force leads to softening of the mechanical resonator. We will then build on this reasoning and the memory analogue. To begin with, we approximate the relatively slow mechanical deflection to be constant during the memory of the electronic subsystem (Fig. 3.3**a**). In this case, the charge on the membrane will simply be the well known [33] time-delayed response of an RC-circuit driven by a periodic field,

$$q = \frac{V_\mathrm{d} C}{\sqrt{1 + (\Omega RC)^2}} \left(1 + \frac{x}{d}\right) \cos(\Omega t - \phi), \tag{3.4}$$

where $\phi = \arctan(\Omega RC) < \pi/2$ is the phase shift of the delayed oscillation relative to the drive. For slow drive frequencies ($\Omega RC \ll 1$), the charge has time to adjust to the slowly varying drive (Fig. 3.3**a**). In the language of the analogue, the memory of the charge is too short for it to remember any significant changes of the drive. However, for fast drive frequencies ($\Omega RC \gg 1$), the accumulated charge will not have time to fully load before the drive field is reversed. This both suppresses and *delays* the response. In other words, for fast drive frequencies, the accumulated charge starts to remember that the drive field has been oscillating and the weighted average, i.e., the charge, will be reduced. Hence, the amplitude of the charge oscillation will be suppressed and the RC-circuit will operate as a low-pass filter.

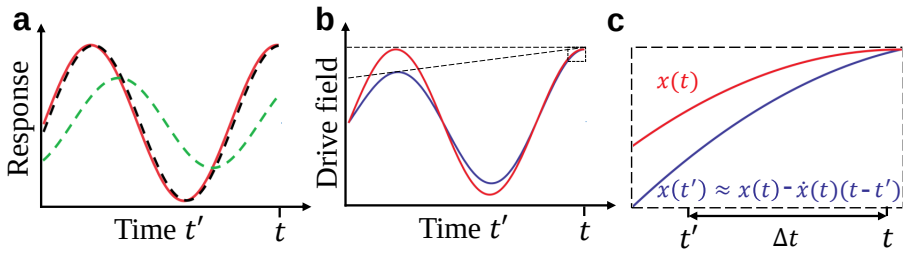

Figure 3.3: **a** Charge response (dashed) for a drive field with stable amplitude (solid). If $\Omega RC = 0.1$ (black), the charge has time to adjust. However, if $\Omega RC = \sqrt{2}$ (green), the drive is reversed before the charge has time to fully load. **b** The drive field for a stationary membrane (red) and the drive field for a membrane which is slowly approaching the gate (blue), i.e., with increasing amplitude. **c** Zoom in of the drive fields. Due to the exponentially decaying memory of the charge system, we can to first approximation treat the membrane position as a linear function increasing with slope $\dot{x}(t)$.

For any drive frequency, the mechanical resonator will experience softening due to the back action force F. The force $F \propto qE(t)$ is proportional to the charge on the membrane acted upon by the oscillating electric field $E(t) \approx V_\mathrm{d} \cos(\Omega t)/d$ which gives

$$F \propto \left(1 + \frac{x}{d}\right) \cos(\Omega t + \phi) \cos(\Omega t) = \left(1 + \frac{x}{d}\right) \frac{[\cos(\phi) + \cos(2\Omega t + \phi)]}{2}. \tag{3.5}$$

The mechanical resonator does not have time to adjust to the rapid force components oscillating on the time scale $1/2\Omega$ and we neglect this component by averaging over fast oscillations [74]. However, the slow component will influence the resonator. More importantly, the amplitude of the charge oscillation (and therefore the strength of the force) depends on the deflection of the mechanical resonator. As a result, the mechanical vibrations will be softened by the back action force, since the phase shift in an RC-circuit is restricted by $0 \leq \phi < \pi/2$. This is similar to the electrostatic softening described in section 2.4.

This softening force term does neither pump nor damp the resonator. For such a phenomenon, we have to take into account that the resonator is in fact moving. Let us first consider the case when the drive frequency is slower than the relaxation rate so that the charge *almost* has time to adjust; its memory is short. We also assume that the mechanical

resonator slowly moves towards[3] the gate. The simple expression in Eq. (3.4) will then overestimate the accumulated charge. This is because it does not take into account that the amplitude of the drive field was weaker further back in time (Fig. 3.3**b**). We can qualitatively compensate for this overestimation by reducing the charge by a small component which will be proportional to the velocity, $\dot{x}$, of the resonator. The faster the resonator moves, the bigger the overestimation. This compensation is reasonable since the membrane moves slowly. Its speed is approximately constant during the memory of the electronic subsystem[4]. When we subtract the compensatory charge component it results in a slow frequency back action force proportional to $-\dot{x}$. In conclusion, the resonator experiences the electronic subsystem as a "viscous" medium which extracts energy from the oscillating resonator. As long as the charge (almost) has time to adjust to the drive field, it will induce additional damping of the mechanical vibration.

On the other hand, if the drive frequency is slightly faster than the relaxation rate, we will pump the mechanical vibration. To understand this case is more demanding since the delay in the charge response is significant. The phase shift of the main charge component (Eq. (3.4)) is restricted by $\pi/2$, i.e., it will never be out of phase with the drive field and thereby stiffen the resonator. However, the phase shift of the compensatory term can exceed $\pi/2$. This is because the deviation between a constant amplitude drive and the drive amplitude for a moving membrane gets successively worse (Fig. 3.3). We can view this as a memory function $\exp[-(t-t')/RC](t-t')/RC$, biased to remember what happened around $t' = RC$ in the past. The phase shift of this component will therefore exceed $\pi/2$ when it is biased to remember that the drive field had opposite direction. This happens for drive frequencies $\Omega \approx 1/RC$. As a result, this charge component gives a back action force proportional to $+\dot{x}$, which pumps energy into the mechanical vibration. As a last case, if the drive frequency is very high, the charge does not have time to respond at all and the drive field has no effect on the system (Fig. 3.4).

In Paper I, we studied the nonresonant high-frequency actuation mechanism in a more extensive model including a parasitic capacitance which reduces the effect of the actuation mechanism. We also discussed

[3]The situation is analogous when the resonator moves in the other direction and will result in the same conclusions.

[4]This correspons to approximating $x(t') \approx x(t) - (t-t')\dot{x}(t)$ in Eq. (3.3).

the possibility of using the nonresonant actuation mechanism to study nonlinear dissipation in NEMS, since the nonlinear dissipation typically saturates the nonresonant action. This is in contrast to the commonly occurring Duffing nonlinearity[5]. Such a nonlinearity shifts the effective frequency of the vibration and can therefore saturate actuation due to a resonant mechanism by pulling the mechanical frequency out of resonance. However, frequency pulling would typically not have any qualitative effect on a nonresonant actuation mechanism.

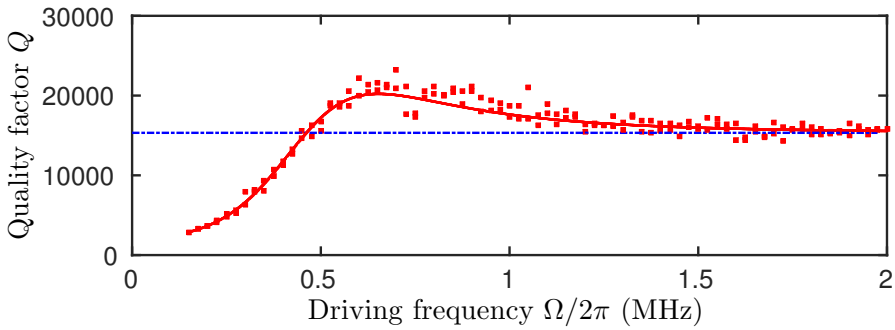

Figure 3.4: Experimental observations, by Barois *et al.* [75], of the effective quality factor Q due to the time-delayed back action mechanism suggested in Paper I. The experimental measurements (dots) are in good agreement with the theory (solid) of Paper I. The mechanism increases the damping of the mechanical vibration when the drive frequency is slow compared to the charge relaxation rate $1/RC$. Hence, in this regime the effective quality factor is lower than the intrinsic quality factor (dash-dotted). However, if the drive frequency is increased above the relaxation rate, the mechanism results in pumping of the mechanical motion and the effective quality factor exceeds the intrinsic one. For drive frequencies much faster than the relaxation rate, the charge oscillations are heavily suppressed and the quality factor is unaffected. Barois *et al.* also showed that mechanical vibration can be actuated if the induced pumping overcomes the intrinsic damping. The figure was provided by Dr. Anthony Ayari.

Our paper stimulated Barois *et al.* [75] to study the nonresonant high-frequency actuation mechanism experimentally (Fig. 3.4). They found the mechanism appealing since it reduces the complexity of the system — the resonator does not need to be coupled to an external resonance such as a resonant electric circuit [72, 73]. They also argued that the nonresonant mechanism can be utilized to simultaneously ac-

[5]The Duffing nonlinearity is further discussed in chapter 5.

tuate several different resonator structures with the same drive field. This is because the frequency range for actuation is relatively large in comparison to resonant actuation of high Q resonators. However, a drawback with the mechanism is that the dissipation in the electronic subsystem heats the structure considerably [75]. The reason for this is that the majority of the energy absorbed from the drive field will be dissipated in the electronic subsystem and not be converted to mechanical energy.

3.1.2 Playing with the Effective Density of States of a Quantum Dot

Will the nature of the nonresonant actuation mechanism change if the quantization of charge is pronounced so that a continuum model of the charge dynamics is no longer feasible? This was studied in Paper II , where we investigated a movable single-level quantum dot (Fig. 3.5). The quantum dot is in tunneling contact with an electronic reservoir described by the model from section 2.1.3. The dot is coupled to the mechanical vibrations of a CNT since the energy level[6] ϵ_{Dot} of the stationary dot is shifted when the CNT deflects in the electric field $E\cos(\Omega t)$. The shifts amounts to $eE\cos(\Omega t)\hat{x}$, where $\hat{x}$ is the position operator. Note that the electrons are only coupled to the mechanical vibration if a field is applied. Now, what happens if we try to mimic the classical case considered in the previous chapter and drive the system nonresonantly, well above the mechanical resonance frequency, at the time scale of the electronic dynamics?

To begin with, what is the time scale of the electron dynamics? To address this question, let us begin by disregarding the weak electromechanical coupling and focus on the interaction of the quantum dot and the electronic reservoir. Due to the tunneling interaction, the dot state is no longer an eigenstate of the electronic Hamiltonian. The dot state will hybridize with the reservoir states and form new eigenstates corresponding to the creation operators $\hat{\psi}_k^\dagger$. As a consequence, if we put an electron in the dot state[7] it will start to evolve according to quantum mechanics (Eq. (2.5)) and "escape" out to the reservoir. The tunneling rate of escape $\Gamma = \pi\mathcal{T}^2\nu_{\mathrm{DoS}}/\hbar$ depends on the tunneling strength $\mathcal{T}$ and the density of states (DoS) ν_{DoS} in the reservoir. We approximate

[6] Counted from the chemical potential in the reservoir.

[7] I.e., a superposition of hybridized states.

the DoS to be constant since it does not vary significantly on the energy scale of interest. Analogously to the classical case in the previous section, the charge on the vibrating structure can be filled and emptied on the time scale $1/\Gamma$.

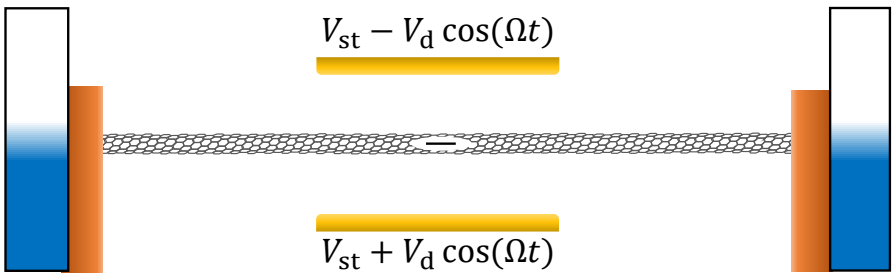

Figure 3.5: A suspended CNT quantum dot in tunneling contact with an electron reservoir constituted by the two leads. In many applications the leads to the left and right have to be treated as two distinct reservoirs typically held at different voltages. However, we are only interested in tunneling to and from the QD and not in charge transport *through* the structure. Hence, we treat the two leads as a single reservoir. The system is tuned into a single-level quantum dot by the static voltage V_{st} (degeneracy for spin can be lifted by a magnetic field) and then driven by the harmonic modulation $V_{\mathrm{d}} \cos(\Omega t)$. Two gates are used in order to reduce the Joule heating in the system.

Now, let us take a look at the type of processes which are induced by the driving electromechanical coupling term $\hat{H}_{\mathrm{i}} = eE \cos(\Omega t)\hat{x}\hat{d}^\dagger\hat{d}$. It describes four different types of processes illustrated in Fig. 3.6. To see this, let us write the interaction term in the basis of the hybridized electronic eigenstates,

$$\hat{H}_{\mathrm{i}} = \frac{eEa_0}{2} \sum_{k,k'} \chi_k \chi_{k'}^* \left(e^{i\Omega t} + e^{-i\Omega t}\right) (\hat{c}^\dagger + \hat{c}) \hat{\psi}_k^\dagger \hat{\psi}_{k'} \tag{3.6}$$

with $\chi_k = \mathcal{T} \exp(-i \mathrm{arccot}[(\epsilon_k - \epsilon_{\mathrm{Dot}})/\hbar\Gamma])/\sqrt{(\epsilon_{k'} - \epsilon_{\mathrm{Dot}})^2 + (\hbar\Gamma)^2}$ and zero-point amplitude of oscillation $a_0 = \sqrt{\hbar/2m\omega_{\mathrm{m}}}$. Reading the interaction term Eq. (3.6) from the right, each process will annihilate an electron ($\hat{\psi}_{k'}$) in a state with energy $\epsilon_{k'}$ and create an electron ($\hat{\psi}_k^\dagger$) in a state with energy ϵ_k. Each process will also either absorb ($\hat{c}$) or emit ($\hat{c}^\dagger$) a quantum to the mechanical vibration and either absorb or emit a quantum[8] to the drive field with energy $\hbar\Omega$ (Fig. 3.6). However,

[8]Note that we have described the drive field as a classical field which is unaffected by the absorption of a few photons.

the processes where quanta are emitted back to the drive field will be strongly suppressed at low temperature of the reservoir $T \ll \hbar\Omega/k_{\mathrm{B}}$, since there are (almost) no empty states below the chemical potential to put electrons in. The main contribution will be to absorb a quantum from the drive field and use the energy to lift an electron from below to above the Fermi surface and simultaneously emit or absorb a mechanical quantum.

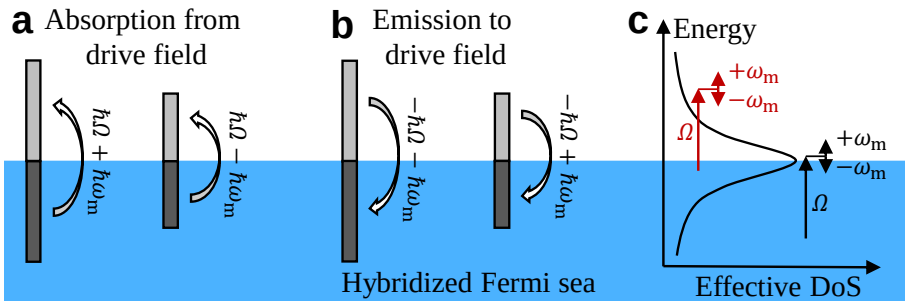

Figure 3.6: The four processes described by the interaction Hamiltonian Eq. (3.6) at temperature $T = 0$. The two processes in **a** describe absorption of a drive field quantum which lifts an electron from the dark gray region to the light gray region. When doing so, a mechanical quantum is either annihilated or created. Hence, the two processes will lift electrons with a difference in energy of $2\hbar\omega_{\mathrm{m}}$. The processes which absorb a mechanical quantum has access to more energy and can therefore reach deeper into the Fermi sea. The two processes in **b** are the Hermitian conjugated processes. These will be suppressed at low temperatures due to the lack of electrons above the chemical potential which otherwise would have been pulled down below the surface. The effective density of states, depicted in **c**, is localized around the Fermi surface if $\epsilon_{\mathrm{Dot}} = 0$. For a typical case (red arrows), the process which creates one mechanical quantum ($-\omega_{\mathrm{m}}$) is more likely than annihilation of one quantum ($+\omega_{\mathrm{m}}$), due to the larger effective density of states close to the Fermi surface. However, this effect has to compete with the fact that processes (black arrows) annihilating a mechanical quantum (and thereby collecting more energy to the electronic subsystem) can reach deeper into the Fermi sea. In conclusion, the allowed processes which create a mechanical quantum are relatively more likely but fewer than the processes annihilating a mechanical quantum. Both damping and pumping can be achieved depending on the relation between the drive frequency Ω and the "width" Γ of the effective density of states.

To actuate mechanical vibrations, the rate at which mechanical quanta is created (Γ^{+}) has to overcome the rate at which mechanical quanta is absorbed (Γ^{-}). These rates coincide with the rates given by Fermi's

golden rule, which was not derived in Paper II . However, a derivation can be found in Appendix B. More importantly, from the derivation, we can identify the effective density of states $\nu_{\mathrm{DoS}}^{\mathrm{eff}} \propto 1/((\epsilon-\epsilon_{\mathrm{Dot}})^2+(\hbar\Gamma)^2)$, see Fig. 3.6**c**. The creation and absorption rates can be interpreted in terms of the induced processes weighted with the effective density of states. In Paper II it was concluded that the mechanical vibrations are in net pumped when the drive frequency slightly exceeds the relaxation rate of the electronic system (Fig. 3.7**a**), similarly to the classical case. However, in contrast to the simple circuit model, the quantum model naturally accounts for temperature (Fig. 3.7**b**). Furthermore, the quantum model also shows that this nonresonant mechanism does not lead to cooling even though $\Gamma^- > \Gamma^+$. This is a clear example that *damping* ($\Gamma^- > \Gamma^+$) is not the same as *cooling*[9]. The mechanical vibrations become unstable when the pumping overcomes the intrinsic mechanical damping. The vibrations will then be saturated by "nonlinear" i.e., multi-phonon processes, as shown in the complementary calculations to Paper II in Appendix C.

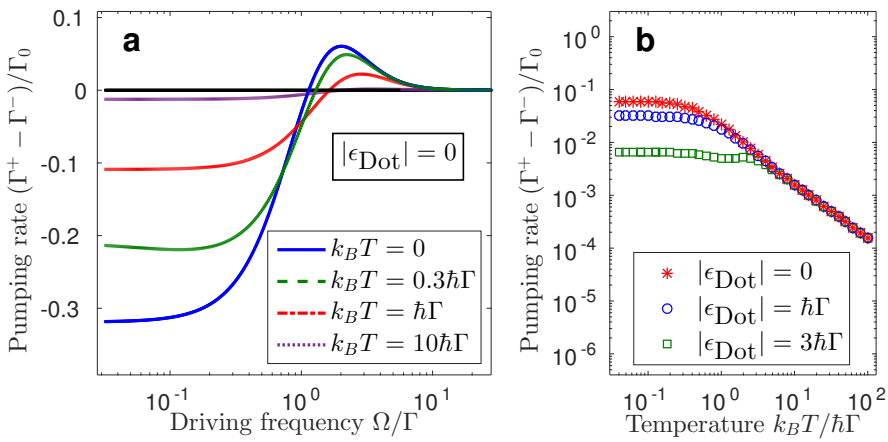

Figure 3.7: Pumping rate normalized with $\Gamma_0 = \omega_{\mathrm{m}}(eEa_0/\hbar\Gamma)^2$. The mechanical oscillator is damped for drive frequencies smaller than $\sim\Gamma$. For drive frequencies slightly above Γ, the induced processes effectively pump the mechanical vibration. The influence of the induced processes diminishes with temperature when $T > \hbar\Gamma/k_{\mathrm{B}}$. **b** The effect is also diminished if the dot level is detuned away from the chemical potential.

[9]Remark: An inconsistent comparison is made in the last paragraph of section 3 in Paper II , which leads to the incorrect conclusion that cooling can be achieved.

To play with the effective density of states is a cornerstone in optomechanics. However, optomechanics usually plays with the effective DoS of a photonic subsystem coupled to the mechanical mode whereas electromechanics utilizes properties of the electronic density of states. Paper II shows an example of how a resonance in the effective density of states is not a requirement for actuation. The lack of a resonance makes the response more subtle and not as straightforward as in the resonant case (cf. Fig. 3.1). Furthermore, the nonresonant actuation mechanism studied here can only convert a small portion of the energy absorbed from the drive field into mechanical energy. A considerable amount of the energy needs to be dissipated in the electronic subsystem. However, the possibility of achieving a mechanical instability and thereby actuating a mechanical mode is not excluded, even though the mode is coupled to a strongly dissipative electronic subsystem.

3.1.3 Selective Mode Actuation

In Paper III, we studied how the nonresonant back action mechanism can be utilized to actuate vibrations of an isolated suspended graphene resonator (Fig. 3.8**a**). Since the graphene sheet is not even connected to an electronic reservoir, the electron dynamics is determined by the *internal* dynamics within the sheet. Hence, the equivalent circuit model is too crude to describe the dynamics. On the other hand, the graphene sheet is so large that individual energy levels cannot be resolved and a quantum model would therefore be superfluous. A good level of description is instead provided by the semiclassical model (section 2.1.2), which is able to describe the response in the inhomogeneous charge distribution when driven by an external electric field.

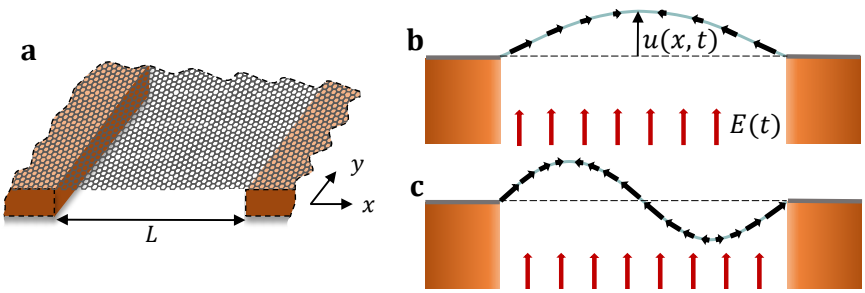

Figure 3.8: **a** An isolated graphene resonator, i.e., not in electronic contact with any reservoir or conducting elements. **b** When a vertical electric field (red) is applied, a field component (black) will be induced along the graphene sheet when it is deflected from its flat configuration. **c** The induced field profile mimics the spatial profile of the vibrational mode.

The isolated graphene sheet exhibits a similar back action force as discussed above. The external field has an inhomogeneous component along the graphene sheet if it is deflected from its flat position (Fig. 3.8**b-c**). As a consequence, the field component will distort the charge distribution and charge the suspended resonator. The external field will then pull in the excess charge and exert a vertical back action force on the mechanical deflection. Separation of charge into an inhomogeneous profile is a consequence of a spatial gradient in the electric field. The external field component $E_{\rm ext}(x,t)$ along the membrane is indeed inhomogeneous for a non-flat sheet since the field depends on the deflection $u(x,t)$ of the membrane $E_{\rm ext}(x,t) = E(t)\partial u(x,t)/\partial x$ where $E(t) = E_{\rm d}\cos(\Omega t)$ is the homogeneous drive field.

A dynamical equation for the charge can be obtained by combining the continuity equation (Eq. (2.4)) with the equation for the conductivity (Eq. (2.3)) which gives[10]

$$\frac{\partial^2}{\partial t^2}\varrho(x,t)+\nu_{\rm R}\frac{\partial}{\partial t}\varrho(x,t)+\frac{1}{2\pi\epsilon_0\mathcal{L}}\frac{\partial}{\partial x}\mathcal{P}\int_{-\infty}^{\infty}\frac{\varrho(x',t)}{x-x'}{\rm d}x' = -\frac{E(t)}{\mathcal{L}}\frac{\partial^2}{\partial x^2}u(x,t). \tag{3.7}$$

where $\mathcal{L} = \pi\hbar^2/e^2E_{\rm F}$. Equation (3.7) resembles a driven and damped oscillator where the internal electric field due to separation of charge

[10]This equation can similarly to the circuit model be analyzed by the Green's function technique which gives

$$G(q,\omega) = -\frac{1}{\omega^2 - \frac{|q|}{2\epsilon_0\mathcal{L}} - i\omega\nu_{\rm R}}.$$

The back action force term on mechanical mode n with $u(x,t) = u_n(t)f_n(x/l)$ can be approximated as (see Paper III for details)

$$\mathcal{F}_n(t) = \frac{E_0^2\epsilon_0\pi}{\rho_{\rm m}l}\int_{-\infty}^{t}{\rm d}t'\; G_n(t-t')\cos\Big(\Omega(t-t')\Big)\frac{u_n(t')}{l}.$$

The back action force depends on the history of the mechanical amplitude, drive field and charge response

$$G_n(t-t') = \omega_{\rm p}\int_{-\infty}^{\infty}{\rm d}Q\;\frac{e^{-\nu_{\rm R}t/2}\sin\Big((t-t')\sqrt{4\omega_p^2|Q|-\nu_{\rm R}^2}/2\Big)}{\sqrt{4\omega_p^2|Q|-\nu_{\rm R}^2}/\omega_{\rm p}}Q^2|\langle e^{i\pi\xi Q},f_n(\xi)\rangle|^2$$

with $\omega_{\rm p} = e\sqrt{E_{\rm F}/(2\epsilon_0 l)}/\hbar$ and spatial overlap of the charge wave and the mechanical mode profile $f_n(\xi)$ which is normalized $\langle f_n(\xi),f_n(\xi)\rangle = 1$,

$$\langle e^{i\pi Q\xi},f_n(\xi)\rangle = \int_{-1/2}^{1/2}{\rm d}\xi\; e^{i\pi Q\xi}f_n(\xi).$$

acts as a restoring force. The drive term in the right hand side is proportional to the second spatial derivative of the membrane deflection, i.e., the curvature of the membrane. The curvature for the vibrational modes in a suspended graphene sheet is especially large close to the clamping, since graphene has an exceptionally low bending rigidity[11]. A crude approximation of the drive term is therefore to view it as two point sources at the clamping points.

A qualitative picture of the actuation mechanism can be described as follows: The two point sources generate charge waves from each side of the trench. The waves propagate out in the suspended part and interfere. For specific drive frequencies, the wavelength of the charge waves matches the width L of the trench and creates a standing wave. The profile of the standing wave has a considerable overlap with a specific mechanical mode shape. As a consequence, the drive field couples strongly to the corresponding mechanical mode with the same wavelength. In this respect, the studied phenomenon is a geometrical resonance in space. However, the phenomenon is nonresonant in the time domain since there is no explicit relation between the drive and vibrational frequency.

The charge wave will be time-delayed and able to both damp and pump the mechanical motion (Fig. 3.9), in analogy with the results discussed in the previous two sections. Interestingly, the mechanical modes can be pumped selectively if the charge waves are underdamped. To selectively pump a mode, the drive frequency has to be tuned to achieve geometrical resonance for each mode respectively. One drawback with this actuation mechanism is that it requires comparably strong drive fields. In Paper III, we estimated the required drive field to be roughly 100 times larger than the strong field of ~ 1 V/μm used in the experiment in Paper VII. On the other hand, the pumping force increases quadratically with mode number n. This is in contrast to standard resonant actuation mechanisms where the pumping strength typically decreases with mode number for a homogeneous drive field. The reason for the decreased pumping strength is the decreased spatial overlap between the mechanical mode and the drive field (Fig. 2.9). The nonresonant pumping mechanism described by the semiclassical Eq. (3.7) does not suffer from this effect but is at the same time not applicable to high mode numbers, since it relies on local equilibrium of the charge carriers. The drive frequency is therefore limited by the electron-

[11]The full distributed model of the deflection $u(x,t)$ is found in Paper III, Eq. 1.

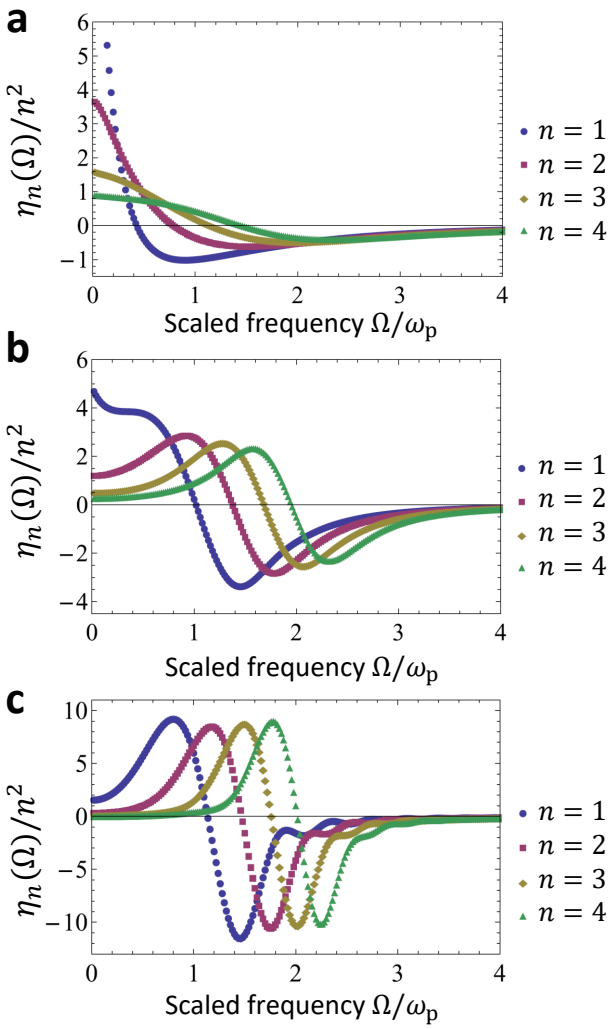

Figure 3.9: Scaled induced mechanical damping for different mechanical mode numbers n and damping ratios ν_R/ω_p of the charge waves with characteristic plasma frequency $\omega_p = e\sqrt{E_F/(2\epsilon_0 l)}/\hbar$. **a** For overdamped charge oscillations (here $\nu_R/\omega_p = 3$) the induced damping resembles the one observed in the capacitive (Fig. 3.4) and quantum (Fig. 3.7) models. **b** The damping ratio has been decreased to $\nu_R/\omega_p = 1$. **c** Selective actuation of modes can probably be detected for underdamped charge waves (here $\nu_R/\omega_p = 1/3$) since the pumping peaks are separated. The separation is limited by the geometrical resonance.

electron scattering time which is typically some hundreds of femtoseconds [76, 77, 57]. Furthermore, actuation of anti-symmetric modes typically requires multi-gate structures. However, the actuation mechanism discussed here can also drive anti-symmetric mechanical modes, even though the drive field is homogeneous.

3.2 Delayed Back action Based on Interaction of Electrons

In Paper IV, we no longer utilize an external alternating field to actuate mechanical vibrations. Instead, we take advantage of a temperature difference between two reservoirs and convert heat to mechanical energy. The system therefore resembles a nanoelectromechanical heat engine.

Similar actuation mechanisms which are based on either a static voltage bias [65, 66, 78, 79, 80] or a temperature drop [81] have been studied. These mechanisms are based on a back action force where the mechanical vibration generates oscillations of the average charge (spin) on the suspended resonator. These charge oscillations modulate the back action force, which pumps the mechanical vibration. The mechanisms studied in [65, 66, 78, 79, 80, 81] require transfer of electrons from one reservoir to another. If the flow of electrons is blocked, the mechanisms no longer function. In the system studied in Paper IV, such electron flow is blocked. Furthermore, the mechanical vibration does not even generate time variations in the average charge on the suspended structure. Nevertheless, actuation is still possible.

A prototype system which exhibits the actuation mechanism is illustrated in Fig. 3.10. A CNT suspended over a trench constitutes a four state quantum dot. It can be either unoccupied, populated by one electron with either spin, or doubly populated by two electrons with opposite spin. Electrons with spin-$\downarrow$ can tunnel to and from the leads which constitute a single spin-polarized[12] reservoir. Similarly, spin-$\uparrow$ electrons can tunnel to and from the tip which is spin-polarized for opposite spins. As a consequence, an electron from the leads can tunnel to the CNT but not continue to the tip since the tip does not contain any spin-$\downarrow$ states. Even though there is no tunneling *through* the system, the reservoirs still interact due to the electron-electron interaction

[12]Spin polarized so called *half-metals* contain only spin-σ states ($\sigma = \uparrow, \downarrow$) close to the Fermi surface [82].

in the quantum dot. Furthermore, the external forces on the CNT are assumed to be dominated by the capacitive force towards the gate. As we will see, the electron-electron interaction allows for a heat flow between the two reservoirs which are kept at different temperatures. More importantly, the interaction also mediates a delayed back action force which can pump the mechanical vibration.

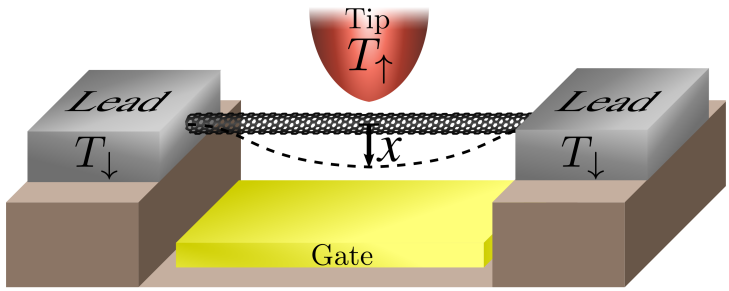

Figure 3.10: The CNT is suspended over a gate and acts as a four-state quantum dot. Electrons can tunnel to and from the dot, but not to a reservoir with opposite spin polarization. The reservoirs have different temperatures which constitute the energy source for the pumping mechanism. Both the capacitive force towards the gate and the tunneling rate to the tip depend on the mechanical deflection.

To understand how heat is transferred between the reservoirs, let us consider the positioning of the electronic states as depicted in Fig. 3.11. If we assume the tip to have a high temperature while the leads are cold, the electron dynamics can be reduced to a four-step cycle described in Fig. 3.12. During one cycle a spin-$\uparrow$ electron leaves the tip with energy $E_1^\uparrow + U$, where U is the electron-electron interaction energy. However, when it comes back, it only brings the energy $E_1^\uparrow$. Conversely, a spin-$\downarrow$ electron with energy $E_1^\downarrow$ leaves the leads and comes back with energy $E_1^\downarrow + U$. Hence, during one cycle, the energy U has been transferred from the hot to the cold reservoir due to the electron-electron interaction. By this means, we have access to a thermodynamic energy source which potentially could pump the mechanical vibration.

To understand the nature of the back action pumping mechanism, we will characterize the electron dynamics by the probabilities[13] P_0, $P_\uparrow$, $P_\downarrow$

[13]In the supplemental material of Paper IV, we derive the rate equations for the probabilities from the Liouville-von Neumann equation by following Refs. [83, 84]. The rate equations are valid for high temperatures $k_\mathrm{B}T_{\uparrow,\downarrow} \gg \hbar\omega_\mathrm{m}, \hbar\Gamma_\uparrow, \hbar\Gamma_\downarrow$.

and P_2 to be in either of the four states. The capacitive force on the mechanical resonator can then be described by

$$F = -\frac{\partial}{\partial x}\frac{e^2}{C(x)}\left(P_\uparrow + P_\downarrow + 4P_2\right) = -\frac{\partial}{\partial x}\frac{e^2}{C(x)}\left(n_\uparrow + n_\downarrow + 2P_2\right). \quad (3.8)$$

This force is the average contribution of the forces in the different states[14]. An alternative form of the force is given by introducing the probabilities $n_\sigma = P_\sigma + P_2$ to have an electron with spin $\sigma = \uparrow,\downarrow$ on the dot, regardless of whether an electron of the opposite spin is present or not. As will be argued later, the probabilities n_σ are constant in time and will therefore not contribute to a dynamic back action force.

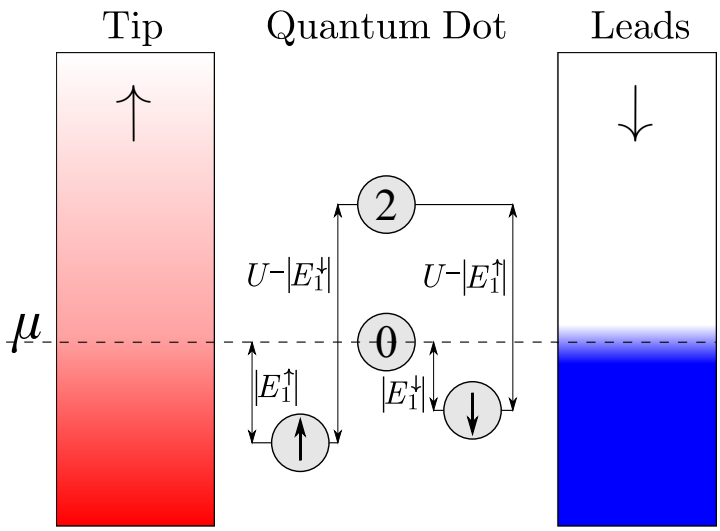

Figure 3.11: Energy diagram of the four dot states. The two singly-occupied states are below the chemical potential μ of the reservoirs. Without electron-electron interaction, we could use the independent-electron model and the energy for the doubly-populated state would be $|E_1^\uparrow| + |E_1^\downarrow|$ below μ. However, due to electron-electron interaction, the doubly-populated state contains the additional interaction energy U, which brings the doubly-populated state above the chemical potential. The occupation of electrons in the reservoirs are indicated by the gradual filling, which reflects the reservoir temperatures. This figure was provided by Dr. A. Vikström [85].

[14]The force in the doubly-populated state is two (electrons) squared i.e., four times stronger than the singly-populated states.

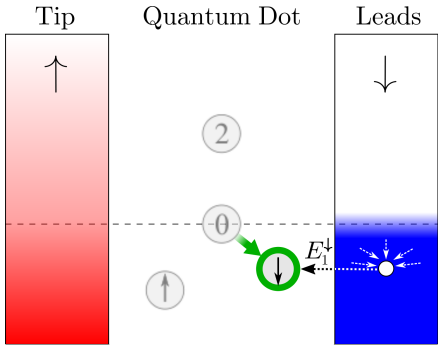

A cycle starts with a spin-↓ electron tunneling from the leads to the empty dot, bringing the dot to the singly-occupied spin-↓ state. After the tunneling event, the empty state left in the leads relaxes quickly due to internal processes.

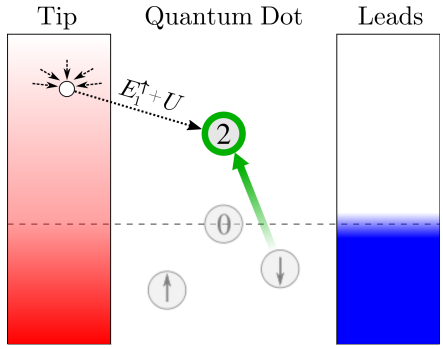

The spin-↓ electron is now stuck on the dot since there are almost no empty states in the lead with energy $E_1^{\downarrow}$. On the other hand, a high-energy spin-↑ electron can overcome the additional interaction energy U and tunnel to the dot (bringing it to the doubly-occupied state). Then the empty state in the tip relaxes.

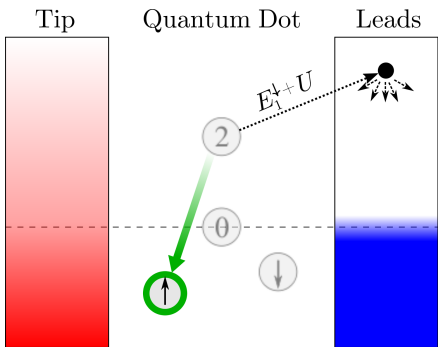

The electron tunneling has at this stage brought the energy $E_1^{\uparrow} + E_1^{\downarrow} + U$ to the dot. Since the doubly-occupied state has relatively high energy, the spin-↓ electron can now tunnel back to the leads. It will leave the dot in the spin-↑ state with energy $E_1^{\uparrow}$ and return to its lead with energy $E_1^{\downarrow} + U$.

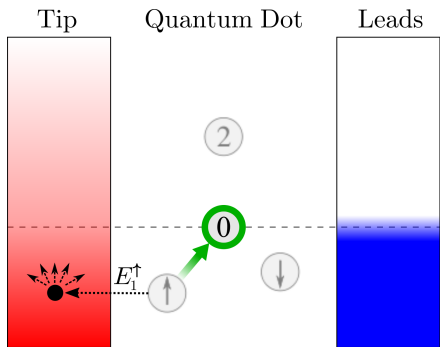

Finally, the spin-↑ electron may tunnel back to the hot tip since there are a considerable amount of empty states it can tunnel to. The dot is then empty and a new cycle can begin. This cycle only describes the average dynamics (the probabalistic nature of the equations include reverse processes).

Figure 3.12: The heat transfer cycle caused by the electron-electron interaction. Tunneling processes are indicated by dashed arrows. Each tunneling process brings the dot from one of its states to another, indicated by the solid arrows. Note that some tunneling arrows (dashed) are not horizontal, which reminds us that the energy diagram depicts the four energy states and not independent energy levels. These figures were provided by Dr. A. Vikström [85].

The back action mechanism is described in Fig. 3.13. A crucial component in the actuation mechanism is that the electron-electron energy depends on the mechanical deflection so that it generates a force. Both the magnitude and the sign of the back action force can be controlled by the temperature difference of the reservoirs. In particular, softening and damping of the vibration can therefore also be achieved, if the temperatures of the reservoirs are switched.

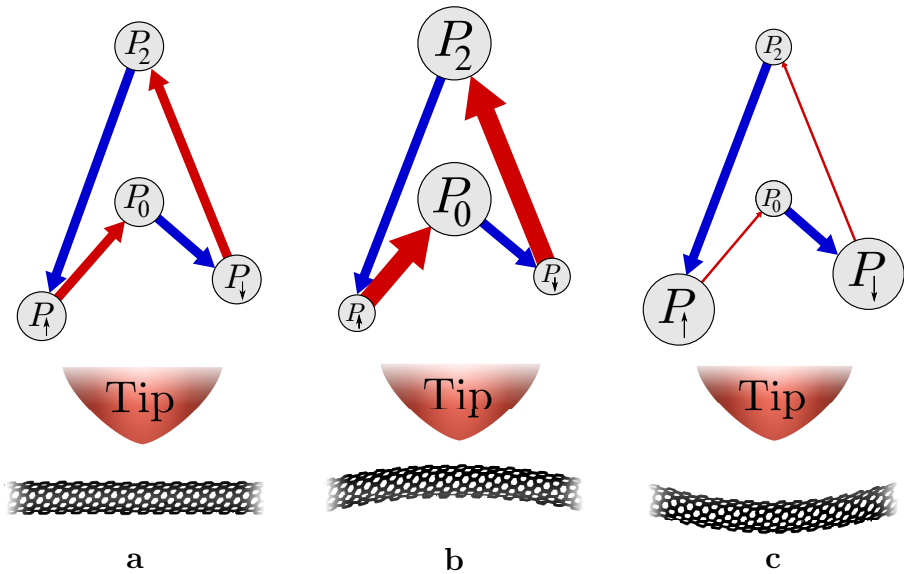

Figure 3.13: Explanation of the back action mechanism which leads to actuation of mechanical vibrations. **a** If the CNT is static, the flow of probability between the four states will equilibrate to a stationary counterclockwise flow (see Fig. 3.12). Hence, the flow of probability in and out from each state are equal. **b** If the CNT deflects towards the tip, the tunneling rate for spin-↑ electrons increases which enhances the corresponding probability flows (indicated by thicker arrows for these flows). The unchanged tunneling rate for spin-↓ electrons then becomes a bottleneck in the cycle. As a consequence, occupation probability will accumulate in the P_2 and P_0 states, whilst the $P_\uparrow$ and $P_\downarrow$ states will be drained with an equal amount. Hence, the average numbers $n_\sigma = P_\sigma + P_2$ of spin-σ electrons are unchanged. **c** Conversely, if the CNT deflects away from the tip, the tunneling of spin-↑ electrons will be suppressed and become a bottleneck, again without changing n_σ. Since n_σ is constant, the two first force terms in Eq. (3.8) cannot generate dynamic back action. However, dynamic back action is still possible since the capacitive force depends on the *square* of the charge, $e^2[n_\uparrow + n_\downarrow + 2P_2(t)]$, which varies in time even though the average charge, $-e[n_\uparrow + n_\downarrow]$, does not. Hence, we can focus our attention on what happens with the probability of being in the doubly-occupied state P_2. The back action force can now be understood as follows: The CNT deflects towards the tip which increases the occupation of the doubly-occupied state due to the bottleneck effect. As a consequence, the capacitive force *down* towards the gate increases and stiffens the vibrations. Furthermore, the back action force will be delayed and therefore not only stiffen but also pump the mechanical vibration. This figure was provided by Dr. A. Vikström [85].

Chapter 4

Exciting Supercurrents

> The chimpanzee Washoe learned sign language, then she taught her son.
>
> Speaking of the impact of ideas.

In this chapter, I will describe one example of how actuated mechanical motion can be useful. The example corresponds to Paper V, where we studied a nanomechanical resonator coupled to coherent transfer of Cooper pairs through a Josephson junction. A Josephson junction is a weak link between two superconducting leads which allows Cooper pairs to tunnel between them. In an ordinary Josephson junction, a ground state supercurrent flows through the junction if the leads have different superconducting phases. If the phases are equal, no supercurrent flows. However, in Paper V we showed that by inserting and parametrically actuating a movable Cooper-pair box (CPB), see Fig. 4.1, a supercurrent can be generated even though the superconducting phase difference is zero.

To generate such supercurrents has attracted considerable attention during the last decade. The literature contains several proposals of how to modify Josephson junctions in order to break the underlying symmetries which prevent the supercurrent to flow at zero phase difference. Modified junctions which support a ground-state supercurrent despite zero phase difference are called φ_0-junctions. Theoretical proposals of φ_0-junctions include ferromagnetic structures [90, 91], quantum point

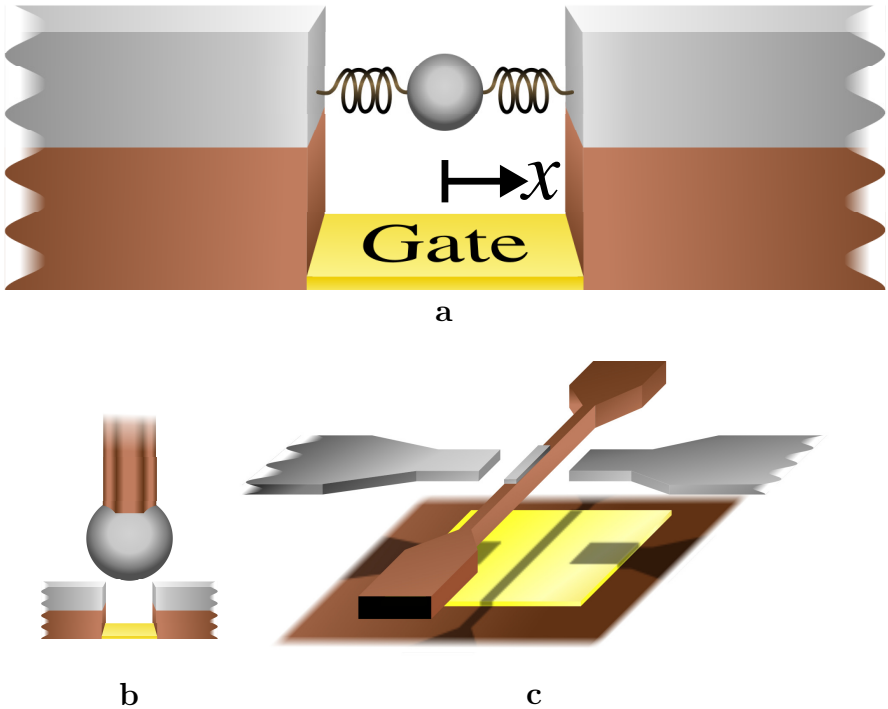

Figure 4.1: **a** A sketch illustrating the theoretical model. A Cooper-pair box (gray sphere) which is attached to anharmonic symmetric (virtual) springs can oscillate in the gap between two superconducting leads (gray blocks). Cooper pairs can tunnel from one lead to the other via the Cooper-pair box. An alternating gate voltage modulates the charge on the CPB, leading to a parametric excitation of horizontal mechanical vibrations. **b** and **c** show two suggestions for realization of the system. In **b**, the CPB is constituted by a superconducting grain (gray sphere) on a bendable nanowire. In **c**, the CPB (gray rectangle) is instead attached to a suspended nanobeam which can oscillate laterally. (Brown components are made of insulating material.) To my knowledge, these structures have not yet been experimentally realized. However, related systems have been constructed, such as a suspended CPB [20], a superconducting mechanical resonator embedded in a SQUID [86], as well as mechanical resonators coupled to superconducting qubits [87, 2, 88, 89].

contacts [92], topological insulators [93, 94], quantum dots [95, 96, 97] and quantum wires [98, 99, 100]. However, only recently has a φ_0-junction been realized experimentally by combining an external magnetic field and spin-orbit coupling [101].

The system proposed in Paper V[1] (Fig. 4.1) is a movable single-Cooper-pair box attached to an anharmonic mechanical resonator in the gap between two superconducting leads with zero phase difference. Cooper pairs can tunnel through the junction via the CPB. Due to symmetry, the net tunneling to the left and right cancel each other out and no net current will flow if the superconducting phases of the leads are equal. However, by applying an alternating potential to the gate, we showed that the CPB position can be parametrically excited. The mechanical vibrations are automatically synchronized with the charging and decharging of the CPB, which establishes a supercurrent through the junction[2].

The system was mathematically modeled as an anharmonic mechanical oscillator coupled to a single-Cooper-pair box (described in section 2.1.3) via position dependent tunneling. The corresponding Hamiltonian is

$$\begin{aligned}\hat{H} = &\left(\frac{\hat{p}^2}{2m} + \frac{m\omega_m^2\hat{x}^2}{2} + \frac{\eta}{4}\hat{x}^4\right) - 2eV_\mathrm{d}\cos(\Omega t)|1\rangle\langle 1| \\ &- \frac{\hbar\omega_\mathrm{J}}{2}\left(e^{-\hat{x}/\lambda}|1\rangle\langle 0| + e^{\hat{x}/\lambda}|1\rangle\langle 0| + \mathrm{H.c.}\right),\end{aligned} \tag{4.1}$$

where η is the mechanical anharmonicity. The neutral state and state with one excess Cooper pair are denoted $|0\rangle$ and $|1\rangle$, respectively. The energy of the charged state is controlled by the harmonic driving field with frequency Ω. The strength of the driving field is assumed to be small compared to the tunneling coupling $eV_\mathrm{d} \ll \hbar\omega_\mathrm{J}$.

[1]The paper builds on the idea, put forth by Gorelik *et al.* [102, 103], that Cooper pairs can be coherently transferred from one superconducting lead to another by moving a single-Cooper-pair box back and forth between the two leads. The state of the box evolves due to an applied electric potential as the box moves. The transport of Cooper pairs through the junction can be controlled by reversing the potential when the box is moved in the other direction. By proper switching of the potential and movement of the CPB, it is possible to establish a direct supercurrent through the junction although the superconducting leads have the same superconducting phase. In contrast to φ_0-junctions, the phenomenon studied by Gorelik *et al.* is a nonequilibrium effect.

[2]Similar automatic synchronization to establish a net current was predicted by Milton *et al.* [104] in normal-conducting systems.

In Paper V, we showed that the supercurrent takes the form

$$\bar{J} \approx \frac{1}{T}\int_{-T/2}^{T/2} \mathrm{d}t\, \mathrm{Tr}\left[\frac{\hat{p}}{2m\lambda}\hat{q}\hat{\rho}\right], \tag{4.2}$$

when the amplitude of vibrations is small compared to the tunneling length λ and where Tr denotes trace with respect to both subsystem. The supercurrent is averaged over one oscillation of the driving field to extract only the direct component of the supercurrent. From Eq. (4.2) it is evident that to have a finite direct supercurrent we need correlation between the movement of the box (corresponding to the operator $\hat{p}$) and the charge of the dot (corresponding to the operator $\hat{q}$). As we will see, such a correlation exists and leads to a supercurrent through the junction.

To qualitatively understand how the supercurrent is established, we can reason as follows. Assume that the CPB is deflected to the left from its symmetric resting position. The mechanical springs will then exert a force on the resonator, which tries to pull the CPB back to the center position. However, the resonator will also experience a softening force due to the tunneling coupling, as discussed in section 2.3. Furthermore, the softening force depends on the state of the electronic system, which is modulated by the driving voltage. As a consequence, the softening force on the mechanical resonator is modulated and therefore able to parametrically excite mechanical vibrations. The parametric excitation can be described as an effective energy landscape for the mechanical resonator (Fig. 4.2). The two minima of the energy landscape correspond to two stable mechanical states oscillating with the driving frequency[3] Ω but with phase shifts $\pm\pi/2$ with respect to the driving field. Similarly, the charge in the CPB oscillates as $q \approx -e[1 + 2\cos(\Omega t)eV_0/\hbar\omega_\mathrm{J}]$. As a result, the mechanical oscillation will be synchronized with the charging and decharging of the Cooper-pair box. The two resulting electromechanical states can be viewed as "chiral states" (Fig. 4.3), which carry supercurrent in opposite directions.

The resulting direct supercurrent increases with amplitude A of the mechanical oscillation and is approximately[4] given by

$$\bar{J}_\pm \approx \pm e\Omega\frac{A}{\lambda}\frac{eV_0}{2\hbar\omega_\mathrm{J}}. \tag{4.3}$$

[3]In the considered system, the parametric excitation is strongest when the driving frequency is close to resonant with the mechanical frequency $\Omega \approx \omega_\mathrm{m}$.

[4]In the analysis we have used a perturbation approach where we have considered the parameters A/λ and $eV_0/\hbar\omega_\mathrm{J}$ to be small.

In the paper, we estimate the direct current to be on the order of 0.1 pA, which is a moderate current since currents down to a few fA can be measured in tunnel-junction structures [105].

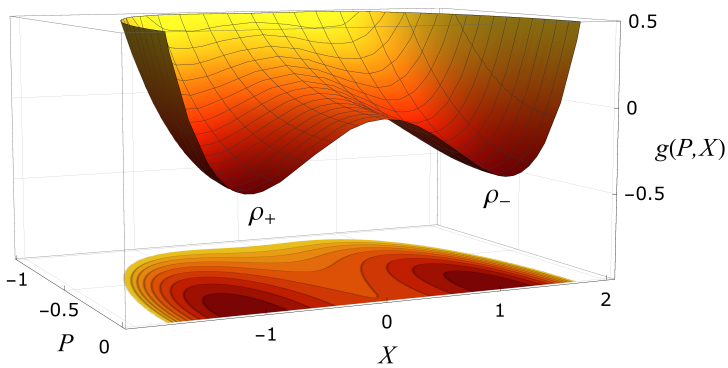

Figure 4.2: The effective energy landscape $g(P,X)$ of the mechanical resonator in the frame rotating with the electric driving field (in the rotating wave approximation [106]). The variables X and P are the so called *quadratures* of the motion, which are related to the amplitude and phase of the oscillation (see Paper V for details). Due to dissipation, the system will relax down to one of the two stable states at the bottom of the effective energy landscape. In these states, the mechanical resonator performs synchronized oscillations with the electronic subsystem, which we refer to as the "chiral states" of the system, see Fig. 4.3. These chiral states carry supercurrent in opposite directions. Small fluctuations may at rare instances induce transitions between the two states [106] and thereby change the direction of the supercurrent. The typical rate at which the transitions occur increases exponentially with increasing temperature.

The mechanical amplitude will be saturated by the anharmonicity in the restoring force of the resonator. This is because the effective distance between the vibrational energy levels of the mechanical oscillator will be altered by the anharmonicity as more energy is pumped into the mechanical oscillation. As a result, the mechanical vibration is pushed out of resonance with the driving field and the efficiency of the pumping mechanism diminishes.

The results presented in Paper V are interesting for several reasons. First of all, the earlier suggestions [90, 91, 92, 93, 94, 95, 96, 97, 98, 99, 100, 102, 103], of how to generate a supercurrent through a junction with zero phase difference, utilized explicit symmetry breaking. However, in Paper V, the symmetry of the system is broken spontaneously by the parametric excitation. This fundamentally different way to generate the

supercurrent results in two coexisting chiral states for the system, which carry current in different directions. It is therefore possible to switch the direction of the current by intentionally perturbing the system from one chiral state to the other. Such manipulation could be interesting for applications[5]. This is in contrast to other zero-phase-difference junctions where the current direction is set by the system parameters. Furthermore, the automatic synchronization of the mechanical and electronic subsystems makes the fabrication of the device and the experimental detection of the phenomenon less demanding compared to the system in Ref. [65].

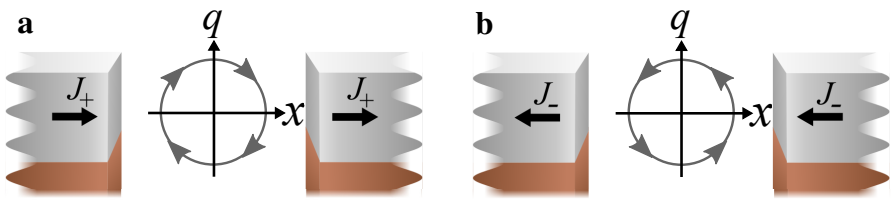

Figure 4.3: The parametric excitation automatically synchronizes the dynamics in charge (q) and position (x) to "chiral states". The charge oscillates in phase with the driving field whereas the parametrically excited mechanical oscillation is approximately $\pm\pi/2$ out of phase with the driving field. As a result, the time-evolution of the electromechanical state in the charge-position space is clockwise (in **a**) or counterclockwise (in **b**). These chiral states coherently transfer Cooper pairs through the junction in opposite directions.

[5]It should be noted that such switching between the chiral states is here modeled as semiclassical, in contrast to coherent manipulation of a qubit.

Chapter 5

Mode Coupling and Internal Resonance

[In the film "Winnie the Pooh", Pooh, Rabbit, Owl, Eeyore, Kanga and Roo are trapped in a hole and Piglet gets a rope — only to cut it up into six pieces.]

Piglet: And six! There! Now we can ALL get out!
Pooh: How very thoughtful you are, Piglet.
Rabbit: Good grief! Tie them together, Piglet! Can you tie a knot?
Piglet: I cannot.
Rabbit: Ah, so you CAN knot.
Piglet: No. I cannot knot.
Rabbit: Not knot?
Pooh: Who's there?
Rabbit: Pooh!
Pooh: Pooh who?
Rabbit: No! Pooh... eh... Piglet, you'll need more than two knots.
Piglet: Not possible.

In a parallel *two-dimensional* world.

In the previous chapters, I described how mechanical vibrations can be coupled to the dynamics of electrons in order to actuate mechanical vibrations and how to utilize the mechanical actuation to excite nontrivial supercurrents.

Another important direction of NEMS research is to not only couple vibrational modes to external fields and charge dynamics, but to couple vibrational modes to each other. Experimental control of interacting modes is rapidly advancing. For instance, modes can be tuned into a strong coupling regime[1] [61, 107]. An important advancement was the demonstration of coherent control and manipulation of the modes by pulse techniques [108, 109]. Coherent control is crucial in information processing applications. Furthermore, driven coupled modes can exhibit very rich nonlinear dynamics, such as multiple hysteresis[2] features [110] and a plethora of coexisting satellite resonances [111]. Mode interaction not only strongly affects the driven response but also influences the dissipation of the modes when the drive is turned off and the system "rings down". Energy can be stored in one mode, which then feeds a second mode during ringdown. The amplitude and frequency of the second mode can thereby be kept steady even after the drive is turned off [112]. However, for a very similar system, namely the one studied in Paper VII, the decay rate of the other mode is not reduced but enhanced due to the mode coupling, as will be described later. The completely different behaviors of these two systems highlight the richness of nonlinear dynamics in mechanical resonators.

For a long time, nonlinearities have been considered unwanted from the point of view of applications. This is partly because the nonlinearities can mediate amplitude fluctuations into frequency fluctuations. For instance, frequency fluctuations are devastating for the performance of filters, since stable frequencies are crucial in order to not lose the signal[3]. Such amplitude induced frequency fluctuations are usually present in an anharmonic (Duffing) oscillator, since the amplitude generates an effective shift of the frequency[4]. However, nonlinearities can in fact be utilized to *stabilize* the frequency of a vibrational mode by coupling it to another mode [113]. Such nonlinear frequency stabilization is a concrete demonstration of the usefulness of nonlinear mode interaction in applications.

[1] In the strong coupling regime studied in [61, 107], the coupling constant g (which is proportional to the frequency splitting of the anti-crossing, see Fig. 5.4) is much larger than the decay rates of the coupled modes.

[2] Hysteresis in the frequency response of NEMS is explained in 5.7.

[3] NEMS filters are also typically very sensitive to changes in temperature since it can change the frequency of the device. This makes high performing NEMS filters difficult to achieve for every day use.

[4] See Fig. 5.7

The frequency-stabilization mechanism utilizes an important type of mode interaction called *internal resonance* (IR). This coupling mechanism is very sensitive to the relation between the frequencies of the involved modes. A small change in for instance the static gate voltage, which slightly shifts the frequencies, can pull the system out of an internal resonance. Comprehensive knowledge of both the nonlinear coupling constants and frequency tuning is therefore important.

In this chapter, I will address this issue by discussing nonlinear mode coupling and frequency tuning in circular graphene resonators (Paper VI). I will then describe the phenomenon of internal resonance and how it can drastically influence both the driven response and the ringdown of a graphene resonator (Paper VII).

5.1 Nonlinearities and Frequency Tuning

In Paper VI, we investigated the nonlinearities and frequency tuning of the vibrational modes of a circular graphene resonator (Fig. 5.1). We did this by starting from the Föppl-von Kármán equations discussed in section 2.2,

$$\begin{aligned}
&\rho_0\ddot{u}_r - \left[\partial_r\sigma_{rr} + r^{-1}\partial_\phi\sigma_{r\phi} + r^{-1}(\sigma_{rr}-\sigma_{\phi\phi})\right] = 0,\\
&\rho_0\ddot{u}_\phi - \left[\partial_r\sigma_{r\phi} + 2r^{-1}\sigma_{r\phi} + r^{-1}\partial_\phi\sigma_{\phi\phi}\right] = 0,\\
&\rho_0\ddot{w} \ + \kappa\Delta^2 w - r^{-1}\left[\partial_r(r\sigma_{rr}\partial_r w + \sigma_{r\phi}\partial_\phi w) + \right.\\
&\qquad \left. + \partial_\phi\left(\sigma_{r\phi}\partial_r w + r^{-1}\sigma_{\phi\phi}\partial_\phi w\right)\right] = P_{\mathrm{st}}(r,\phi) + P_{\mathrm{d}}(t,r,\phi).
\end{aligned} \tag{5.1}$$

They describe the motion of the displacement field

$$\mathbf{u}(r,\phi) = \Big(w(r,\phi), u_r(r,\phi), u_\phi(r,\phi)\Big) \tag{5.2}$$

of the membrane[5] (Fig. 5.1**b**) under the external load $P(t,r,\phi)$. The stress tensor σ_{ij} relates to the displacement field via Poisson's ratio[6] $\nu \approx 0.15$ and the two-dimensional elastic modulus $Eh \approx 340$ N/m [42]. In the stress regime of interest, graphene can be considered as a linear-

[5] Counted from its flat and stress-free configuration

[6] Poisson's ratio is defined as the negative ratio between the transverse and axial strain $\nu = -\epsilon_{\mathrm{trans}}/\epsilon_{\mathrm{axial}}$. When you stretch graphene in one (axial) direction it gets longer in this direction by the amount $\epsilon_{\mathrm{axial}}$. However, it also gets contracted in the transverse direction by $\epsilon_{\mathrm{trans}}$. The same effect can be observed if you stretch a strip of rubber or a balloon.

elastic material[7]. However, a heavily stressed graphene sheet may behave as a nonlinear-elastic membrane [45], but with the imminent risk that the tension will destroy the resonator.

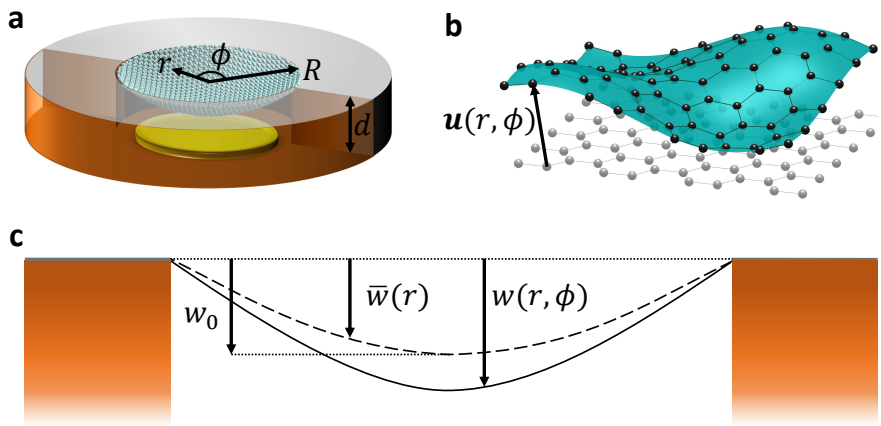

Figure 5.1: **a** Circular graphene resonator with radius R. **b** The displacement field $\mathbf{u}(r,\phi)$ describes how the graphene sheet is deformed (black) from its unstretched flat configuration (light gray). This figure was provided by Professor Andreas Isacsson. **c** The static deflection $\bar{w}(r)$ is due to external loading from the backgate with maximum deflection amplitude w_0. The membrane performs small oscillations $\delta w(r,\phi) = w(r,\phi) - \bar{w}(r)$ around the static configuration.

Before finding the vibrational modes and the corresponding frequencies of the circular resonator, we make two important approximations. Firstly, we neglect the extraordinarily low bending rigidity $\kappa \approx 1.5$ eV [42] of the suspended graphene sheet. This so called *membrane approximation* reflects the fact that graphene is an exceptionally thin material which only requires tiny forces to bend the bonds between the carbon atoms.

Secondly, we assume that the in-plane motion follows the out-of-plane motion adiabatically. This is motivated by the lowest in-plane vibrational modes having much higher frequencies than the out-of-plane modes. The in-plane and out-of-plane frequencies are on the order

[7]The stress σ_{ij} can be approximated as linear in u_r and u_ϕ and quadratic in w due to the geometric nonlinearity given by the Pythagorean theorem, see Paper VI for details.

$$f_{\text{in-plane}} \approx \sqrt{\frac{Eh}{\rho_0 R^2}} \sim 10 \text{ GHz} \;\gg\; f_{\text{out-of-plane}} \approx \sqrt{\frac{T}{\rho_0 R^2}} \sim 100 \text{ MHz}, \tag{5.3}$$

for typical resonators with radius $R = 1$ μm and two-dimensional mass density $\rho_0 \approx 0.75$ mg/m^2 [42]. Hence, a small damping of the in-plane motion will relax it to follow the out-of-plane vibration adiabatically. The adiabatic approximation lets us set $\ddot{u}_r = \ddot{u}_\phi = 0$ in Eq. (5.1). The in-plane displacement can then be solved by treating the instantaneous out-of-plane displacement as a static input. We did this by introducing the Airy stress function [114, §101] which can be seen as a potential to the stress field [50, §7]. When the adiabatic in-plane problem is solved, the dynamics is reduced to a nonlinear partial differential equation for the out-of-plane vibrations. The equations are nonlinear in w since the stress σ_{ij} depends on the out-of-plane deformation. This is due to the so called *geometric nonlinearity* of the system. Another origin of nonlinear out-of-plane motion is the electrostatic coupling to the backgate, which results in a nonlinear force, see Eq. (2.15).

To solve the out-of-plane problem, we performed the mode expansion for the flexural vibrations given by

$$w(t,r,\phi) = \bar{w}(r) + \sum_{\alpha=1}^{\infty} R q_\alpha(t) \Psi_\alpha(r,\phi), \tag{5.4}$$

with dimensionless amplitudes q_α and mode shapes $\Psi_\alpha(r,\phi)$, around the static deflection[8] $\bar{w}(r)$. The mode expansion in Eq. (5.4) allows us to reformulate the dynamics described by the Föppl-von Kármán equations as an infinite set of Duffing oscillators[9]

$$\frac{\partial^2}{\partial \tau^2} q_\alpha + \Lambda_\alpha q_\alpha + \sum_{\beta=1}^{\infty}\sum_{\gamma\geq\beta}^{\infty} Q^\alpha_{\beta\gamma} q_\beta q_\gamma + \sum_{\beta=1}^{\infty}\sum_{\gamma\geq\beta}^{\infty}\sum_{\eta\geq\gamma}^{\infty} C^\alpha_{\beta\gamma\eta} q_\beta q_\gamma q_\eta = \int_0^R \frac{\mathrm{d}r}{R} \int_0^{2\pi} \mathrm{d}\phi \; \Psi^*_\alpha(r,\phi) \frac{R}{T} P_{\mathrm{d}}(t,r,\phi), \tag{5.5}$$

[8] The static solution was obtained by adopting the ansatz $\bar{w}(r) = w_0[1-(r/R)^2]$ for the static deflection and solving the in-plane static configuration self-consistently according to Eq. (5.1). The free energy [114, §97] was then minimized [115, §92] for the center deflection w_0 (Fig. 5.1) under an external parallel-plate-capacitor load.

[9] The dimensionless time $\tau = t\sqrt{T/\rho_0 R^2}$. Hence, the vibrational frequency $f_\alpha = \sqrt{\Lambda_\alpha T/\rho_0 R^2}/2\pi$.

with frequencies $f_\alpha = \sqrt{\Lambda_\alpha T/\rho_0 R^2}/2\pi$. The Duffing oscillators are coupled by the quadratic $Q^\alpha_{\beta\gamma}$ and the cubic $C^\alpha_{\beta\gamma\eta}$ coupling constants (Fig. 5.2), which account for the geometric nonlinearity.

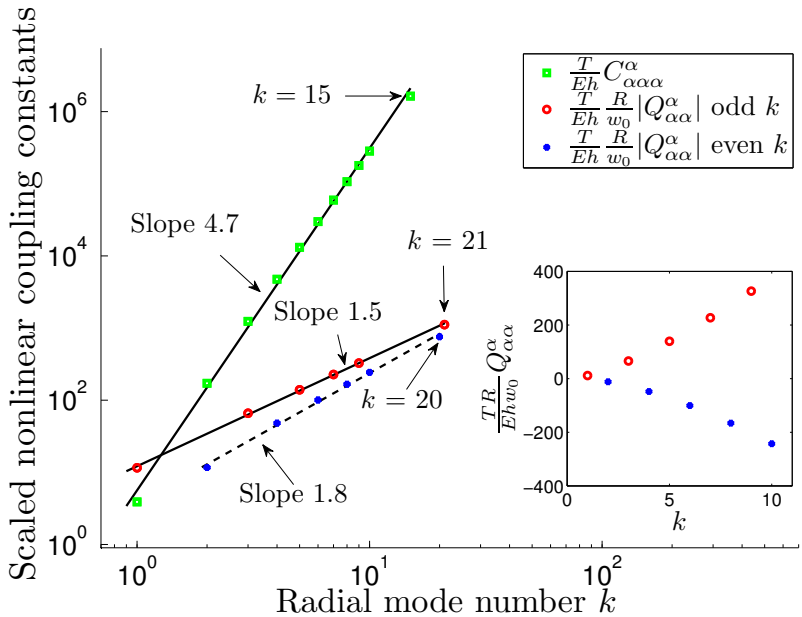

Figure 5.2: Coupling constants for radially symmetric modes ($n = 0$), where the composite mode index $\alpha = (n,k)$ consists of an angular component n and a radial component k. (Coupling constants for asymmetric modes are calculated in Paper VI.) The relative importance of the cubic nonlinear coupling terms compared to the linear terms are proportional to Eh/T where T is the uniform tension in the graphene. Hence, larger tension makes the membrane behave more linear. The quadratic coupling terms are zero for an unloaded membrane but increase linearly with the deflection of the membrane. The magnitude of both symmetric and asymmetric nonlinearities typically increase with mode number.

To describe the dynamics of the membrane as interaction between different vibrational modes has important advantages. The reason is that the modes can be treated as independent, at least for low drive amplitudes where the nonlinear coupling can be neglected. It is therefore often enough to consider only a single mode at a time, which drastically reduces the complexity of the dynamics. Furthermore, different vibrational modes have different frequencies[10]. Hence, if one mode cou-

[10]Obvious exceptions are degenerate modes. However, in a real system, degeneracies are often lifted by imperfections in the fabrication.

ples to another mode, their average interaction will be very small due to the mismatch in frequency — the interaction averages out. This relies on the high quality factors in NEMS, which make the resonance of each mode extremely narrow. As a consequence, vibrational modes can be very selectively addressed. However, the same fact also reduces the possibility of making modes interact when desired.

The vibrational frequencies f_α can be tuned by applying a load to the membrane (Fig. 5.3). A uniform parallel-plate-capacitor load will both enhance the uniform tension and introduce a non-uniform tension[11]. Interestingly, the non-uniform tension introduces frequency crossings (inset of Fig. 5.3 and Fig. 5.4) where the frequencies of two modes intersect. Such crossings do not occur in a uniformly stressed membrane. Modes can therefore be tuned in and out of *internal* resonance with each other. To conclude, modes can not only be selectively addressed, but also, the interaction between modes in an internal resonance can be precisely tuned by for instance varying the gate voltage.

5.2 Internal Resonance

The phenomenon of internal resonance[12] (IR) is not restricted to the case where the involved frequencies coincide, as discussed in the previous section. Internal resonance may also occur when the ratio between two modes is (close to) a rational number [60]. To understand why, it is again beneficial to think about the system quantum mechanically and apply the rotating wave approximation[13] (RWA). Consider a general interaction term in the Hamiltonian proportional to $q_1^n q_2^m$, with amplitude $q_i \to (\hat{c}_i^\dagger + \hat{c}_i)$ of mode i and integers n, m. This interaction term describes processes with n (bosonic) creation and/or annihilation operators for mode 1 with energy quantum $\hbar\omega_1$ and m operators of mode 2 with energy quantum $\hbar\omega_2$. We have to create and annihilate quanta in a way which conserves energy. This introduces conditions for the frequencies as shown in Fig. 5.5. Furthermore, if a resonator is not fiercely driven, only relatively low-power nonlinearities are impor-

[11] The influence of the non-uniform tension can approximately be calculated by first order perturbation theory [116, p. 286].

[12] Also called *autoparametric resonance.*

[13] The same reasoning holds for the "classical" rotating wave approximation where we write $q_1 \propto a_1(t)\cos(\Omega t) + a_2(t)\sin(\Omega t)$ and $q_2 \propto a_3(t)\cos(n\Omega t/m) + a_4(t)\sin(n\Omega t/m)$ and expand the nonlinearities with trigonometric relations to find the slow dynamics of $a_i(t)$ in the rotating frame.

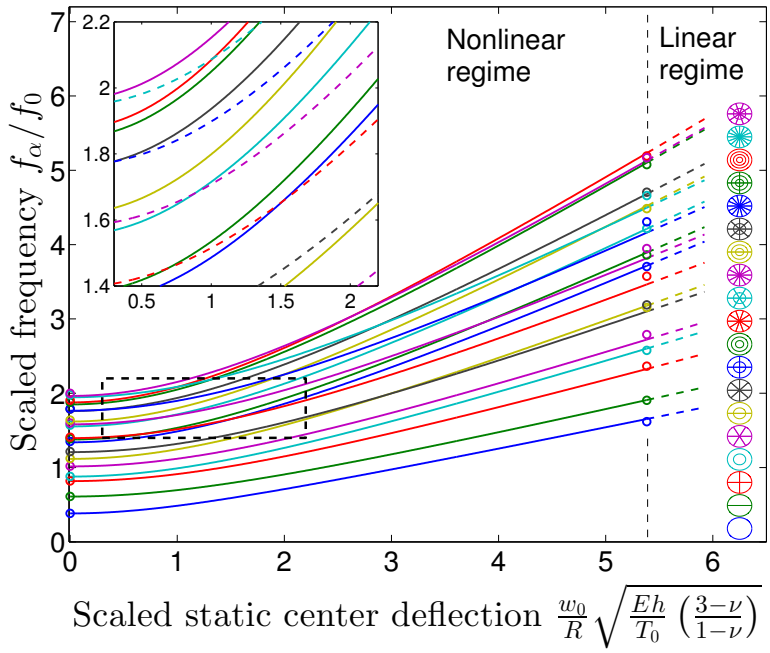

Figure 5.3: Frequency tuning for the lowest vibrational modes with their corresponding mode shapes illustrated on the right. The scaling factor $f_0 = \sqrt{T_0/\rho_0 R^2}$ with pre-stress T_0 and the circles correspond to COMSOL Multiphysics simulations. The non-uniform tension introduces frequency crossings (inset). The crossings are mainly due to the modes with radial mode number $k = 1$ (dashed) being less stiffened by comparison to other modes. These less stiffened modes are the ones with only one circle in the mode shapes. The frequencies can cross since there is no "linear coupling" between the modes. If such linear coupling existed, the modes would instead exhibit an avoided crossing (Fig. 5.4). Avoided crossings are not present for the perfectly circular membranes shown here, due to rotational symmetry. However, if the symmetry is broken, for instance due to imperfect fabrication, such coupling might be introduced.

tant. The easiest internal resonances to observe are therefore typically of the kind n "to" 1, commonly written as $n:1$, with ratio between the involved frequencies $n = \omega_2/\omega_1$.

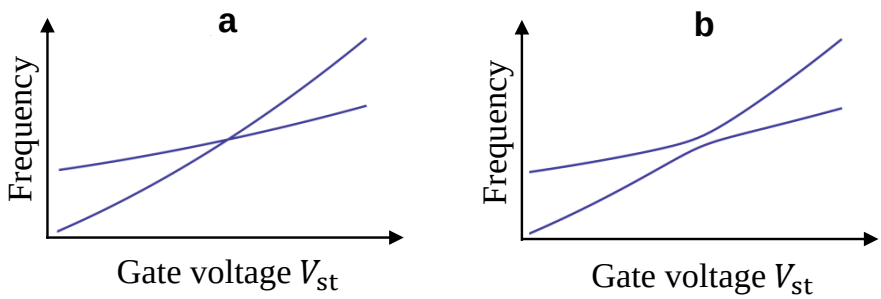

Figure 5.4: **a** Frequency tuning of two modes exhibiting a frequency crossing. **b** If we add a small linear interaction between the modes they will hybridize into two new modes. However, the hybridization is only pronounced close to the crossing point, where the interaction is comparable to the separation in frequency. Far away from the crossing point, the interaction can be neglected. As a consequence of the interaction, the two frequency branches repel each other in a so called *avoided crossing*, also known as *anti-crossing*. The height of the avoided crossing is proportional to the interaction.

So, what will happen with the dynamics if we couple two modes in an internal resonance? One important phenomenon is that energy can be transferred between the modes, as described in Fig. 5.5. We can therefore expect a drastic influence on the dissipation of the modes, depending on if they are in or out of the IR. This is indeed what was observed in Paper VII, where we investigated a 3:1 IR in a multi-layer graphene drum similar to the one in Fig. 2.1. We could also expect the driven response to be richer close to the internal resonance. This chapter aims to describe the basics of nonlinear modeling of mechanical resonators and to understand qualitative features in the dynamical response.

To theoretically study the 3:1 IR, we modeled the two interacting modes as Duffing oscillators. The frequency ratio of 3 indicates that the nonlinear term in the Hamiltonian $\propto g q_1^3 q_2$ is probably most important[14]. The coupled equations are therefore

[14]For a review on nonlinear dynamics in NEMS see Ref. [117]. Especially, it describes how general nonlinear mode equations can be reduced to effective ones.

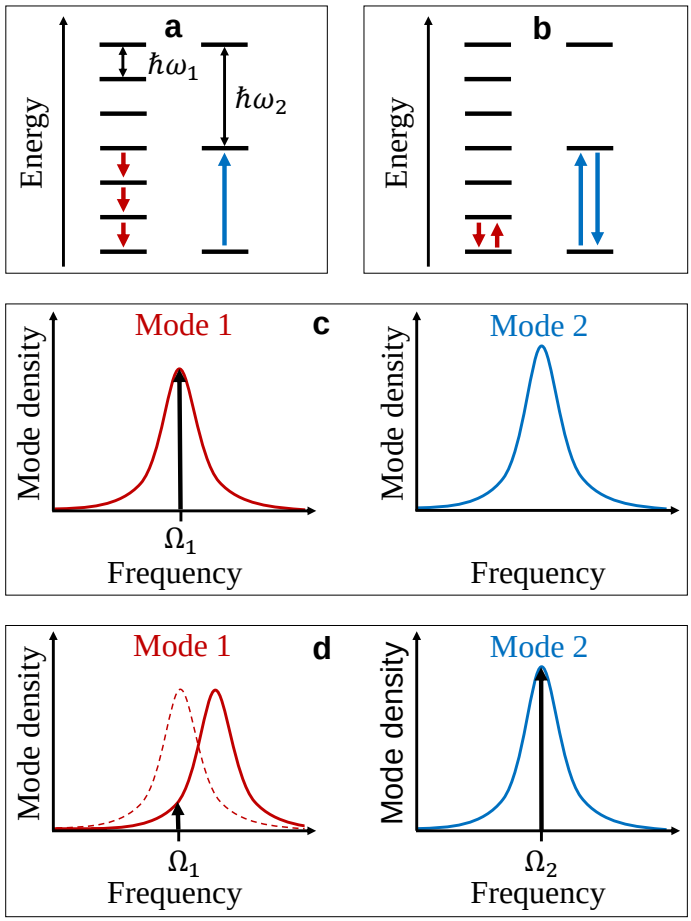

Figure 5.5: Mode interaction for two modes with $\omega_2 = 3\omega_1$. **a** The coupling term $q_1^3 q_2$ induces processes where three quanta in mode 1 are annihilated and turned into one quantum in mode 2. Mode 2 is thereby pumped by mode 1 (the reverse process is also induced). **b** The dispersive term $q_1^2 q_2^2$ couples the two modes but cannot transfer energy from one mode to the other (and conserve energy at the same time). However, the dispersive coupling can induce a shift in frequency of the other mode. Assume that mode 2 oscillates with constant amplitude A_2. In the spirit of the averaging technique, we can effectively set $q_1^2 q_2^2 \approx q_1^2 A_2^2/2$, which is just a frequency shift of mode 1 (cf. the Hamiltonian term $\omega_1^2 q_1^2$). **c** To illustrate the nonlinear dispersive effect, assume that mode 1 is weakly driven but mode 2 is not. Mode 1 will respond with a moderate amplitude to a resonant drive field $\Omega_1 = \omega_1$. **d** If we start to strongly drive mode 2 at its resonance, the nonlinear dispersive coupling will pull the frequency of mode 1 out of resonance with its drive field (the mode density of mode 1 has been shifted in frequency). By this means, the energy in mode 1 can be controlled by mode 2, even though no energy is transferred *between* the modes.

$$\ddot{q}_1 + \gamma_1 \dot{q}_1 + \omega_1^2 q_1 + \alpha_1 q_1^3 + 3g q_1^2 q_2 = f\cos(\Omega t), \tag{5.6}$$

$$\ddot{q}_2 + \gamma_2 \dot{q}_2 + \omega_2^2 q_2 + \alpha_2 q_2^3 + g q_1^3 = 0, \tag{5.7}$$

where we drive the fundamental mode close to its natural frequency $\omega_1 \approx \Omega$ and both oscillators are weakly damped.

In practice, the system parameters have to be fitted to experimental data, since the response is very sensitive to the values of the parameters. Theoretical estimations, which assume idealized conditions, only give a crude estimate of the parameters. However, if the theoretical estimate differs significantly from the experimentally extracted values, it might indicate that the measured response has another physical origin.

An important reason for the sensitivity of the parameters is that even very small changes in the parameters can drastically change the qualitative dynamics of the system. At these special parameter values, the system is said to undergo a *bifurcation*. For instance, the number of stationary states can change and oscillatory motion can bifurcate (be initiated) from the boundary between qualitatively different parameter regions. Different parameter regions are mapped out in a so called *bifurcation diagram*, which is an important tool to understand complex dynamics in nonlinear systems. As seen in Fig. 5.6, the response of the device is indeed complex. The question is: can we understand qualitative features of the behavior, despite its complexity? With the aim to understand the dynamics at the IR, let us start by looking into the dynamics as if the modes were uncoupled.

When the modes are uncoupled ($g = 0$), the amplitude response of mode 1 is only affected by its Duffing nonlinearity, as explained in Fig. 5.7**a**. A positive Duffing nonlinearity tilts the Lorentzian linear response to the right, whereas a negative Duffing nonlinearity tilts the linear response to the left. The corresponding bifurcation diagram, which is important to understand for the remainder of this chapter, is described in Fig 5.7**b**. Being reminded of the single mode Duffing response by these figures, we now add the second mode but still assume that they are uncoupled. If we simultaneously drive mode 2 with a term $f_2\cos(3\Omega t)$, the combined bifurcation diagram would qualitatively be as in Fig. 5.8**a**, if mode 2 is slightly red tuned i.e., $\omega_2/3 < \omega_1$, and has a positive Duffing nonlinearity. For a downward frequency sweep, each mode would follow its Duffing response, unaffected by what happens to the other mode, see Fig 5.8**c**.

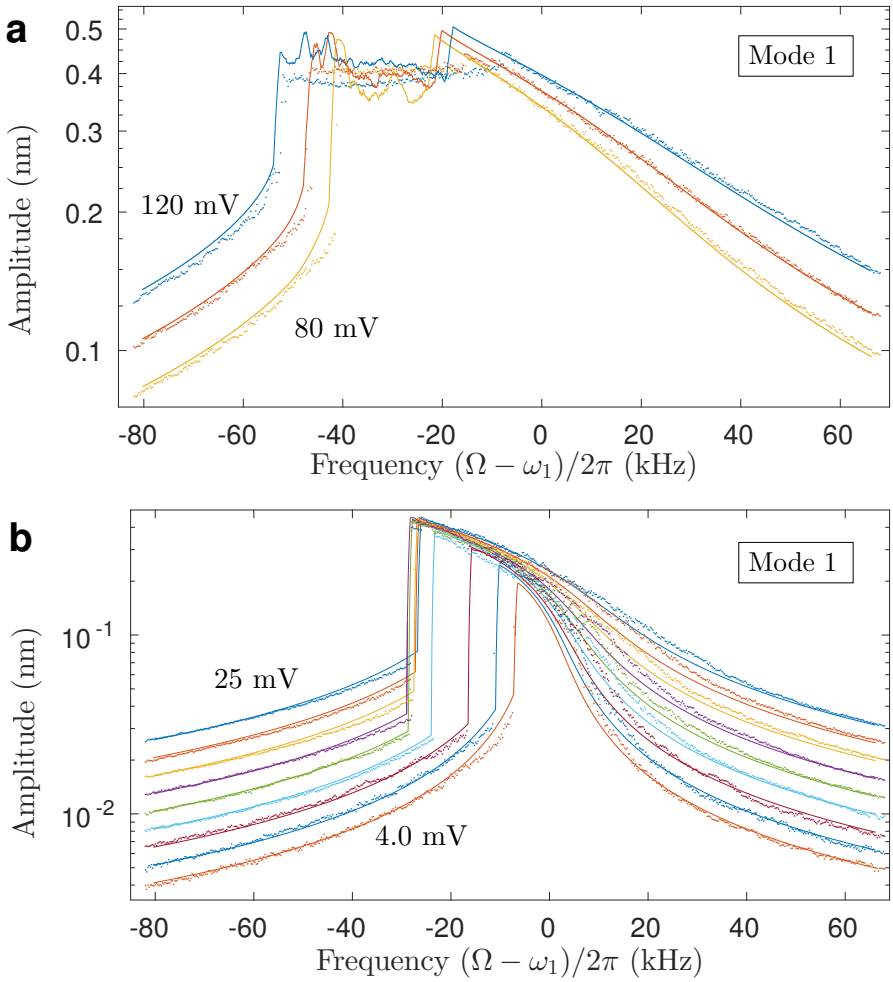

Figure 5.6: Amplitude response of mode 1 for downward frequency sweep. Curves correspond to drive voltages ranging from 4.0 mV to 120 mV. Theoretical model (solid) fits well with the measured response (dots) presented in Paper VII. **a** For high drive, the amplitude response drops down to a plateau. **b** For low drive, the ordinary Duffing response (Fig. 5.7) is observed. When the drive is increased to moderate strength (~ 20 mV), the frequency at which the amplitude drops to the low-amplitude branch saturates. This happens when the effective frequencies ω_i^{eff} (due to Duffing frequency shift) of the two modes come into internal resonance [17]. IR can therefore be achieved in at least two ways. Either, we can drive one mode strongly and utilize the frequency shift due to the Duffing nonlinearity to achieve $\omega_2^{\text{eff}} = n\omega_1^{\text{eff}}$ or we can tune the frequencies into IR by static means.

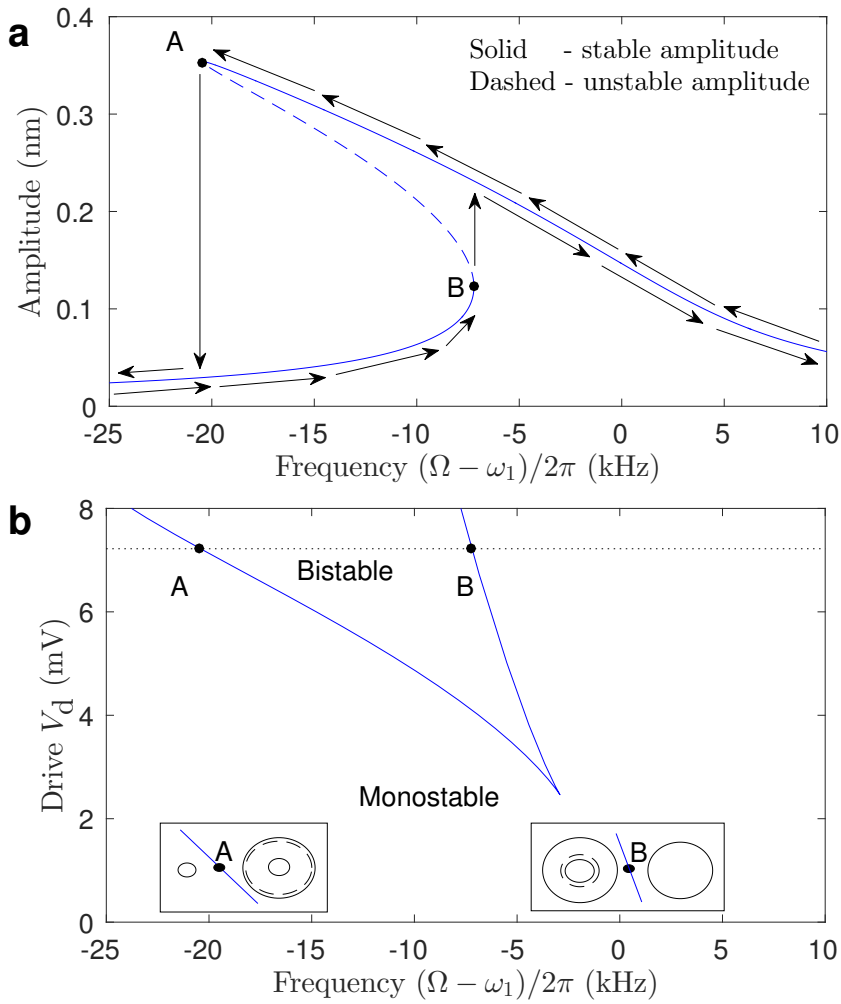

Figure 5.7: **a** Amplitude branches of a driven Duffing oscillator for fixed drive amplitude V_d. The negative Duffing nonlinearity softens the natural vibrational frequency ω_1 if the vibration is driven to a large amplitude. As a consequence, the system exhibits a stable (solid) large amplitude branch below ω_1, where the drive frequency Ω is (close to) resonant with the effective mechanical frequency. The system is therefore partly bistable and will exhibit hysteresis since the response will depend on the sweep direction (arrows). **b** Bifurcation diagram of the driven Duffing oscillator. The solid line separates the monostable and bistable regions. The dotted line corresponds to the amplitude response in **a**, with bifurcation points A and B as indicated. **b** (inset) To the right of bifurcation point B, the system is monostable. If the frequency is changed to the left of B, one stable and one unstable limit cycle are created at small amplitude. If the frequency if further decreased, the unstable limit cycle grows and annihilates the large amplitude state at **A**, cf. **a**.

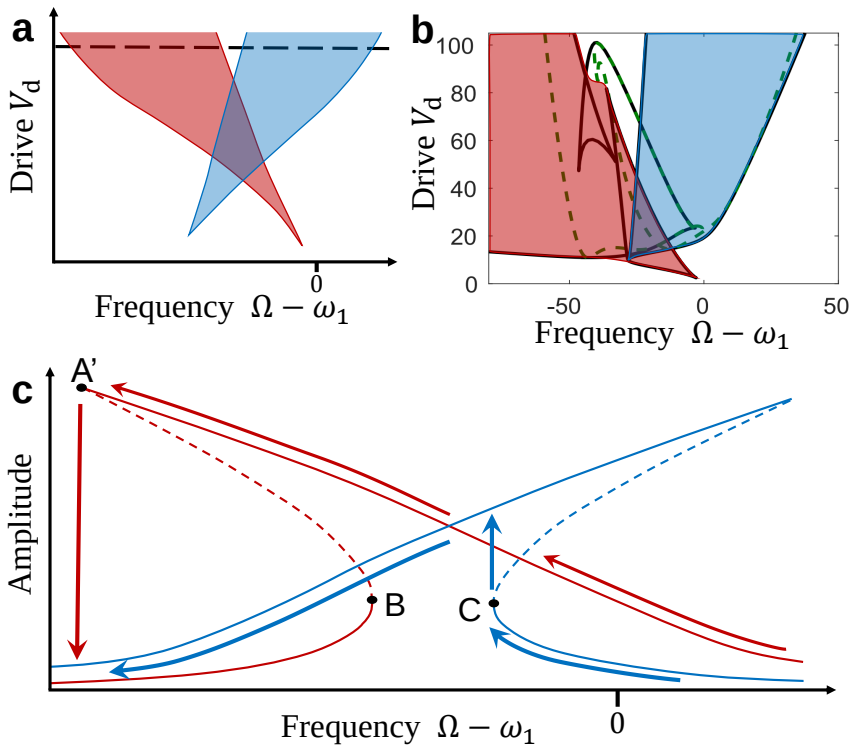

Figure 5.8: **a** Bifurcation diagram of the uncoupled Duffing oscillators. Mode 1 (red) and mode 2 (blue) are driven by $\cos(\Omega t)$ and $\cos(3\Omega t)$, respectively. Shaded areas indicate the bistable region for each oscillator. **b** Bifurcation diagram with parameters fitted to the device response in Fig. 5.6. When the modes are coupled, by letting mode 1 drive mode 2 as q_1^3 (see Eqs. (5.6)-(5.7)), we can still recognize the bifurcations from the uncoupled case (shaded), although distorted. **c** If we perform a downward frequency sweep of the uncoupled modes (at V_d indicated by the dashed line in **a**), we would follow the arrows.

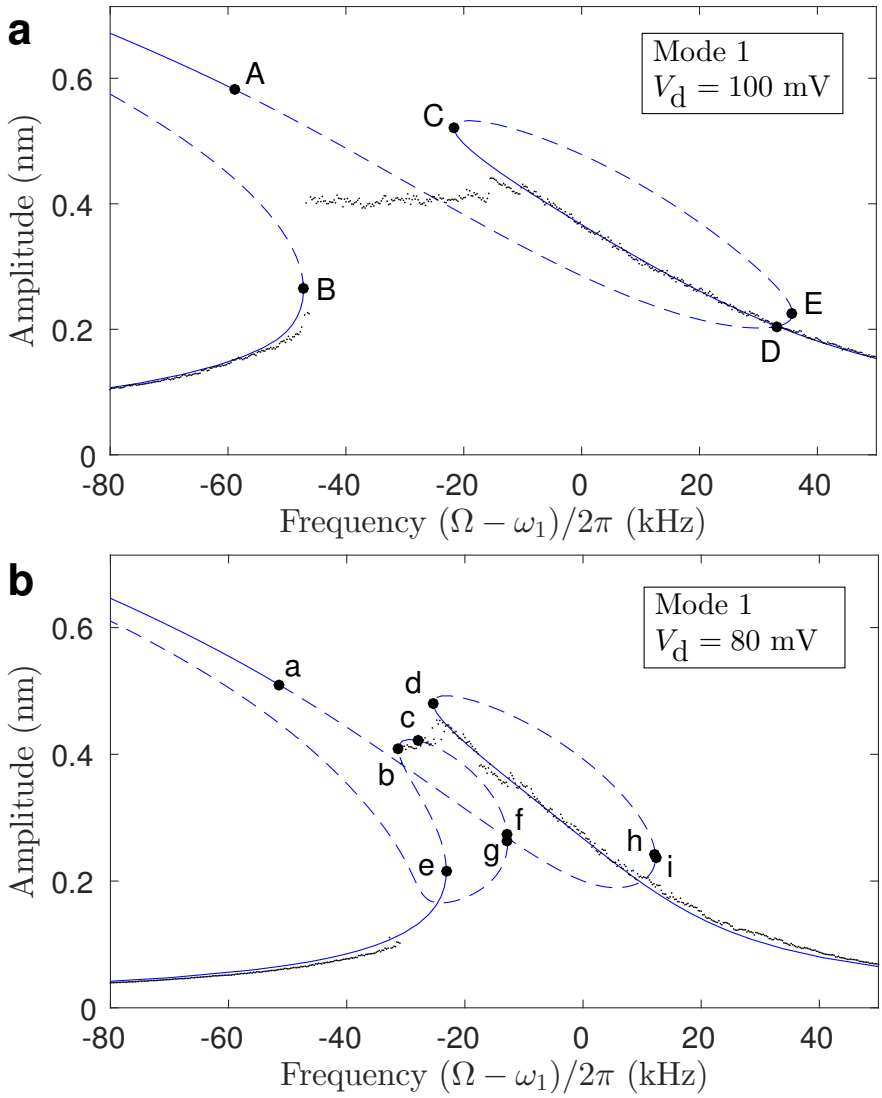

Figure 5.9: Measured amplitude response for downward frequency sweep (dots) compared to the IR model. **a** and **b** correspond to the two dashed lines in the bifurcation diagram in Fig. 5.10. The modeled amplitude response and bifurcation diagrams were calculated with MATCONT [118].

However, when mode 2 is driven not externally but by mode 1 via the coupling term gq_1^3, the modes will interact. As a consequence, the upward jump in amplitude of mode 2 at point C (Fig. 5.8**c**) will affect the response of mode 1 and push it down a little bit in amplitude, as seen in Fig. 5.9**a**. Naively, this can be explained by the fact that the high-amplitude state of mode 2 will lead to increased dissipation[15] of mode 2. To support the higher amplitude state of mode 2, energy has to be transferred to it at a faster rate from mode 1. As a consequence, the amplitude of mode 1 will be suppressed. This is what explains the sudden disappearance of the stable amplitude branch to the right of the plateau in Fig 5.6**a**.

Interestingly, there is no stable amplitude state to drop to in the frequency interval B-C (Fig. 5.9**a**). Instead, the resonator relaxes towards an amplitude-modulated state. Depending on the parameters, the amplitude-modulated state is typically a variation of a torus state (see Fig. 5.10**b**) but may even be chaotic. In the measurement, the modulation of the amplitude is averaged out, which is the reason for the flat plateau[16] response between B and C. Numerical simulations indicate that the amplitude-modulated state makes complicated transitions from torus states (Fig. 5.10) via period doubling bifurcations[17] to chaotic states. Similar transitions have been observed in nanomechanical resonators under other conditions [120].

Furthermore, the system does not continue on the high-amplitude branch of mode 1 and drops down as expected at point A' (Fig. 5.8**c**). Instead, the system drops *down* in amplitude at B, where the system usually jumps up in amplitude for an upward frequency sweep. This is probably because of large fluctuations (Fig. 5.11) in the amplitude-modulated state, which kick the system into the basin of attraction of the low-amplitude state when it emerges. The high-amplitude branch close to A' is therefore inaccessible by this experimental procedure. To experimentally study the IR by approaching it from the high-amplitude branch closer to A' requires a non-trivial preparation of the system.

For instance, we can try to get to the high-amplitude state close to A' by shifting the static gate voltage so that mode 1 becomes red detuned away from the IR. There, we can get up to the high-amplitude branch

[15] The damping is modeled to increase linearly with the amplitude.

[16] A similar plateau has been observed in a 2:1 IR [119].

[17] During a (supercritical) period doubling bifurcation, the period of the dynamics is doubled.

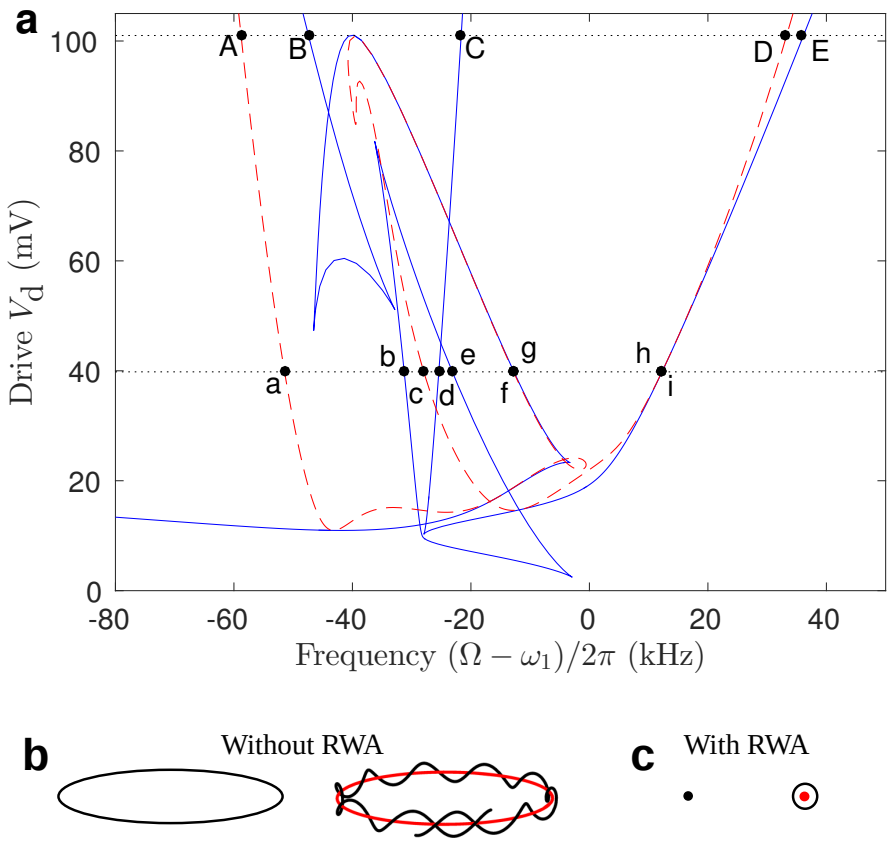

Figure 5.10: **a** Bifurcation diagram for the IR model, including limit points of cycles (LPC) (solid) and Neimark-Sacker (NS) (dashed) bifurcations. At an LPC bifurcation, two periodic orbits are born (cf. Fig. 5.7**b**). The NS bifurcation is here a consequence of the interaction between the two modes. **b** At a (supercritical) NS, a stable (black) limit cycle becomes unstable (red) and the resonator performs small oscillations on a torus (the "shell of a donut") around the unstable limit cycle. The motion will then generally become quasi-periodic. This is a higher-dimensional analogue of the (supercritical) Hopf bifurcation, which is when a stable fixed point becomes unstable and gives birth to a stable limit cycle. **c** In the RWA, the dynamics of the system is "reduced by one oscillation". For instance, in the RWA, a stable limit cycle is characterized by its amplitude and phase, i.e., a fixed point and not a periodic orbit. Hence, in the RWA, the NS is reduced to a Hopf bifurcation. At some special points, the Hopf curve (dashed) undergoes a Bogdanov-Takens (BT) bifurcation and continues as a neutral saddle, which is not a bifurcation. This can occur where a Hopf curve tangents a curve of limit points. The reader is encouraged to find candidates for the BT bifurcation in the bifurcation diagram above and see illustrations of the bifurcations at *scholarpedia.org*.

of mode 1 and then turn the static voltage back to the IR. Similar non-trivial paths to access dynamical regimes have been proposed in Ref. [121].

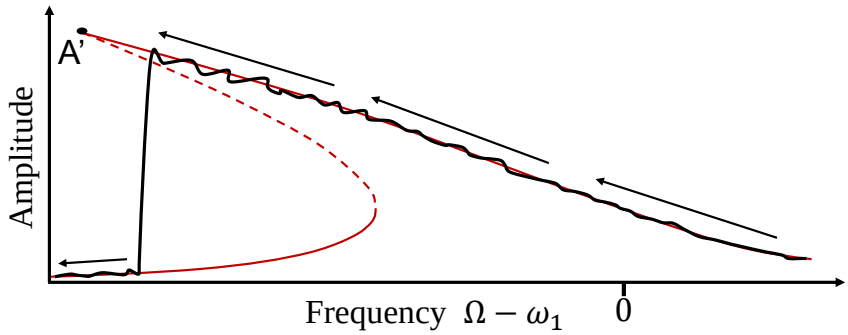

Figure 5.11: Fluctuation induced transition. Noise can induce a transition from one state to another state, even though no bifurcation is passed. For instance, as we slowly sweep the drive frequency downwards, fluctuations may kick the resonator out of the high-amplitude state, so that it falls down to the low-amplitude state before bifurcation point A' is reached. During experiments, it is therefore important to not sweep the frequency so slowly that there is a considerable risk that noise kicks the system out of its state. On the other hand, bifurcation points might be passed unnoticed if the frequency is swept too quickly. Such noise induced transitions and unnoticed bifurcations complicate the interpretation of experimental data.

So far, I have only discussed the interplay between the two modes during driven response. How does the IR affect the ringdown of the vibrating modes if the drive is turned off? The procedure of a ringdown experiment is explained in Fig. 5.12**a**. In the case of uncoupled resonators, each mode decays individually with its decay rate γ_1 and γ_2, respectively. However, when the modes are coupled in the IR, they can become hybridized. This takes place when the effective coupling g_{eff} is strong in comparison with the difference in dissipation rates and effective detuning between the modes[18]. The effective coupling $g_{\text{eff}} \propto gE^{(n-1)/2}$ increases with increasing total (Manley–Rowe) mode energy E. As a consequence, the coupling becomes strong when the vibrations are strongly driven and the modes hybridize. When the drive is turned off, the energy decays freely from the hybridized state as a whole. As the energy decreases, so does the nonlinear coupling be-

[18]See Paper VII for details.

tween the modes and eventually the modes decouple. This results in a crossover in the ringdown trace for the fundamental mode amplitude (Fig. 5.12**b**). Internal resonance is therefore one important origin for nonlinear dissipation in NEMS.

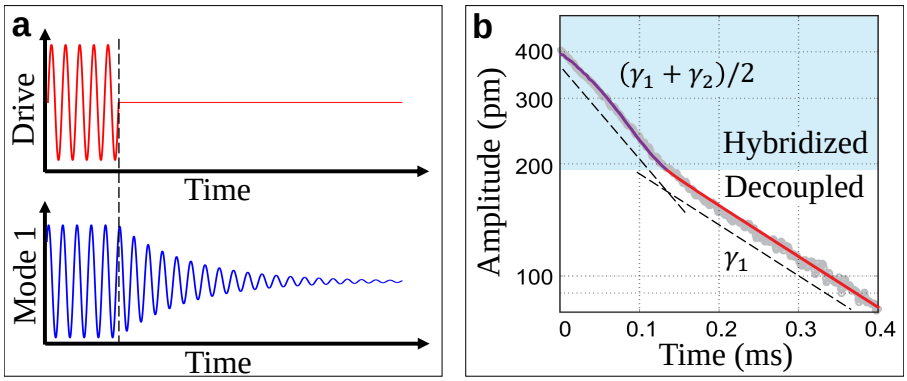

Figure 5.12: **a** Procedure of a ringdown experiment. The vibrations are first driven to large amplitudes and possibly into a hybridized state. The drive is then suddenly switched off and the free decay of a mode is measured, here with a simple exponential decay. **b** Average ringdown for mode 1 from a hybridized high-amplitude-modulated state to low amplitudes, presented in Paper VII. As the energy dissipates from the hybridized state, the coupling becomes weaker and the modes eventually decouple. In this experiment, the decoupling takes place at ∼200 pm. As the modes decouple, the dissipation rate changes from approximately $(\gamma_1 + \gamma_2)/2$ to γ_1.

Chapter 6

Outlook and Conclusions

"Happy, happy"

Lars-Johan Åge

Our experimental dexterity with NEMS are rapidly advancing and exhibit maturing coherent control. Nanomechanical resonators are built to interact with external objects in ways which connect diverse fields of physics. Strong nonlinear effects are being explored and utilized, even tailored. These experimental advances raises the ambitions of the field of nonlinear dynamics in NEMS. Their extraordinary parameters make it possible to access and study exotic parameter regions with complex dynamical response. The next step is to master the nonlinear effects in the lab and to apply them in new ways. However, mastering the effects is not enough, a huge amount of creative work lies ahead in order to achieve novel applications. The success of nonlinear NEMS will likely not be determined by how they can improve existing technologies, but by which completely new applications they enable.

Even to master the nonlinear effects is a demanding task. The world of nonlinear dynamics in NEMS is huge, due to the large accessible parameter space. Experimental examination of a device can therefore be overwhelming and the results can be hard to interpret and explain. At the same time, from the theoretical side, it makes little sense to simulate the whole parameter space numerically for a general device without restrictions. Furthermore, theoretical models for exotic, but less robust, features in special regions are difficult to realize experimentally. This is because it is still very challenging to tailor all parameters in order to reach a specific nonlinear regime of a theoretical model. For faster

advances towards mastering relevant observable features, both the experimental and theoretical efforts need guidance — a map to navigate with in the nonlinear world.

Bifurcation diagrams can serve as the maps we require. Bifurcation diagrams may not only reveal where the device exhibits exotic dynamics, they could also tell us how to get there. This is important, since exotic nonlinear dynamics can be *hidden* and only accessed if non-trivial tuning paths through parameter space are followed. The common experimental technique of using cascades of frequency sweeps might not be enough. Without a map, such regimes would probably be forever lost treasures. Knowledge is what makes creativity possible.

One important question to address is: how to draw such a map? It has to correspond to the nonlinear world of the device at hand. To draw a crude map, for instance for a two-mode IR, we could start by characterizing the low-amplitude basic response of each mode. We have then drastically reduced the relevant parameter space. A standard cascade of frequency sweeps can then be performed to get an estimate of the coupling coefficient. The parameters can be adjusted to the cascade data in order to have a reliable map of the local nonlinear landscape. This is basically what was done in Paper VII and shown in Fig. 5.10**a**. However, the theoretical work could then be extended since the fitted equations contain a lot of information. By extracting this information through the procedures of bifurcation theory, several exotic dynamical regions were predicted, as shown in the refined bifurcation diagram in Fig. 6.1**a**. The map is now ready for experimental treasure hunting.

However, there are at least two aggravating circumstances which have to be taken into account when drawing and using a bifurcation map. Firstly, it is not always clear which kinds of interactions are most important for the behavior of a specific system. A tough question is therefore: which nonlinear equations should be used in the theoretical model? To find an appropriate answer, a combination of qualified guesswork and complementary experimental investigations are most likely required. Secondly, what is the influence of fluctuations? This question has only been briefly touched upon in this thesis, but it is an important issue in the field of NEMS. Fluctuations may blur the dynamics, causing special dynamical points to be difficult to study. For this reason, slightly larger devices, i.e., microelectromechanical systems, might be more suitable since they typically contain less noise but still offer widely tunable parameters with well separated time scales.

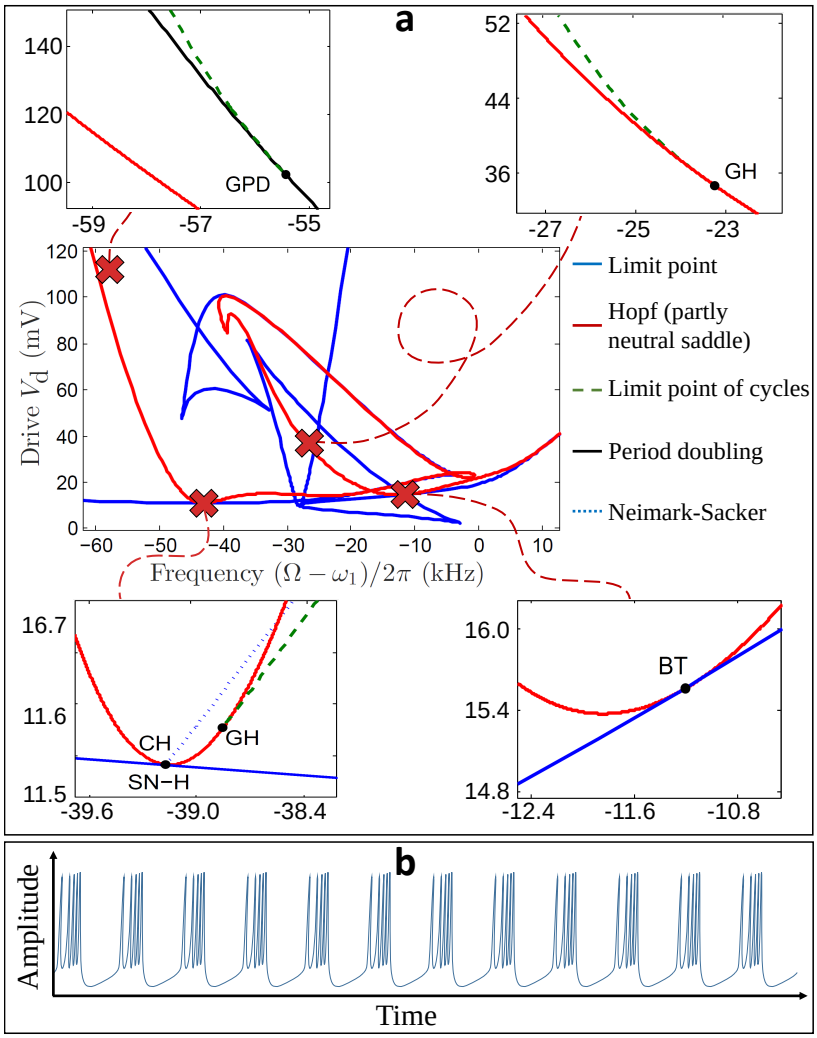

Figure 6.1: **a** The bifurcation diagram is a map of the nonlinear world of a device which can be used to guide experimental investigations. This map is a refined bifurcation diagram (still heavily simplified) of the device in Paper VII. The map reveals several exotic dynamical regions (GPD – Generalized period doubling, GH – Generalized Hopf, CH – Chenciner generalized Hopf, SN-H – Saddle-node Hopf, BT – Bogdanov-Takens). Some of the regions might be hidden and can only be accessed by non-trivial adjustments of parameters (illustrated by the dashed paths through parameter space), which are also predicted by applied bifurcation theory. **b** Bursting — can it be observed in NEMS?

Bifurcation analysis is, of course, often used to understand experimental results and to propose new experiments from scratch. However, many nonlinear systems are very sensitive to the system parameters and it is in practice still very difficult to simultaneously tailor several nonlinear coefficients. It is therefore crucial to have direct feedback between the experimental and theoretical designs of experiments. A synergistic procedure of constructing and following bifurcation maps will not only help us find the dynamics which the systems were designed for, but much more importantly: such a procedure will help us find what we did not originally expect. This procedure is in no way limited to NEMS, but may be fruitful in a vast number of nonlinear systems in physics, chemistry and biology.

Furthermore, due to the general applicability of bifurcation theory and nonlinear dynamics, different scientific fields can often inspire one another. Perhaps this is another opportunity. In neuroscience, a phenomenon called *bursting* is commonly observed in neuron activity. In the bursting state, a neuron first repeatedly fires signals, which are followed by a "quiet" period, before the next burst of firing occurs (Fig. 6.1**b**). Bursting neurons typically require well separated dynamical time scales, at least a three-dimensional phase space and several possibilities to switch between oscillatory and "steady" motion. The conditions resemble the situation of the internal resonance in NEMS. A tickling question arises: can we achieve bursting NEMS?

To conclude, fascinating and useful nonlinear dynamics can be achieved by making mechanical modes interact with external structures and each other. When two or more modes interact, the increased dimensionality of the relevant phase space allows for much richer dynamics than the two dimensions of a single mode. The system may burst, even be chaotic; "knots can be knot". To accelerate the understanding and applicability of the rich nonlinear dynamics of coupled modes, close collaborations between experts in both theoretical and experimental physics are required. One valuable tool to achieve synergistic effects is the above described construction and utilization of bifurcation diagrams — the maps of nonlinear dynamics. An exciting and prosperous future lies ahead if we can tame the complexity of high-dimensional nonlinear mode dynamics. Or in other words:

There's plenty of room in higher dimensions.

Acknowledgements

My greatest gratitude goes to my supervisor Leonid Gorelik. I have immensely enjoyed our open and stimulating discussions during the past years. Together with Andreas Isacsson, you have stretched my mind into its nonlinear regime, where I have experienced both difficult adversities and, more importantly, the greatest of joys.

Furthermore, I would also like to thank my colleagues. Some of you have tiptoed around in the corridors, others have been spread out all over the world. In particular, my collaborations with Adrian Bachtold's group in experimental nanomechanics provided a new dimension to my work. Special thanks go to Anton Vikström. After some time sharing office, we *actually* started to cooperate. Several of our discussions regarding quantum physics started, in a not too early morning, with one of us stating something. The afternoon was then spent on trying to understand if we understood what was stated. If so, the following day was spent on understanding if what was said had any physical meaning or relevance.

While writing this thesis, I had great support from Anton Vikström and Andreas Isacsson, both of whom contributed with several important and valuable comments on the technical content. I would also like to thank the father[1], the sister[2] and the holy spirit[3] for proofreading my thesis.

Finally, I would like to thank my friends and family for your support and making me feel safe and loved even in moments of despair.

Now, my life continues, and I hope it will be filled with complex dynamics, not least between minds.

[1]Sven Eriksson
[2]Ellinor Eriksson
[3]Mathilda Engström

Appendix A

Models for Dissipation in Mechanical Oscillators

In this appendix, I briefly describe the most straightforward ways to model dissipation in classical and quantum mechanical oscillators.

Classical Model

We can model linear and nonlinear dissipation in a classical oscillator by adding the right hand side of

$$\ddot{x} + \omega_{\mathrm{m}}^2 x = -\left(\gamma_L + \gamma_{NL}\left(\frac{x}{l}\right)^2\right)\dot{x} \tag{A.1}$$

in the equations of motion for the mechanical oscillator. The strength of linear and nonlinear damping is given by $\gamma_{\mathrm{L}} > 0$ and $\gamma_{\mathrm{NL}} > 0$, respectively. The right hand side describes friction, which counteracts the motion of the oscillator. At small amplitudes, $x \ll l$, the linear damping dominates. If the amplitude increases, the nonlinear dissipation increases in efficiency and dominates at large amplitudes. Nonlinear dissipation of this form has been used successfully to model nonlinear damping in CNTs [59].

Quantum Model

One common dissipation operator in bosonic systems is the Lindblad superoperator

$$\mathcal{L}_{\mathrm{L}}(\hat{\rho}) = \gamma_{\mathrm{L}}\left((\bar{n}+1)\left(\hat{c}\hat{\rho}\hat{c}^\dagger - \frac{1}{2}\{\hat{c}^\dagger\hat{c},\hat{\rho}\}\right) + \bar{n}\left(\hat{c}^\dagger\hat{\rho}\hat{c} - \frac{1}{2}\{\hat{c}\hat{c}^\dagger,\hat{\rho}\}\right)\right) \tag{A.2}$$

with coupling strength γ_{L}, average number of bosons in the thermal bath $\bar{n}$ given by the Bose-Einstein distribution and anti-commutator $\{\hat{A},\hat{B}\} = \hat{A}\hat{B} +$

$\hat{B}\hat{A}$. The Lindblad superoperator can be derived from Liouvillian dynamics of the total system fulfilling the Liouville-von Neumann Eq. (2.5) [122]. The Lindblad superoperator describes dissipative single-quantum processes where one vibron is added or annihilated at a time. If no external forces bring the subsystem out of equilibrium, it will thermalize due to these processes and adjust to the temperature of the environmental bath. Such single-vibron interaction gives rise to "linear dissipation" of the mechanical motion with respect to the amplitude of actuation.

Multi-vibron processes can be described by the superoperator [123]

$$\mathcal{L}_{\mathrm{NL}}(\hat{\rho}) = \gamma_{\mathrm{NL}}\left[(\bar{n}+1)\left(\hat{c}\hat{c}\hat{\rho}\hat{c}^{\dagger}\hat{c}^{\dagger} - \frac{\{\hat{c}^{\dagger}\hat{c}^{\dagger}\hat{c}\hat{c},\hat{\rho}\}}{2}\right) + \bar{n}\left(\hat{c}^{\dagger}\hat{c}^{\dagger}\hat{\rho}\hat{c}\hat{c} - \frac{\{\hat{c}\hat{c}\hat{c}^{\dagger}\hat{c}^{\dagger},\hat{\rho}\}}{2}\right)\right] \quad \text{(A.3)}$$

with coupling strength γ_{NL}. It describes processes where two vibrons are either created or annihilated at the same time. Multi-vibron processes give rise to "nonlinear dissipation" of the mechanical motion with respect to the amplitude of actuation.

Appendix B

The Rate Equation

In this appendix, I derive the rate equation of the dynamics in Paper II. The movable QD is coupled to an electronic reservoir and the energy of the QD state is modulated by a harmonic external field. The dynamics of the density operator $\hat{\rho}$ for the coupled system is governed by the Liouville-von Neumann equation

$$i\hbar\frac{\partial}{\partial t}\hat{\rho} = \left[\hat{H}_0 + \left(e^{i\Omega t} + e^{-i\Omega t}\right)\hat{H}_{\rm i},\hat{\rho}\right] \tag{B.1}$$

where $\hat{H}_0$ contains the non-interacting hybridized electronic and mechanical subsystems (see Paper II), whereas the electromechanical coupling has been written as $\hat{H}_{\rm int} = \hat{H}_{\rm i}(e^{i\Omega t} + e^{-i\Omega t})$ where $\hat{H}_{\rm i} = eEa_0(\hat{c}^\dagger + \hat{c})\hat{d}^\dagger\hat{d}/2$.

We will assume the electronic subsystem to always be in its equilibrium distribution at temperature T due to fast relaxation by processes not governed by Eq. (B.1). Hence, the density operator of the electronic subsystem takes the form

$$\hat{\rho}_{\rm el} = Z^{-1}\exp\left(-\sum_k \epsilon_k\hat{\psi}_k^\dagger\hat{\psi}_k/k_{\rm B}T\right) \tag{B.2}$$

with the partition function given by the trace over the electronic states

$$Z = {\rm Tr}_{\rm el}\left[\exp\left(-\sum_k \epsilon_k\hat{\psi}_k^\dagger\hat{\psi}_k/k_{\rm B}T\right)\right], \tag{B.3}$$

satisfying $\left[\hat{H}_0,\hat{\rho}_{\rm el}\right] = 0$. The density operator of the full system can then be separated into the form $\hat{\rho}(t) = \hat{\rho}_{\rm m}(t)\otimes\hat{\rho}_{\rm el}$, where $\hat{\rho}_{\rm m}(t)$ is the density operator of the mechanical subsystem.

We expand the mechanical density operator $\hat{\rho}_{\rm m}(t) = \sum_{n=-\infty}^{\infty}\hat{\rho}_n\exp(in\Omega t)$ where $\hat{\rho}_n = \sum_{k=0}^{\infty}\hat{\rho}_n^{(k)}$ and $\hat{\rho}_n^{(k)} \propto \varepsilon^{|n|+2k}$ with the small drive strength parameter $\varepsilon = eEa_0/(2\hbar\Omega) \ll 1$. This gives an infinite set of coupled equations, one

for each frequency $n\Omega$. To continue the analysis we choose to truncate the coupled dynamics at order ϵ^2, which results in the closed set of equations

$$0 = \left[\hat{H}_{\rm i},\hat{\rho}^{(0)}_{+1}\otimes\hat{\rho}_{\rm el}\right] + \left[\hat{H}_{\rm i},\hat{\rho}^{(0)}_{-1}\otimes\hat{\rho}_{\rm el}\right], \tag{B.4}$$

$$\mp\hbar\Omega\hat{\rho}^{(0)}_{\pm1}\otimes\hat{\rho}_{\rm el} = \left[\hat{H}_0,\hat{\rho}^{(0)}_{\pm1}\otimes\hat{\rho}_{\rm el}\right] + \left[\hat{H}_{\rm i},\hat{\rho}^{(0)}_{0}\otimes\hat{\rho}_{\rm el}\right], \tag{B.5}$$

where we have assumed the stationary term $\hat{\rho}^{(0)}_0$ and $\hat{\rho}^{(1)}_0$ to be diagonal in the $|n\rangle$ basis, due to dephasing processes not governed by (B.1).

Using the residue theorem we can express the operators

$$\hat{\rho}^{(0)}_{\pm1}\otimes\hat{\rho}_{\rm el} = -\frac{1}{2\pi i}\int {\rm d}\epsilon\ \hat{G}_+(\epsilon\mp\hbar\Omega)\left[\hat{H}_{\rm i},\hat{\rho}^{(0)}_0\otimes\hat{\rho}_{\rm el}\right]\hat{G}_-(\epsilon), \tag{B.6}$$

with

$$\hat{G}_\pm(\xi) = \frac{1}{\hat{H}_0-\xi\pm i\delta} \tag{B.7}$$

where $\delta\to0$ and $\hat{G}_+(\xi)$ $\left(\hat{G}_-(\xi)\right)$ has a pole in the upper (lower) complex plane and satisfies the identity

$$\delta(\hat{H}_0-\xi) = 2\pi i\left(\hat{G}_-(\xi)-\hat{G}_+(\xi)\right). \tag{B.8}$$

We substitute Eq. (B.6) into Eq. (B.4) in order to obtain a closed equation for the stationary density operator $\hat{\rho}^{(0)}_0\otimes\hat{\rho}_{\rm el}$. Eq. (B.4) contains eight terms, due to the two nested commutators. Two of these terms (one from each nested term) are

$$\begin{aligned}\chi = -\frac{1}{2\pi i}\int {\rm d}\epsilon\ \Big(&\hat{H}_{\rm i}\hat{G}_-(\epsilon+\hbar\Omega)\hat{H}_{\rm i}\hat{\rho}^{(0)}_0\otimes\hat{\rho}_{\rm el}\hat{G}_+(\epsilon)...\\ &+\hat{\rho}^{(0)}_0\otimes\hat{\rho}_{\rm el}\hat{G}_-(\epsilon-\hbar\Omega)\hat{H}_{\rm i}\hat{G}_+(\epsilon)\hat{H}_{\rm i}\Big).\end{aligned} \tag{B.9}$$

We shift the argument of the last term $\epsilon-\hbar\Omega\to\epsilon$. One of the $\hat{G}$-operators in each term can be substituted by a Dirac delta-function according to Eq. (B.8). This is because the integral along the real axis, with poles only in the upper or the lower complex plane, is zero. We then have

$$\begin{aligned}\chi = \int {\rm d}\epsilon\ \Big(&\hat{H}_{\rm i}\hat{G}_-(\epsilon+\hbar\Omega)\hat{H}_{\rm i}\hat{\rho}^{(0)}_0\otimes\hat{\rho}_{\rm el}\delta(\epsilon-\hat{H}_0)...\\ &-\hat{\rho}^{(0)}_0\otimes\hat{\rho}_{\rm el}\delta(\epsilon-\hat{H}_0)\hat{H}_{\rm i}\hat{G}_+(\epsilon+\hbar\Omega)\hat{H}_{\rm i}\Big).\end{aligned} \tag{B.10}$$

Since our next aim is to trace over the electronic states we may cycle $\hat{\rho}^{(0)}_0\otimes\hat{\rho}_{\rm el}$ and the delta functions. Combining the remaining $\hat{G}$-operators to delta functions and using the integral representation

$$\delta(\omega) = \frac{1}{2\pi}\int_{-\infty}^{\infty}{\rm d}t e^{-i\omega t} \tag{B.11}$$

brings us to the form

$$\chi = \frac{i}{\hbar}\int_{-\infty}^{\infty} \mathrm{d}t\; e^{it\Omega} e^{it\hat{H}_0/\hbar}\hat{H}_\mathrm{i} e^{-it\hat{H}_0/\hbar}\hat{H}_\mathrm{i}\hat{\rho}_0^{(0)}\otimes\hat{\rho}_\mathrm{el}. \tag{B.12}$$

Calculating the interaction picture of the first interaction Hamiltonian and substituting all operators give

$$\chi = \frac{(eEa_0)^2}{4\hbar}\int_{-\infty}^{\infty}\mathrm{d}t \sum_{k_1}\sum_{k_2}\sum_{k_3}\sum_{k_4}\; b_{k_1}b^*_{k_2}b_{k_3}b^*_{k_4}\times$$
$$e^{i\Omega t}\left(\hat{c}^\dagger e^{i\omega_\mathrm{m}t}+\hat{c}e^{-i\omega_\mathrm{m}t}\right)\left(\hat{c}^\dagger+\hat{c}\right)e^{i(\epsilon_1-\epsilon_2)t/\hbar}\hat{\psi}^\dagger_{k_1}\hat{\psi}_{k_2}\hat{\psi}^\dagger_{k_3}\hat{\psi}_{k_4}\hat{\rho}_0^{(0)}\otimes\hat{\rho}_\mathrm{el}, \tag{B.13}$$

where

$$b_\xi = \frac{\mathcal{T}}{\epsilon_\xi-\epsilon_0+i\hbar\Gamma}. \tag{B.14}$$

The trace over the electronic subsystem of χ can be calculated by using the commutation relations for the fermionic operators and successively moving one operator around one whole cycle. The result is

$$\mathrm{Tr}_\mathrm{el}\left[\hat{\psi}^\dagger_{k_1}\hat{\psi}_{k_2}\hat{\psi}^\dagger_{k_3}\hat{\psi}_{k_4}\hat{\rho}_\mathrm{el}\right] = \delta_{k_1,k_2}\delta_{k_3,k_4}f_{k_1}f_{k_2}+\delta_{k_1,k_4}\delta_{k_2,k_3}f_{k_1}\Big(1-f_{k_3}\Big), \tag{B.15}$$

where f is the Fermi-Dirac distribution function. Two of the sums in Eq. (B.13) take out the Kronecker deltas in Eq. (B.15) and the integral over t gives a delta function for energy conservation. The contribution from the other six terms in Eq. (B.4) can be calculated in an analogous manner. The rate equation for the diagonal elements of the stationary mechanical density operator then becomes

$$\Gamma^-\left(\hat{c}\hat{\rho}_\mathrm{st}\hat{c}^\dagger-\hat{c}^\dagger\hat{c}\hat{\rho}_\mathrm{st}\right)+\Gamma^+\left(\hat{c}^\dagger\hat{\rho}_\mathrm{st}\hat{c}-\hat{c}\hat{c}^\dagger\hat{\rho}_\mathrm{st}\right)=0 \tag{B.16}$$

with $\Gamma^\pm = \Gamma^{\pm\omega_\mathrm{m}}_{+\Omega}+\Gamma^{\pm\omega_\mathrm{m}}_{-\Omega}$ and

$$\Gamma^{\pm\omega_\mathrm{m}}_{\pm\Omega} = \frac{(eEa_0)^2}{2\pi\hbar^2\Gamma}\int \mathrm{d}\epsilon_1\mathrm{d}\epsilon_2 f(\epsilon_1)\Big(1-f(\epsilon_2)\Big)\frac{(\hbar\Gamma)^3\delta(\epsilon_2-\epsilon_1\pm\hbar\Omega\pm\hbar\omega_\mathrm{m})}{\left|\epsilon_1-\epsilon_0+i\hbar\Gamma\right|^2\left|\epsilon_2-\epsilon_0+i\hbar\Gamma\right|^2}. \tag{B.17}$$

By comparing this with the linear Lindblad superoperator in Eq. (A.2), it is evident that they have the same structure under the diagonal condition of $\hat{\rho}$. We add the dissipative superoperator terms to Eq. (B.16), at zero temperature for simplicity. By projecting Eq. (B.16) on the diagonal state $\langle n|...|n\rangle$ we get the rate equation

$$\begin{aligned}&\gamma_\mathrm{NL}(n+1)(n+2)P_{n+2}+(\Gamma^-+\gamma_\mathrm{L})(n+1)P_{n+1}+\Gamma^+nP_{n-1}\\&\quad-\left(\gamma_\mathrm{NL}n(n-1)+(\Gamma^-+\gamma_\mathrm{L})n+\Gamma^+(n+1)\right)P_n=0\end{aligned} \tag{B.18}$$

for the stationary occupation probabilities $P_n=\langle n|\hat{\rho}_0^{(0)}|n\rangle$.

Appendix C

Average Number of Quanta

The aim of this appendix is to derive an expression for the stationary average number of vibrational quanta $\mathcal{N}$ governed by the rate equation derived in Appendix B,

$$\begin{aligned}\gamma_{\mathrm{NL}}(n+1)(n+2)P_{n+2} + (\Gamma^- + \gamma_{\mathrm{L}})(n+1)P_{n+1} + \Gamma^+ n P_{n-1} \\ - \left(\gamma_{\mathrm{NL}} n(n-1) + (\Gamma^- + \gamma_{\mathrm{L}})n + \Gamma^+(n+1)\right) P_n = 0. \end{aligned} \tag{C.1}$$

To do this, let us introduce $\mathcal{P}(z) = \sum_{n=0}^{\infty} z^n P_n$, where z is a complex number inside the unit circle. The probabilities P_n have to sum up to 1, which gives $\mathcal{P}(1) = 1$ and $\mathcal{P}(-1)$ has to be absolute convergent. The trick is to multiply Eq. (C.1) by z^n and sum over $\sum_{n=0}^{\infty}$. The first term in Eq. (C.1) can then be manipulated as

$$\begin{aligned}\sum_{n=0}^{\infty} z^n (n+1)(n+2)P_{n+2} = \frac{\partial^2}{\partial z^2} \sum_{n=0}^{\infty} z^{n+2} P_{n+2} = \\ = \frac{\partial^2}{\partial z^2}(\mathcal{P}(z) - P_0 - zP_1) = \frac{\partial^2}{\partial z^2}\mathcal{P}(z). \end{aligned} \tag{C.2}$$

Similarly, the third term in Eq. (C.1) can be manipulated by using $P_{-1} = 0$, there is no probability to occupy *negative* numbers of vibrational quanta,

$$\begin{aligned}\sum_{n=0}^{\infty} z^n n P_{n-1} = \sum_{m=0}^{\infty} z^{m+1}(m+1)P_m = z\frac{\partial}{\partial z}\sum_{m=0}^{\infty} z^{m+1} P_m = \\ = z\frac{\partial}{\partial z}\Big(z\mathcal{P}(z)\Big) = z\left(1 + z\frac{\partial}{\partial z}\right)\mathcal{P}(z). \end{aligned} \tag{C.3}$$

The other terms can be manipulated in an analogous manner. Summing all terms in Eq. (C.1) and excluding the common factor of $1 - z$ result in the

homogeneous second order differential equation

$$(1+z)\frac{\partial^2}{\partial z^2}\mathcal{P}(z)+\frac{\Gamma^-+\gamma_{\rm L}}{\gamma_{\rm NL}}\frac{\partial}{\partial z}\mathcal{P}(z)-\frac{\Gamma^+}{\gamma_{\rm NL}}\left(1+z\frac{\partial}{\partial z}\right)\mathcal{P}(z)=0. \tag{C.4}$$

We can rewrite it as

$$\frac{\partial}{\partial z}\left((1+z)\frac{\partial}{\partial z}\mathcal{P}(z)\right)-\frac{\partial}{\partial z}\mathcal{P}(z)+\frac{\Gamma^-+\gamma_{\rm L}}{\gamma_{\rm NL}}\frac{\partial}{\partial z}\mathcal{P}(z)-\frac{\Gamma^+}{\gamma_{\rm NL}}\frac{\partial}{\partial z}\Big(z\mathcal{P}(z)\Big)=0. \tag{C.5}$$

This equation can be integrated trivially one time in z, yielding a non-homogeneous first order differential equation

$$\frac{\partial}{\partial z}\mathcal{P}(z)-h(z)\mathcal{P}(z)=g(z),\quad h(z)=\frac{\left(1-\frac{\Gamma^-+\gamma_{\rm L}}{\gamma_{\rm NL}}+\frac{\Gamma^+}{\gamma_{\rm NL}}z\right)}{1+z},\quad g(z)=\frac{C_1}{1+z} \tag{C.6}$$

where C_i, $i=1,2...$ are constants of integration. The homogeneous solution is $\mathcal{P}_{\rm h}(z)=\exp(f(z))$ where $f'(z)=h(z)$. The particular solution can be written as $\mathcal{P}_{\rm p}(z)=\int_{-1}^{z}{\rm d}z'\exp(f(z)-f(z'))g(z')$. If we write

$$f(z)=(1-(\Gamma^++\Gamma^-+\gamma_{\rm L})/\gamma_{\rm NL})\ln(1+z)+(1+z)\Gamma^+/\gamma_{\rm NL}+C_2, \tag{C.7}$$

the full solution (with new constants C_3 and C_4) takes the form

$$\begin{aligned}\mathcal{P}(z)=&C_3(1+z)^{\left(1-\frac{\Gamma^++\Gamma^-+\gamma_{\rm L}}{\gamma_{\rm NL}}\right)}...\\&+C_4\int_{-1}^{z}{\rm d}z'\ \left(\frac{1+z'}{1+z}\right)^{\left(\frac{\Gamma^++\Gamma^-+\gamma_{\rm L}}{\gamma_{\rm NL}}-1\right)}\frac{e^{\frac{\Gamma^+}{\gamma_{\rm NL}}(z-z')}}{1+z'}.\end{aligned} \tag{C.8}$$

To satisfy the absolute convergence criteria at $z=-1$ of $\mathcal{P}(z)$ the constant C_3 has to be zero. Finally, we integrate by parts to obtain the solution

$$\mathcal{P}(z)=C_5\left(1+\frac{\Gamma^+}{\gamma_{\rm NL}}\int_{-1}^{z}{\rm d}z'\ \left(\frac{1+z'}{1+z}\right)^{\left(\frac{\Gamma^++\Gamma^-+\gamma_{\rm L}}{\gamma_{\rm NL}}-1\right)}e^{\frac{\Gamma^+}{\gamma_{\rm NL}}(z-z')}\right) \tag{C.9}$$

where the constant C_5 is given by the condition $\mathcal{P}(1)=1$,

$$C_5=\left(1+\frac{\Gamma^+}{\gamma_{\rm NL}}\int_{-1}^{1}{\rm d}z'\ \left(\frac{1+z'}{2}\right)^{\left(\frac{\Gamma^++\Gamma^-+\gamma_{\rm L}}{\gamma_{\rm NL}}-1\right)}e^{\frac{\Gamma^+}{\gamma_{\rm NL}}(1-z')}\right)^{-1}. \tag{C.10}$$

The stationary average number of vibrational quanta $\mathcal{N}$ is then given by the relation $\mathcal{N}=\partial_z\mathcal{P}(z)$.

Bibliography

[1] M. D. LaHaye, O. Buu, B. Camarota, and K. C. Schwab, *Approaching the quantum limit of a nanomechanical resonator*, Science **304** (2004), no. 5667, 74–77.

[2] A. D. O'Connell, M. Hofheinz, M. Ansmann, R. C. Bialczak, M. Lenander, E. Lucero, M. Neeley, D. Sank, H. Wang, M. Weides, J. Wenner, J. M. Martinis, and A. N. Cleland, *Quantum ground state and single-phonon control of a mechanical resonator*, Nature **464** (2010), no. 7289, 697 – 703.

[3] H. Grabert and M. H. Devoret, *Single charge tunneling: Coulomb blockade phenomena in nanostructures*, Springer, London, 1992.

[4] K. Jensen, J. Weldon, H. Garcia, and A. Zettl, *Nanotube radio*, Nano Letters **7** (2007), no. 11, 3508–3511.

[5] C. Chen, S. Lee, V. V. Deshpande, G.-H. Lee, M. Lekas, K. Shepard, and J. Hone, *Graphene mechanical oscillators with tunable frequency*, Nat. Nano. **8** (2013), no. 12, 923–927.

[6] S. T. Bartsch, A. Rusu, and A. M. Ionescu, *A single active nanoelectromechanical tuning fork front-end radio-frequency receiver*, Nanotechnology **23** (2012), no. 22, 225501.

[7] E. Pop, *Energy dissipation and transport in nanoscale devices*, Nano Research **3** (2010), no. 3, 147–169.

[8] H. B. Meerwaldt, G. Labadze, B. H. Schneider, A. Taspinar, Ya. M. Blanter, H. S. J. van der Zant, and G. A. Steele, *Probing the charge of a quantum dot with a nanomechanical resonator*, Phys. Rev. B **86** (2012), 115454.

[9] J. Moser, J. Guttinger, A. Eichler, M. J. Esplandiu, D. E. Liu, M. I. Dykman, and A. Bachtold, *Ultrasensitive force detection with a nanotube mechanical resonator*, Nat. Nano. **8** (2013), no. 7, 493–496.

[10] J. Chaste, A. Eichler, J. Moser, G. Ceballos, R. Rurali, and A. Bachtold, *A nanomechanical mass sensor with yoctogram resolution*, Nat. Nano. **7** (2012), no. 5, 301–304.

[11] V. Sazonova, Y. Yaish, H. Ustunel, D. Roundy, T. A. Arias, and P. L. McEuen, *A tunable carbon nanotube electromechanical oscillator*, Nature **431** (2004), no. 7006, 284 – 287.

[12] A. K. Geim and I. V. Grigorieva, *Van der waals heterostructures*, Nature **499** (2013), no. 7459, 419 – 425.

[13] G. D. Cole, S. Gröblacher, K. Gugler, S. Gigan, and M. Aspelmeyer, *Monocrystalline $Al_xGa_{1-x}As$ heterostructures for high-reflectivity high-Q micromechanical resonators in the megahertz regime*, Applied Physics Letters **92** (2008), no. 26, 261108.

[14] B. Lassagne, Y. Tarakanov, J. Kinaret, D. Garcia-Sanchez, and A. Bachtold, *Coupling mechanics to charge transport in carbon nanotube mechanical resonators*, Science **325** (2009), no. 5944, 1107–1110.

[15] G. A. Steele, A. K. Hüttel, B. Witkamp, M. Poot, H. B. Meerwaldt, L. P. Kouwenhoven, and H. S. J. van der Zant, *Strong coupling between single-electron tunneling and nanomechanical motion*, Science **325** (2009), no. 5944, 1103–1107.

[16] L. L. Li, P. M. Polunin, S. Dou, O. Shoshani, B. S. Strachan, J. S. Jensen, S. W. Shaw, and K. L. Turner, *Tailoring the nonlinear response of mems resonators using shape optimization*, Applied Physics Letters **110** (2017), no. 8, 081902.

[17] D. Antonio, D. H. Zanette, and D. López, *Frequency stabilization in nonlinear micromechanical oscillators*, Nat. Comm. **3** (2012), 806.

[18] A. M. Eriksson, *Nonresonant high-frequency actuation of carbon based nanoelectromechanical oscillators*, Institutionen för teknisk fysik, Chalmers tekniska högskola, Göteborg, 2015.

[19] K. L. Ekinci and M. L. Roukes, *Nanoelectromechanical systems*, Review of Scientific Instruments **76** (2005), no. 6, 061101.

[20] G. S. Paraoanu and A. M. Halvari, *Suspended single-electron transistors: Fabrication and measurement*, Applied Physics Letters **86** (2005), no. 9, 093101.

[21] D. Hatanaka, I. Mahboob, H. Okamoto, K. Onomitsu, and H. Yamaguchi, *An electromechanical membrane resonator*, Applied Physics Letters **101** (2012), no. 6, 063102.

[22] Z. Wang, H. Jia, X.-Q. Zheng, R. Yang, G. J. Ye, X. H. Chen, and P. X.-L. Feng, *Resolving and tuning mechanical anisotropy in black phosphorus via nanomechanical multimode resonance spectromicroscopy*, Nano Letters **16** (2016), no. 9, 5394–5400.

[23] H. Kim, D. H. Shin, K. McAllister, M. Seo, S. Lee, I.-S. Kang, B. H. Park, E. E. B. Campbell, and S. W. Lee, *Accurate and precise determination of mechanical properties of silicon nitride beam nanoelectromechanical devices*, ACS Applied Materials & Interfaces **9** (2017), no. 8, 7282–7287.

[24] P. Weber, J. Güttinger, A. Noury, J. Vergara-Cruz, and A. Bachtold, *Force sensitivity of multilayer graphene optomechanical devices*, Nat. Comm. **7** (2016), 12496.

[25] M. Terrones, A. R. Botello-Méndez, J. Campos-Delgado, F. López-Urías, Y. I. Vega-Cantú, F. J. Rodríguez-Macías, A. L. Elías, E. Muñoz-Sandoval, A. G. Cano-Márquez, J.-C. Charlier, and H. Terrones, *Graphene and graphite nanoribbons: Morphology, properties, synthesis, defects and applications*, Nano Today **5** (2010), no. 4, 351 – 372.

[26] K. S. Novoselov, V. I. Fal'ko, L. Colombo, P. R. Gellert, M. G. Schwab, and K. Kim, *A roadmap for graphene*, Nature **490** (2012), no. 7419, 192 – 200.

[27] L. Banszerus, M. Schmitz, S. Engels, M. Goldsche, K. Watanabe, T. Taniguchi, B. Beschoten, and C. Stampfer, *Ballistic transport exceeding 28 μm in cvd grown graphene*, Nano Letters **16** (2016), no. 2, 1387–1391.

[28] F. Schwierz, *Graphene transistors*, Nat Nano **5** (2010), no. 7, 487 – 496.

[29] R. R. Nair, P. Blake, A. N. Grigorenko, K. S.Novoselov, T. J. Booth, T. Stauber, N. M. R. Peres, and A. K. Geim, *Fine structure constant defines visual transparency of graphene*, Science **320** (2008), no. 5881, 1308–1308.

[30] R. Saito, G. Dresselhaus, and M. S. Dresselhaus, *Physical properties of carbon nanotubes*, Edition 2, Imperial College Press, London, 1998.

[31] T. W. Odom, J. Huang, P. Kim, and C. M. Lieber, *Atomic structure and electronic properties of single-walled carbon nanotubes*, Nature **391** (1998), no. 6662, 62 – 64.

[32] L. D. Landau, E. M. Lifshitz, and L. P. Pitaevskii, *Electrodynamics of continuous media vol. 8 of course of theoretical physics*, Butterworth-Heinemann, Oxford, 1984, pp. 29-30.

[33] P. Horowitz and W. Hill, *The art of electronics*, Third Edition, Cambridge University Press, Cambridge, 2015.

[34] M. Jablan, M. Soljačić, and H. Buljan, *Plasmons in graphene: Fundamental properties and potential applications*, Proceedings of the IEEE **101** (2013), no. 7, 1689–1704.

[35] D. Svintsov, V. Vyurkov, S. Yurchenko, T. Otsuji, and V. Ryzhii, *Hydrodynamic model for electron-hole plasma in graphene*, Journal of Applied Physics **111** (2012), no. 8, 083715.

[36] L. D. Landau and E. M. Lifshitz, *Quantum mechanics non-relativistic theory*, Course of theoretical physics, Volume 3 Third Edition, Butterworth-Heinemann, Oxford, 1977.

[37] R. Wiesendanger, *Scanning probe microscopy and spectroscopy: methods and applications*, Chap. 1, Cambridge University Press, Cambridge, 1994.

[38] A. V. Parafilo, I. V. Krive, R. I. Shekhter, and M. Jonson, *Nanoelectromechanics of superconducting weak links (review article)*, Low Temperature Physics **38** (2012), no. 4, 273–282.

[39] V. Bouchiat, D. Vion, P. Joyez, D. Esteve, and M. H. Devoret, *Quantum coherence with a single cooper pair*, Physica Scripta **1998** (1998), no. T76, 165.

[40] Y. Nakamura, Yu. A. Pashkin, and J. S. Tsai, *Coherent control of macroscopic quantum states in a single-cooper-pair box*, Nature **398** (1999), no. 6730, 786 – 788.

[41] P. Poncharal, Z. L. Wang, D. Ugarte, and W. A. de Heer, *Electrostatic deflections and electromechanical resonances of carbon nanotubes*, Science **283** (1999), no. 5407, 1513–1516.

[42] K. N. Kudin, G. E. Scuseria, and B. I. Yakobson, *C_2F, BN, and C nanoshell elasticity from ab initio computations*, Phys. Rev. B **64** (2001), 235406.

[43] D. Garcia-Sanchez, A. M. van der Zande, A. San Paulo, B. Lassagne, P. L. McEuen, and A. Bachtold, *Imaging mechanical vibrations in suspended graphene sheets*, Nano Letters **8** (2008), no. 5, 1399–1403.

[44] S. Y. Kim and H. S. Park, *The importance of edge effects on the intrinsic loss mechanisms of graphene nanoresonators*, Nano Letters **9** (2009), no. 3, 969–974.

[45] C. Lee, X. Wei, J. W. Kysar, and J. Hone, *Measurement of the elastic properties and intrinsic strength of monolayer graphene*, Science **321** (2008), no. 5887, 385–388.

[46] A.N. Cleland, *Foundations of nanomechanics: From solid-state theory to device applications*, Advanced Texts in Physics, Springer Berlin Heidelberg, 2002.

[47] D. Davidovikj, J. J. Slim, S. J. Cartamil-Bueno, Herre S. J. van der Zant, P. G. Steeneken, and W. J. Venstra, *Visualizing the motion of graphene nanodrums*, Nano Letters **16** (2016), no. 4, 2768–2773.

[48] Z. Wang and P. X.-L. Feng, *Design of black phosphorus 2d nanomechanical resonators by exploiting the intrinsic mechanical anisotropy*, 2D Materials **2** (2015), no. 2, 021001.

[49] J. Atalaya, A. Isacsson, and J. M. Kinaret, *Continuum elastic modeling of graphene resonators*, Nano Letters **8** (2008), no. 12, 4196–4200.

[50] L. D. Landau, E. M. Lifshitz, A. M. Kosevich, and L.P. Pitaevskiĭ, *Theory of elasticity*, Course of theoretical physics, Third Edition, Pergamon Press, Oxford, 1986.

[51] J. S. Bunch, S. S. Verbridge, J. S. Alden, A. M. van der Zande, J. M. Parpia, H. G. Craighead, and P. L. McEuen, *Impermeable atomic membranes from graphene sheets*, Nano Letters **8** (2008), no. 8, 2458–2462.

[52] M. Dequesnes, S. V. Rotkin, and N. R. Aluru, *Calculation of pull-in voltages for carbon-nanotube-based nanoelectromechanical switches*, Nanotechnology **13** (2002), no. 1, 120.

[53] J. Moser, A. Eichler, J. Güttinger, M. I. Dykman, and A. Bachtold, *Nanotube mechanical resonators with quality factors of up to 5 million*, Nat Nano **9** (2014), no. 12, 1007 – 1011.

[54] R. Lifshitz and M. L. Roukes, *Thermoelastic damping in micro- and nanomechanical systems*, Phys. Rev. B **61** (2000), 5600–5609.

[55] I. Wilson-Rae, *Intrinsic dissipation in nanomechanical resonators due to phonon tunneling*, Phys. Rev. B **77** (2008), 245418.

[56] J. Rieger, A. Isacsson, M. J. Seitner, J. P. Kotthaus, and E. M. Weig, *Energy losses of nanomechanical resonators induced by atomic force microscopy-controlled mechanical impedance mismatching*, Nat. Comm. **5** (2014), 3345.

[57] E. Malic, T. Winzer, E. Bobkin, and A. Knorr, *Microscopic theory of absorption and ultrafast many-particle kinetics in graphene*, Phys. Rev. B **84** (2011), 205406.

[58] A. Croy, D. Midtvedt, A. Isacsson, and J. M. Kinaret, *Nonlinear damping in graphene resonators*, Phys. Rev. B **86** (2012), 235435.

[59] Eichler A., Moser J., Chaste J., Zdrojek M., Wilson-Rae I., and Bachtold A., *Nonlinear damping in mechanical resonators made from carbon nanotubes and graphene*, Nat Nano **6** (2011), no. 6, 339 – 342.

[60] A. H. Nayfeh and D. T. Mook, *Nonlinear oscillations*, Physics textbook, Wiley-VCH,Weinheim, 2004.

[61] R. De Alba, F. Massel, I. R. Storch, T. S. Abhilash, A. Hui, P. L. McEuen, H. G. Craighead, and J. M. Parpia, *Tunable phonon-cavity coupling in graphene membranes*, Nat. Nano. **11** (2016), no. 9, 741–746.

[62] L. D. Landau and E. M. Lifshitz, *Mechanics*, Pergamon Press, Oxford, 1976.

[63] Q. P. Unterreithmeier, E. M. Weig, and J. P. Kotthaus, *Universal transduction scheme for nanomechanical systems based on dielectric forces*, Nature **458** (2009), no. 7241, 1001–1004.

[64] M. Poot, S. Etaki, I. Mahboob, K. Onomitsu, H. Yamaguchi, Y. M. Blanter, and H. S. J. van der Zant, *Tunable backaction of a dc squid on an integrated micromechanical resonator*, Phys. Rev. Lett. **105** (2010), 207203.

[65] L. Y. Gorelik, A. Isacsson, M. V. Voinova, B. Kasemo, R. I. Shekhter, and M. Jonson, *Shuttle mechanism for charge transfer in coulomb blockade nanostructures*, Phys. Rev. Lett. **80** (1998), no. cond-mat/9711196. APR-97-75. 20, 4526–4529.

[66] A. Isacsson, L. Y. Gorelik, M. V. Voinova, B. Kasemo, R. I. Shekhter, and M. Jonson, *Shuttle instability in self-assembled coulomb blockade nanostructures*, Physica B: Condensed Matter **255** (1998), no. 1-4, 150–163.

[67] M. T. Tuominen, R. V. Krotkov, and M. L. Breuer, *Stepwise and hysteretic transport behavior of an electromechanical charge shuttle*, Phys. Rev. Lett. **83** (1999), 3025–3028.

[68] P. Benjamin, *The intellectual rise in electricity*, vol. p. 507, Appleton, New York, 1895.

[69] C. H. Metzger and K. Karrai, *Cavity cooling of a microlever*, Nature **432** (2004), 1002–1005.

[70] T. J. Kippenberg and K. J. Vahala, *Cavity optomechanics: Back-action at the mesoscale*, Science **321** (2008), no. 5893, 1172–1176.

[71] R. A. Barton, I. R. Storch, V. P. Adiga, R. Sakakibara, B. R. Cipriany, B. Ilic, S. P. Wang, P. Ong, P. L. McEuen, J. M. Parpia, and H. G. Craighead, *Photothermal self-oscillation and laser cooling of graphene optomechanical systems*, Nano Letters **12** (2012), no. 9, 4681–4686.

[72] T. T. Heikkilä, *Physics of nanoelectronics: Transport and fluctuation phenomena at low temperatures*, OUP Oxford Master Series in Physics, Oxford, 2014, pp. 218-219.

[73] K. Brown, J. Britton, R. Epstein, J. Chiaverini, D. Leibfried, and D. Wineland, *Passive cooling of a micromechanical oscillator with a resonant electric circuit*, Phys. Rev. Lett. **99** (2007), 137205.

[74] J. A. Sanders, F. Verhulst, and J. Murdock, *Averaging methods in nonlinear dynamical systems*, Second Edition, Springer, New York, 2007.

[75] T. Barois, S. Perisanu, P. Poncharal, P. Vincent, S. T. Purcell, and A. Ayari, *Quality-factor enhancement of nanoelectromechanical systems by capacitive driving beyond resonance*, Phys. Rev. Applied **6** (2016), 014012.

[76] L. Fritz, J. Schmalian, M. Müller, and S. Sachdev, *Quantum critical transport in clean graphene*, Phys. Rev. B **78** (2008), 085416.

[77] A. B. Kashuba, *Conductivity of defectless graphene*, Phys. Rev. B **78** (2008), 085415.

[78] T. Novotný, A. Donarini, and A.-P. Jauho, *Quantum shuttle in phase space*, Phys. Rev. Lett. **90** (2003), 256801.

[79] P. Stadler, W. Belzig, and G. Rastelli, *Ground-state cooling of a carbon nanomechanical resonator by spin-polarized current*, Phys. Rev. Lett. **113** (2014), 047201.

[80] P. Stadler, W. Belzig, and G. Rastelli, *Ground-state cooling of a mechanical oscillator by interference in andreev reflection*, Phys. Rev. Lett. **117** (2016), 197202.

[81] J. Atalaya and L. Y. Gorelik, *Spintronics-based mesoscopic heat engine*, Phys. Rev. B **85** (2012), 245309.

[82] M. Ziese, *Extrinsic magnetotransport phenomena in ferromagnetic oxides*, Reports on Progress in Physics **65** (2002), no. 2, 143.

[83] H. P. Breuer and F. Petruccione, *The theory of open quantum systems*, Oxford University Press, Oxford, 2002.

[84] G. Schaller, *Open quantum systems far from equilibrium*, Lecture Notes in Physics, Springer International Publishing, Heidelberg, 2014.

[85] A. Vikström, *Nanomechanical phenomena in low-dimensional structures*, Doktorsavhandlingar vid Chalmers tekniska högskola. Ny serie, no: 4262, Institutionen för fysik, Kondenserade materiens teori (Chalmers), Chalmers tekniska högskola, 2017.

[86] S. Etaki, M. Poot, I. Mahboob, K. Onomitsu, H. Yamaguchi, and H. S. J. van der Zant, *Motion detection of a micromechanical resonator embedded in a d.c. SQUID*, Nature Physics **4** (2008), no. 10, 785 – 788.

[87] M. D. LaHaye, J. Suh, P. M. Echternach, K. C. Schwab, and M. L. Roukes, *Nanomechanical measurements of a superconducting qubit*, Nature **459** (2009), no. 7249, 960 – 964.

[88] J.-M. Pirkkalainen, S. U. Cho, J. Li, G. S. Paraoanu, P. J. Hakonen, and M. A. Sillanpaa, *Hybrid circuit cavity quantum electrodynamics with a micromechanical resonator*, Nature **494** (2013), no. 7436, 211 – 215.

[89] A. P. Reed, K. H. Mayer, J. D. Teufel, L. D. Burkhart, W. Pfaff, M. Reagor, L. Sletten, X. Ma, R. J. Schoelkopf, E. Knill, and K. W. Lehnert, *Faithful conversion of propagating quantum information to mechanical motion*, (2017), arXiv:1703.02548, quant-ph.

[90] A. Buzdin, *Direct coupling between magnetism and superconducting current in the josephson φ_0 junction*, Phys. Rev. Lett. **101** (2008), 107005.

[91] J.-F. Liu and K. S. Chan, *Anomalous josephson current through a ferromagnetic trilayer junction*, Phys. Rev. B **82** (2010), 184533.

[92] H. Zhang, J. Wang, and J.-F. Liu, *Anomalous josephson effect in noncentrosymmetric superconductors*, Applied Physics Letters **108** (2016), no. 10, 102601.

[93] F. Dolcini, M. Houzet, and J. S. Meyer, *Topological josephson ϕ_0 junctions*, Phys. Rev. B **92** (2015), 035428.

[94] Y. Tanaka, T. Yokoyama, and N. Nagaosa, *Manipulation of the majorana fermion, andreev reflection, and josephson current on topological insulators*, Phys. Rev. Lett. **103** (2009), 107002.

[95] A. Zazunov, R. Egger, T. Jonckheere, and T. Martin, *Anomalous josephson current through a spin-orbit coupled quantum dot*, Phys. Rev. Lett. **103** (2009), 147004.

[96] L. Dell'Anna, A. Zazunov, R. Egger, and T. Martin, *Josephson current through a quantum dot with spin-orbit coupling*, Phys. Rev. B **75** (2007), 085305.

[97] Constantin Schrade, Silas Hoffman, and Daniel Loss, *Detecting topological superconductivity with φ_0 josephson junctions*, Phys. Rev. B **95** (2017), 195421.

[98] F. Dolcini and F. Giazotto, *Switching the sign of josephson current through aharonov-bohm interferometry*, Phys. Rev. B **75** (2007), 140511.

[99] T. Yokoyama, M. Eto, and Y. V. Nazarov, *Anomalous josephson effect induced by spin-orbit interaction and zeeman effect in semiconductor nanowires*, Phys. Rev. B **89** (2014), 195407.

[100] G. Campagnano, P. Lucignano, D. Giuliano, and A. Tagliacozzo, *Spin–orbit coupling and anomalous josephson effect in nanowires*, Journal of Physics: Condensed Matter **27** (2015), no. 20, 205301.

[101] D. B. Szombati, S. Nadj-Perge, D. Car, S. R. Plissard, E. P. A. M. Bakkers, and L. P. Kouwenhoven, *Josephson ϕ_0-junction in nanowire quantum dots*, Nat. Phys. **12** (2016), no. 6, 568 – 572.

[102] L. Y. Gorelik, A. Isacsson, Y. M. Galperin, R. I. Shekhter, and M. Jonson, *Coherent transfer of cooper pairs by a movable grain*, Nature **411** (2001), no. 6836, 454 – 457.

[103] A. Isacsson, L. Y. Gorelik, R. I. Shekhter, Y. M. Galperin, and M. Jonson, *Mechanical cooper pair transportation as a source of long-distance superconducting phase coherence*, Phys. Rev. Lett. **89** (2002), 277002.

[104] M. E. Pe na-Aza, A. Scorrano, and L. Y. Gorelik, *Parametric excitation of dc current in a single-dot shuttle system via spontaneous symmetry breaking*, Phys. Rev. B **88** (2013), 035412.

[105] J. Bylander, T. Duty, and P. Delsing, *Current measurement by real-time counting of single electrons*, Nature **434** (2005), no. 7031, 361 – 364.

[106] M. I. Dykman, C. M. Maloney, V. N. Smelyanskiy, and M. Silverstein, *Fluctuational phase-flip transitions in parametrically driven oscillators*, Phys. Rev. E **57** (1998), 5202–5212.

[107] J. P. Mathew, R. N. Patel, A. Borah, R. Vijay, and M. M. Deshmukh, *Dynamical strong coupling and parametric amplification of mechanical modes of graphene drums*, Nat. Nano. **11** (2016), no. 9, 747–751.

[108] H. Okamoto, A. Gourgout, C.-Y. Chang, K. Onomitsu, I. Mahboob, E. Y. Chang, and H. Y., *Coherent phonon manipulation in coupled mechanical resonators*, Nat. Phys. **9** (2013), no. 8, 480–484.

[109] T. Faust, J. Rieger, M. J. Seitner, J. P. Kotthaus, and E. M. Weig, *Coherent control of a classical nanomechanical two-level system*, Nat. Phys. **9** (2013), no. 8, 485–488.

[110] A. Leuch, L. Papariello, O. Zilberberg, C. L. Degen, R. Chitra, and A. Eichler, *Parametric symmetry breaking in a nonlinear resonator*, Phys. Rev. Lett. **117** (2016), 214101.

[111] M. J. Seitner, M. Abdi, A. Ridolfo, M. J. Hartmann, and E. M. Weig, *Parametric oscillation, frequency mixing, and injection locking of strongly coupled nanomechanical resonator modes*, Phys. Rev. Lett. **118** (2017), 254301.

[112] C. Chen, D. H. Zanette, D. A. Czaplewski, S. Shaw, and D. López, *Direct observation of coherent energy transfer in nonlinear micromechanical oscillators*, Nat. Comm. **8** (2017), 15523.

[113] D. Antonio, D. H. Zanette, and D. López, *Frequency stabilization in nonlinear micromechanical oscillators*, Nat. Comm. **3** (2012), 806.

[114] S. P. Timoshenko and S. Woinowsky-Krieger, *Theory of plates and shells*, Second Edition, Engineering societies monographs, McGraw-Hill, Singapore, 1959.

[115] S. P. Timoshenko and J. N. Goodier, *Theory of elasticity*, Third Edition, McGraw-Hill, Singapore, 1970.

[116] J. Mathews and R. L. Walker, *Mathematical methods of physics*, Second Edition, Addison-Wesley World Student Series, Addison-Wesley Publishing Company, inc., New York, 1970.

[117] R. Lifshitz and M. C. Cross, *Nonlinear dynamics of nanomechanical and micromechanical resonators, in Reviews of nonlinear dynamics and complexity (ed. H. G. Schuster)*, Wiley-VCH Verlag GmbH & Co. KGaA, Weinheim, 2008.

[118] CL MATCONT MATCONT and CL MATCONT for MAPS, *Version matcont6p2 , http://www.matcont.ugent.be/*, (2015-05-21).

[119] C. van der Avoort, R. van der Hout, J. J. M. Bontemps, P. G. Steeneken, K. Le Phan, R. H. B. Fey, J. Hulshof, and J. T. M. van Beek, *Amplitude saturation of mems resonators explained by autoparametric resonance*, Journal of Micromechanics and Microengineering **20** (2010), no. 10, 105012.

[120] R. B. Karabalin, M. C. Cross, and M. L. Roukes, *Nonlinear dynamics and chaos in two coupled nanomechanical resonators*, Phys. Rev. B **79** (2009), 165309.

[121] O. Shoshani, S. W. Shaw, and M. I. Dykman, *Anomalous dissipation of nanomechanical modes going through nonlinear resonance*, (2016), arXiv:1702.00769, cond-mat.mes-hall.

[122] H. Carmichael, *An open systems approach to quantum optics*, Springer Verlag, Berlin, 1991, pp. 6-9.

[123] A. Voje, A. Croy, and A. Isacsson, *Multi-phonon relaxation and generation of quantum states in a nonlinear mechanical oscillator*, New Journal of Physics **15** (2013), no. 5, 053041.